A Measurement of the Exclusive Branching Fraction for $B \to \pi K$ at BaBar

Marie Louise Aspinwall

Imperial College

A thesis submitted for the degree of Doctor of Philosophy
at the University of London
February 2002

ABSTRACT

This thesis presents an exclusive measurement of the branching fraction $\mathcal{B}$ for the rare charmless hadronic B decays to πK final states. A sample of 22.57 ± 0.36 million $B\overline{B}$ pairs was collected with the BaBar detector at the Stanford Linear Accelerator Center's PEP-II B Factory, during the Run 1 data taking period (1999-2000). The following branching fractions have been measured:

$$\mathcal{B}(B^0 \to \pi^\pm K^\mp) = (26.6 \pm 3.4(\mathrm{stat}) \pm 3.3(\mathrm{syst})) \times 10^{-6}$$

$$\mathcal{B}(B^\pm \to \pi^0 K^\pm) = (18.9 \pm 4.0(\mathrm{stat}) \pm 3.6(\mathrm{syst})) \times 10^{-6}$$

$$\mathcal{B}(B^\pm \to \pi^\pm K^0_S) = (17.8 \pm 4.0(\mathrm{stat}) \pm 5.3(\mathrm{syst})) \times 10^{-6}$$

$$\mathcal{B}(B^0 \to \pi^0 K^0_S) = (4.1 \pm 4.2(\mathrm{stat}) \pm 2.5(\mathrm{syst})) \times 10^{-6}$$

Event yields are determined from a multi-dimensional unbinned maximum likelihood fit. The decay rate asymmetry in the channels $B^0 \to \pi^\pm K^\mp$, $B^\pm \to \pi^0 K^\pm$, $B^\pm \to \pi^\pm K^0_S$, has also been measured. The results are given below:

$$A_{CP} \equiv \frac{\Gamma(\overline{B}^0 \to K^-\pi^+) - \Gamma(B^0 \to K^+\pi^-)}{\Gamma(\overline{B}^0 \to K^-\pi^+) + \Gamma(B^0 \to K^+\pi^-)} = -0.06 \pm 0.12(\mathrm{stat}) \pm 0.07(\mathrm{syst})$$

$$A_{CP} \equiv \frac{\Gamma(B^- \to K^-\pi^0) - \Gamma(B^+ \to K^+\pi^0)}{\Gamma(B^- \to K^-\pi^0) + \Gamma(B^+ \to K^+\pi^0)} = 0.07 \pm 0.18(\mathrm{stat}) \pm 0.06(\mathrm{syst})$$

$$A_{CP} \equiv \frac{\Gamma(B^- \to K^0_S\pi^-) - \Gamma(B^+ \to K^0_S\pi^+)}{\Gamma(B^- \to K^0_S\pi^-) + \Gamma(B^+ \to K^0_S\pi^+)} = +0.35 \pm 0.23(\mathrm{stat}) \pm 0.08(\mathrm{syst})$$

Acknowledgements

I would like to thank Paul Dauncey for having been a wonderful supervisor. He has been a great support and it has been a pleasure to work with him. Also, many thanks to Jordan Nash for his help and guidance while I was working at SLAC. I would also like to thank Professor Peter Dornan for giving me the opportunity to work in the Imperial College High Energy Physics Group. I must also thank the PPARC for providing me with generous funding.

Particular thanks go to Peter Sanders for the time he spent helping me get to grips with the BaBar code and his clear explanations of some difficult concepts. Thanks also to the other members of the IC BaBar group; Ulrik Egede, Ivo Escherich, Geoff Morton, Naveen Gunawardane and Dan Bowerman. Their help was invaluable.

The opportunity to work at SLAC was the chance of a lifetime. I have such happy memories of being there and I met and worked with some wonderful and brilliant people. Rowan Hamilton was my best friend and he's one of a kind! Thanks for the heady mix of intellectualism, humour and gunpowder! Thanks also to the rest of the 'Harvard Trio', Colin Jessop and Tom Dignan. I would also like to thank Gregory Dubois-Felsmann for many interesting discussions and cups of tea! Thank you to Alex Romosan for his friendship, philosophy, poetry and time spent in Berkeley and Pasadena with George and Gordon. Thanks also to Hooman Davoudiasl and Gudrun Hiller, 'The Theorists', for being great friends, and of course, New York 2000.

Away from SLAC, it was a pleasure to get to know Robert Goyette and Will Sandoval. Will's place in EPA was the venue for some unforgettable parties!

The IC HEP group has been a great place to work. I'd like to thank Elaine McLeod, Robert Illingworth, Richard 'Whitey' White, Riccardo Goncalo, Rod Walker and

Alex Tapper for helping me aquire the taste for beer and lively political debate! Barry MacEvoy has shown me the humourous, but sometimes disturbing, side of paranoia, romance and life as a South London slum landlord. On a more serious note, thanks to Julia Sedgebeer and John Hassard for giving me the chance to do my PhD at IC. It's been a rich educational experience.

Special thanks go to Carsten Kueppersbusch for being such a loyal and wonderful friend for so long. Many other friends have put up with me while I've been writing this thesis - thanks to Konrad Scheffler and my housemates, Sofia Olhede, Yuko Nagai and Katherine Sisson.

Finally, I'd like to thank my parents, Roy and Margaret, for their unconditional love, support and encouragement.

Marie Louise Aspinwall

London, January 2002.

Contents

List of Figures

List of Tables

Preface

0.1 A Brief History of CP Violation

The realisation of a connection between physical laws and symmetry can certainly be traced back as far as Newton, and possibly even to the ancient Greeks. However, the connection as we understand it today was perceived by Emmy Noether in 1918. Noether's Theorem [1] elegantly states the dynamical implications of symmetry:

$$\text{SYMMETRIES} \Longleftrightarrow \text{CONSERVATION LAWS}$$

Physics symmetries may be categorised into four main groups. Space-time, gauge, permutation and discrete symmetries, the first two being continuous symmetries (see table 1). According to Noether's Theorem, every symmetry yields a conserva-

Type of Symmetry	Examples
Space-time	Translations in space and time, rotations in space, Lorentz transformations
Discrete	Charge conjugation, Parity and Time reversal
Gauge	U(1), SU(2) and SU(3) symmetries
Permutation	Fermi-Dirac, Bose-Einstein statisics

Table 1: Types of Symmetry.

tion law, and every conservation law reveals an underlying symmetry. For example, for a system invariant under translations in space, linear momentum is conserved. If the system remains invariant under translations in time, energy is conserved. Conversely, conservation of angular momentum implies a system is symmetric under rotations about a point. An example of a gauge symmetry, and its conserved

quantity, is the invariance of the Lagrangian describing electrodynamics under U(1) transformations, and the conservation of electric charge.
The symmetries of interest for this thesis are the discrete symmetries, explicitly,

- Charge conjugation (C), where particles a replaced by antiparticles
- Parity (P), in which the space axes are inverted
- Time reversal (T), where the direction of time is inverted

and their combinations CP and CPT.
In 1947 particle phyics seemed well understood. There were the constituents of atoms - the proton, neutron and electron, and the pion (thought to be responsible for binding the nuclei of atoms together) had been discovered, as had the positron, which had been postulated by Dirac. The neutrino had not been observed, but was thought to be understood. The muon seemed to be the only real enigma. Then in 1947 the K^0 was found (known then as the θ^0) in cosmic ray interactions and shortly afterwards the K^+ (first called the τ^+) [2]. These kaons behaved in some respects like pions and the meson family were extended to include them. Over the next few years a proliferation of particles, both mesons and baryons, were discovered. A subset of these particles, including the kaons, were labeled 'strange' because they were created on a short time scale, $\sim 10^{-23}$ seconds, but had a relatively long lifetime of $\sim 10^{-10}$ seconds. This suggested a different mechanism for production and decay. We now know that they are created via the stong interaction and decay via the weak. A property called 'stangeness' was introduced, analogous to electric charge, which is conserved in the strong and electromagnetic interactions but is not conserved in the weak interactions. In 1956, the K^+ was thought to be two different particles; the θ^+, which decayed to two pions, a state of parity $P = +1$, and the τ^+, which decayed to the $P = -1$ three pion state. Lee and Yang [3] thought it odd that two otherwise identical particles should carry different parity and wondered if the θ^+ and τ^+ were actually the same particle, and parity was violated in one of the decays. They suggested an experiment to test parity invariance. The result of the experiment to measure β-decay in polarised Cobalt 60 atoms was that parity was found to be maximally violated by the weak interaction.

It had already been shown that any Lorentz invariant local field theory was necessarily invariant under the combined CPT transformation. There was no reason to suppose that physical laws were not invariant under C, P and T individually. However, now that P had been shown to be violated in the weak interaction, at least one of C and T must be violated too, in order to conserve CPT. The discovery that only a left-handed neutrino and a right-handed antineutrino exist showed that C was also maximally violated by the weak interaction - since the action of C on a left-handed neutrino produced a left-handed antineutrino, a particle never observed. After the shock of the discovery of P violation, the realisation that the combined CP operation seemed to be a good symmetry for the weak interactions was some comfort.

CP violation was observed in the K^0 system [6] in 1964, and since then similar neutral particle systems have been observed; namely the B^0 and D^0. It was natural to wonder if CP violation would be exhibited by these particles as well. The non-conservation of CP symmetry was introduced to the Standard Model in 1973 [17] by the appearance of complex phases in the Cabibbo-Kobayashi-Maskawa (CKM) matrix, which also inferred the existence of the b and t quarks. The CKM matrix describes the weak charge-changing transitions of quarks. The Standard Model predicted CP asymmetries between partial rates of B mesons and their corresponding antiparticles. The expected CP violation in the B^0 meson system was observed in 2001 by both the BaBar and Belle experiments [9] [10].

The field of B physics has become an important arena in which to investigate the phenomenon of CP violation. The suggestion that a sizeable asymmetry could be measured in the decays of B mesons to a pair of charmless pseudoscalar mesons (*e.g.* $B \to \pi K$ decays) has inspired the search for such decays and the elusive asymmetry. The first observation of $B \to \pi K$ [24] decays was at the CLEO experiment in 1999. This thesis presents a search for $B \to \pi K$ decays and a measurement of their branching fractions at BaBar and a measurement of asymmetry effects.

0.2 Author's Contribution

As part of my PhD course I spent fifteen months working at the Stanford Linear Accelerator Center (SLAC). My time there coincided with BaBar's first year of running. I took on several tasks while I was there, which mainly consisted of working on the detector's Electromagnetic Calorimeter (EMC), given the fact that this device was the main responsibility of UK collaborators. Imperial College was responsible for the main EMC electronics, and I spent many hours carrying out maintenance tasks on the EMC electronics components located on the detector. After BaBar came online in May 1999, I was able to analyse real data. I carried out a study of π^0 detection in the EMC, which determined the resolution of π^0 decaying to two photons at various energies. During the second year of my PhD I commenced my analysis of $B \to \pi K$.

0.3 Outline of Thesis

Chapter 1 gives a brief account of CP violation in the context of the B meson system. The motivation for measuring the branching fractions of $B \to \pi K$ decays is presented. The relevance of such measurements to the determination of the decay asymmetries and the eventual calculation of the CKM angle γ using these branching fractions is discussed. Chapter 2 describes the BaBar detector and the PEP-II B Factory. Chapter 3 outlines my work on a cut-and-count based analysis, while Chapter 4 describes a Maximum Likelihood analysis of $B \to \pi K$ on the Run 1 data collected at BaBar between 1999 and 2000.

Chapter 1

Theoretical Synopsis

1.1 Introduction

The violation of CP conservation was observed in the K^0 system in 1964 [6]. A neutral kaon mass eigenstate is not a pure CP eigenstate. The long-lived kaon, K_L^0, which is mainly CP = -1, has a small amplitude to decay to two pions, a CP = +1 state. The phenomenon of CP violation was unambiguously demonstrated by the observation of $K_L^0 \to \pi^+ \pi^-$. In field theory terms, the Lagrangian describing interactions does not remain invariant under the combined CP transformation. CP violation occurs in any field theory which has complex terms in the Lagrangian, which cannot be made real by any (complex) phase transformation. It is understood that CP violation is a crucial feature of any theory which attempts to explain the asymmetry between matter and antimatter in the universe [7]. It is also a natural feature of the three generation Standard Model. The discovery of the b quark from the decay of $\Upsilon(4S)$ in 1977 [8] opened up the possibility of using the B meson system to test CP violation. One beauty of the B meson system is the great variety of channels that can be studied. The BaBar experiment at SLAC is primarily a B physics laboratory. Recent results from BaBar (and the Belle experiment in Japan) have observed CP violation in B mesons and measured a significant CP asymmetry as predicted by the Standard Model [9] [10]. This thesis is a study of the rare $B \to \pi K$ decays, which have branching fractions of $\mathcal{O}(10^{-5})$. The ratio of partial decay rates for charged and neutral B mesons to πK provides information on the weak phase (see equation 1.10 below) when augmented with information on the CP violating decay asymmetry in the $B \to \pi K$ processes [15].

1.2 The Standard Model and CP Violation

Flavour changing weak interactions in the Standard Model are mediated by the coupling of the charged current

$$\mathcal{L}_{CC} = \frac{-g}{\sqrt{2}} \mathcal{J}^{\mu}_{CC} W^{\dagger}_{\mu} + h.c. \tag{1.1}$$

where,

$$\mathcal{J}^{\mu}_{CC} = (\bar{\nu}_e, \bar{\nu}_\mu, \bar{\nu}_\tau)\gamma^\mu \begin{pmatrix} e_L \\ \mu_L \\ \tau_L \end{pmatrix} + (\bar{u}_L, \bar{c}_L, \bar{t}_L)\gamma^\mu V_{CKM} \begin{pmatrix} d_L \\ s_L \\ b_L \end{pmatrix} \tag{1.2}$$

contains the left-handed lepton and quark fields, and

$$V_{CKM} = \begin{pmatrix} V_{ud} & V_{us} & V_{ub} \\ V_{cd} & V_{cs} & V_{cb} \\ V_{td} & V_{ts} & V_{tb} \end{pmatrix} \tag{1.3}$$

gives the famous CKM 3 x 3 mixing matrix [16]. V_{CKM} can be parameterised by three Euler angles and six phases, five of which can be removed by adjusting the relative phases of the left-handed quark fields. Hence, three angles and one observable complex phase δ remain in the quark mixing matrix, as was shown by Kobayashi and Maskawa in 1973 [17]. The imaginary part of the mixing matrix is necessary to describe CP violation in the Standard Model. The values of the individual matrix elements can in principle all be determined from weak decays of the relevant quarks, or in some cases, from deep inelastic neutrino scattering. The 90% confidence limits on the magnitudes of the matrix elements are currently [18]:

$$V_{CKM} = \begin{pmatrix} 0.9742 - 0.9757 & 0.219 - 0.226 & 0.002 - 0.005 \\ 0.219 - 0.225 & 0.9734 - 0.9749 & 0.037 - 0.043 \\ 0.004 - 0.014 & 0.035 - 0.043 & 0.9990 - 0.9993 \end{pmatrix} \tag{1.4}$$

The CKM matrix has many different representations. The one below [19] is the parameterisation favoured by the Particle Data Group,

$$V_{CKM} = \begin{pmatrix} c_{12}c_{13} & s_{12}c_{13} & s_{13}e^{-i\delta} \\ -s_{12}c_{23} - c_{12}s_{23}s_{13}e^{i\delta} & c_{12}c_{23} - s_{12}s_{23}s_{13}e^{i\delta} & s_{23}c_{13} \\ s_{12}s_{23} & -c_{12}c_{23} - s_{12}c_{23}s_{13}e^{i\delta} & c_{23}c_{13} \end{pmatrix} \tag{1.5}$$

where $c_{ij} = \cos\theta_{ij}$, $s_{ij} = \sin\theta_{ij}$ for $(i, j = 1, 2, 3)$ and θ_{ij} are real angles and δ is the aforementioned complex phase factor. The CKM matrix can also be written in the standard Wolfenstein parameterisation [20]. In doing this, the elements of the CKM matrix are expanded in a power series in terms of the parameter $\lambda = |V_{us}|$ to give,

$$V_{CKM} \simeq \begin{pmatrix} 1-\frac{\lambda^2}{2} & \lambda & A\lambda^3(\rho - i\eta) \\ -\lambda & 1-\frac{\lambda^2}{2} & A\lambda^2 \\ A\lambda^3(1-\rho-i\eta) & -A\lambda^2 & 1 \end{pmatrix} + \mathcal{O}(\lambda^4) \tag{1.6}$$

Here, $s_{12} = \lambda$, $s_{23} = A\lambda^2$, $s_{13} = A\sqrt{\rho^2+\eta^2}\lambda^3$ and $\delta = \tan^{-1}(\eta/\rho)$. CP violation requires that the above unitary matrix must be complex, therefore, $\eta \neq 0$. The unitarity nature of the CKM matrix can be exploited to yield nine unitary relations [21]. Of these, the one that is of interest to us for the B meson system is,

$$V_{ud}V_{ub}^* + V_{cd}V_{cb}^* + V_{td}V_{tb}^* = 0. \tag{1.7}$$

Geometrically, the above is an equation of a triangle in the complex plane. This triangle, most commonly known as the Unitarity Triangle, is shown in figure 1.1. The three angles, α, β and γ, of the above triangle can be defined as,

$$\alpha = arg(-\frac{V_{td}V_{tb}^*}{V_{ud}V_{ub}^*}) \tag{1.8}$$

$$\beta = arg(-\frac{V_{cd}V_{cb}^*}{V_{td}V_{tb}^*}) \tag{1.9}$$

$$\gamma = arg(-\frac{V_{ud}V_{ub}^*}{V_{cd}V_{cb}^*}) \tag{1.10}$$

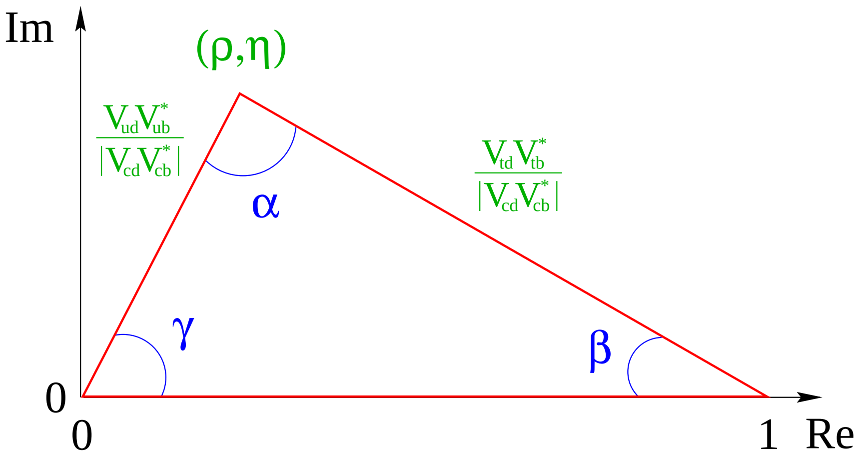

Figure 1.1: *The Unitarity Triangle*

1.3 CP Violation in B Meson Decays

In the previous section the appearance of CP violation in the Standard Model was discussed. In this section the connection of CP violation to the phenomenology of B meson decays will be covered [22]. There are three types of CP violation in B meson decays:

- CP violation in mixing, which occurs when the two neutral mass eigenstates cannot be chosen to be CP eigenstates:

- CP violation in decay, which occurs in both charged and neutral decays, when the amplitude for a decay and its CP-conjugate process have different magnitudes;

- CP violation in the interference of decays with and without mixing, which occurs in decays to final states that are common to B^0 and $\overline{B}^0$.

The decays of $B \rightarrow \pi K$ are expected to give rise to CP violation in decay, and this is, therefore, the main focus of this section. However, some mention of the other two forms of CP violation will also be made.

1.3.1 Formalism

The time evolution of a state ψ is governed by the time dependent Schrödinger equation,

$$i\frac{d}{dt}\psi = \mathcal{H}\psi \tag{1.11}$$

with the form of the non-Hermitian Hamiltonian, $\mathcal{H}$, being constrained by the CPT symmetry [11] [12]. The Hamiltonian, can in fact, be written in terms of two Hermitian components; the so-called Mass matrix ($\mathcal{M}$) and the Disintegration matrix (Γ) such that,

$$\mathcal{H} = \mathcal{M} - \frac{i}{2}\Gamma \tag{1.12}$$

The mass eigenstates of the B meson system, B_L^0 and B_H^0, can be expressed in terms of the flavour eigenstates, B^0 and $\overline{B}^0$. The B_L^0 and the B_H^0, which are referred to as the "light" and "heavy" states respectively, can be expanded in terms of the flavour eigenstates as,

$$|B_L^0\rangle = p|B^0\rangle + q|\overline{B}^0\rangle \tag{1.13}$$

$$|B_H^0\rangle = p|B^0\rangle - q|\overline{B}^0\rangle \tag{1.14}$$

with the parameters p and q subject to the normalisation condition,

$$|p|^2 + |q|^2 = 1 \tag{1.15}$$

The mass and the width differences between the two mass eigenstates are defined as,

$$\Delta m_d = M_H - M_L \tag{1.16}$$

$$\Delta\Gamma_B = \Gamma_H - \Gamma_L \tag{1.17}$$

Solving the eigenvalue equation, it can be show that,

$$\Delta m_d^2 - \frac{1}{4}(\Delta\Gamma_B)^2 = 4(|M_{12}|^2 - \frac{1}{4}|\Gamma_{12}|^2) \tag{1.18}$$

$$\Delta m_d \Delta\Gamma_B = 4\mathcal{R}e\,(M_{12}\Gamma_{12}^*) \tag{1.19}$$

and

$$\frac{q}{p} = -\frac{2M_{12}^* - i\Gamma_{12}^*}{\Delta m_d - \frac{i}{2}\Gamma_{12}} = -\frac{\Delta m_d - \frac{i}{2}\Delta\Gamma_B}{2M_{12} - i\Gamma_{12}} \tag{1.20}$$

In the B system, using the observation that $|\Gamma_{12}| << |M_{12}|$, gives,

$$\Delta m_d = 2|M_{12}| \tag{1.21}$$

$$\Delta\Gamma_B = \frac{2\mathcal{R}e(M_{12}\Gamma_{12}^*)}{M_{12}} \tag{1.22}$$

and to leading order, the ratio $\left(\frac{q}{p}\right)$, can be written as,

$$\frac{q}{p} = -\frac{M_{12}^*}{|M_{12}|}\left[1 - \frac{1}{2}\mathcal{I}m\left(\frac{\Gamma_{12}}{M_{12}}\right)\right] \tag{1.23}$$

1.3.2 CP Violation in Mixing

Inspection of q and p in equation 1.23 shows that if CP is conserved the relative phase between M_{12} and Γ_{12} must vanish. In fact there is still a phase between q and p but one which can be accounted for by a suitable definition of the B - $\overline{B}$ phase difference, which we are free to choose. This gives,

$$|\frac{q}{p}| \neq 1 \tag{1.24}$$

This is CP violation in mixing. It is also called 'Indirect CP Violation'. It arises because the mass eigenstates are different from the CP eigenstates. This form of CP violation has been unambiguously observed in the K^0 system. At BaBar, mixing in the B meson system has been observed by studying semileptonic B decays. A measurement of the time dependent asymmetry,

$$a_{sl} = \frac{\Gamma(\overline{B}^0(t) \to l^- \bar{\nu}_l X) - \Gamma(B^0(t) \to l^+ \nu_l X)}{\Gamma(\overline{B}^0(t) \to l^- \bar{\nu}_l X) + \Gamma(B^0(t) \to l^+ \nu_l X)} \tag{1.25}$$

would provide evidence for CP violation in mixing. This effect was measured by BaBar [13] during its first year of running, and was found to be of $\mathcal{O}(10^{-2})$.

1.3.3 CP Violation in the Interference between Mixing and Decay

Consider the decay of a mixed state into a CP eigenstate. Let η_{CP} be a CP eigenstate and H be the Hamiltonian that governs the decay.

$$A = \langle \eta_{CP} | \hat{H} | B^0 \rangle \tag{1.26}$$

for the $\overline{B}^0$ and,

$$\bar{A} = \langle \eta_{CP} | \hat{H} | \overline{B}^0 \rangle. \tag{1.27}$$

The physically meaningful phase convention independent quantity here is the parameter λ, defined as,

$$\lambda = \frac{q\bar{A}}{pA}. \tag{1.28}$$

What is of interest are the time dependent amplitudes that are given by,

$$\langle \eta_{CP} | \hat{H} | B^0(t) \rangle = A\Big(f_+(t) + \lambda f_-(t)\Big) \tag{1.29}$$

$$\langle \eta_{CP} | \hat{H} | \overline{B}^0(t) \rangle = A\frac{p}{q}\Big(f_-(t) + f_+(t)\Big) \tag{1.30}$$

The decay rate of the B^0 to a CP eigenstate is then given by,

$$\Gamma(B^0(t) \to \eta_{CP}) \propto |\langle \eta_{CP}|\hat{H}|B^0(t)\rangle|^2 \tag{1.31}$$

$$\Gamma(B^0(t) \to \eta_{CP}) \propto |A|^2 e^{-\Gamma t}\left[\left(\frac{1+|\lambda|^2}{2}\right)+\left(\frac{1+|\lambda|^2}{2}\right)\cos(\Delta m_d t)-\mathcal{I}m(\lambda)\sin(\Delta m_d t)\right] \tag{1.32}$$

Similarly, it can be shown that for the $\overline{B}^0$, the decay rate is given by,

$$\Gamma(\overline{B}^0(t) \to \eta_{CP}) \propto |A|^2 e^{-\Gamma t}\left[\left(\frac{1+|\lambda|^2}{2}\right)-\left(\frac{1+|\lambda|^2}{2}\right)\cos(\Delta m_d t)+\mathcal{I}m(\lambda)\sin(\Delta m_d t)\right] \tag{1.33}$$

The main point is that these amplitudes have two contributions, one from the direct decay of the B^0 to the η_{CP} state and one from the mixing of the B^0 into a $\overline{B}^0$ which then decays to a η_{CP} state.

1.3.4 CP Violation in Decay

To discuss CP violation in decay, we need to consider decay amplitudes. The amplitudes of the B^0 and $\overline{B}^0$ may written,

$$A = \langle f|\hat{H}|B^0\rangle \tag{1.34}$$

for the B^0 and,

$$\bar{A} = \langle \bar{f}|\hat{H}|\bar{B}^0\rangle \tag{1.35}$$

for the $\overline{B}^0$. Complex CKM parameters in the Lagrangian that contribute to the amplitudes will appear in a complex conjugate form in the CP conjugate amplitude. Such phases will therefore have opposite signs in the amplitudes, A and $\bar{A}$. In the Standard Model such complex phases arise only from the Electroweak sector of the theory via the CKM matrix. Hence they are called 'weak phases' and are convention dependent, while their differences are convention independent. It is also possible for scattering/decay amplitudes to contain phases even when the Lagrangian is real. These phases, known as 'strong phases', as they can arise from strong interactions, occur in A and $\bar{A}$ with the same sign and do not violate CP. Again, what is of importance is the relative strong phase difference and not the overall phase. Thus, the decay amplitude can be written in three parts: its magnitude A; the weak phase term $e^{i\phi}$; and the strong phase term $e^{i\delta}$. If several amplitudes contribute to A, A can be written as,

$$A = \sum_i A_i e^{i(\delta_i + \phi_i)} \tag{1.36}$$

and

$$\frac{\bar{A}}{A} = \frac{\sum_i A_i e^{i(\delta_i - \phi_i)}}{\sum_i A_i e^{i(\delta_i + \phi_i)}} \tag{1.37}$$

Inspection of the amplitudes tells us that in the case of CP conservation the weak phases are equal. This leads to a relative phase between the two amplitudes, but one which can be set to zero. Therefore, CP violation occurs if,

$$|\frac{\bar{A}}{A}| \neq 1 \tag{1.38}$$

This is CP violation in decay, also called 'Direct CP violation'. It is a result of interference between the various terms in the decay amplitudes. Direct CP violation will therefore only be observed if at least two terms have different weak and strong phases. For the simplest case where two such phases exist, the rates can be written as,

$$\Gamma_1 \propto |A_1 e^{i(\delta_1 + \phi_1)} + A_2 e^{i(\delta_2 + \phi_2)}|^2 \tag{1.39}$$

$$\Gamma_2 \propto |A_1 e^{i(\delta_1 - \phi_1)} + A_2 e^{i(\delta_2 - \phi_2)}|^2 \tag{1.40}$$

giving,

$$\Gamma_1 - \Gamma_2 \propto 2 A_1 A_2 \sin(\phi_1 - \phi_2) \sin(\delta_1 - \delta_2) \tag{1.41}$$

Asymmetries in charged B decays are only due to direct CP violation,

$$a_f \equiv \frac{\Gamma(\mathrm{B}^- \to \bar{f}) - \Gamma(\mathrm{B}^+ \to f)}{\Gamma(\mathrm{B}^- \to \bar{f}) + \Gamma(\mathrm{B}^+ \to f)} \tag{1.42}$$

Direct CP violation can also occur in neutral meson decays, but in this case the CP violation in decay may compete with the other two manifestations of CP violation, already described.

1.4 Rare Charmless Hadronic B Decays

The processes $B \to \pi K$ and $B \to \pi\pi$ have been identified as possible sources of Direct CP violation. Hadronic B meson decays occur primarily through the CKM favoured $b \to c$ transition. However, rare decays, such as $B \to \pi\pi$, can proceed via a CKM-suppressed $b \to u$ transition. These decays are suppressed since the CKM matrix element $|V_{ub}|$ is small. Therefore, additional diagrams may contribute significantly to these decay amplitudes. The most significant of these is the one-loop flavour-changing neutral current "penguin" diagram. This diagram consists of a $b \to s$ transition. The contribution of this $b \to s$ is expected to be significant in $B \to \pi K$ decays.

The Feynman diagrams contributing to both $B \to \pi K$ and $B \to \pi\pi$ can be summarised as follows (figure 1.2). The unprimed amplitudes denote strangeness-preserving decays, whereas the primed amplitudes indicate strangeness-changing transitions [15]. Top left is a "colour-allowed" external W emission "tree" process

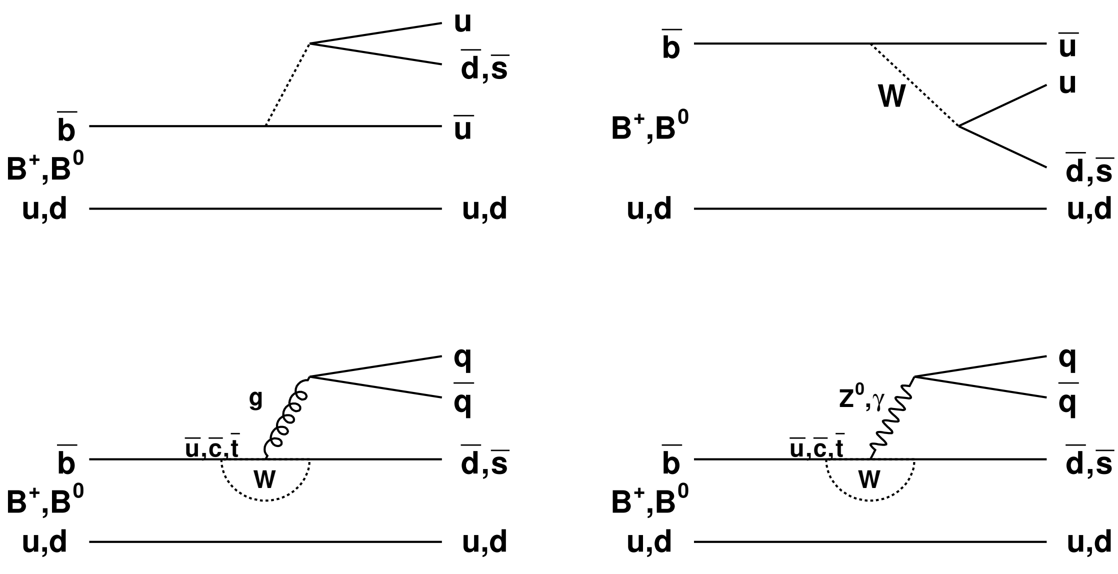

Figure 1.2: *Top left: external W emission, Top right: internal W-emission, Bottom left: gluonic penguin and Bottom right: electroweak penguin.*

T (T'), top right is a "colour-suppressed" internal W transition C (C'), bottom left is the $b \to dg$ or $b \to sg$ gluonic penguin P (P') and bottom right is an electroweak penguin P_{EW} (P'_{EW}). The extent of the electroweak penguin contributions is not well known and will be discussed later on in this section. The amplitudes of $B \to \pi K$ and $B \to \pi\pi$ are combinations of tree and penguin contributions. Below is a list of the types of transition involved in the $\Delta S = 1$ $B \to \pi K$ decay channels and the $\Delta S = 0$ $B \to \pi\pi$ channels.

channel	P'	C'	T'
$B^0 \to \pi^{\pm}K^{\mp}$	$\surd$		$\surd$
$B^{\pm} \to \pi^0 K^{\pm}$	$\surd$	$\surd$	$\surd$
$B^{\pm} \to \pi^{\pm}K^0_S$	$\surd$		
$B^0 \to \pi^0 K^0_S$	$\surd$	$\surd$	
	P	C	T
$B^0 \to \pi^{\mp}\pi^{\pm}$	$\surd$		$\surd$
$B^{\pm} \to \pi^{\pm}\pi^0$	$\surd$	$\surd$	$\surd$
$B^0 \to \pi^0\pi^0$	$\surd$	$\surd$	

Table 1.1: The penguin and tree contributions to $B \to \pi K$ and $B \to \pi\pi$.

In $B \to \pi K$ decay channels, it is thought that the $b \to sg$ gluonic penguin will form the dominant contribution to the decay amplitude, as $P < P'$ since $|V_{td}| < |V_{ts}|$ in the ratio 1:4. The $\overline{b} \to \overline{d}u\overline{u}$ tree diagram is expected to dominate the decay amplitude in $B \to \pi\pi$ channel, as $T, C > T', C'$, because $|V_{ud}| > |V_{us}|$ in the ratio 5:1.

By studying $B \to \pi K$ we could gain an insight into the penguin process and similarly $B \to \pi\pi$ would gives us information regarding the tree diagrams.

1.4.1 Direct CP Violation in Charmless Rare B Decays

As previously described the difference between rates for $B \to f$ and $\overline{B} \to \bar{f}$ will occur in any decay mode for which there are two or more contributing amplitudes which differ in both weak and strong phases. This rate difference gives rise to an asymmetry A_{CP}, expressed in terms of the magnitudes of the branching fractions for $B \to \pi K$ and $B \to \pi\pi$ decay channels. From an experimental point of view the $B^0 \to \pi\pi$ channels require the flavour of the decaying B to be tagged, which is rather complicated in these modes. The $B \to \pi K$ modes, however, have the advantage that the modes $B^0 \to \pi^- K^+$, $B^- \to \pi^0 K^-$, and $B^- \to \pi^- K^0_S$ and their charge conjugates are "self-tagging". Interference between the penguin and tree amplitudes could lead to a CP violating effects which would be evident if the values of A_{CP} in equations 1.43, 1.44, 1.45 are non-zero.

$$A_{CP} \equiv \frac{\Gamma(B^0 \to K^-\pi^+) - \Gamma(B^0 \to K^+\pi^-)}{\Gamma(B^0 \to K^-\pi^+) + \Gamma(B^0 \to K^+\pi^-)} \tag{1.43}$$

$$A_{CP} \equiv \frac{\Gamma(B^- \to K^-\pi^0) - \Gamma(B^+ \to K^+\pi^0)}{\Gamma(B^- \to K^-\pi^0) + \Gamma(B^+ \to K^+\pi^0)} \tag{1.44}$$

and

$$A_{CP} \equiv \frac{\Gamma(B^- \to K^0\pi^-) - \Gamma(B^+ \to K^0\pi^+)}{\Gamma(B^- \to K^0\pi^-) + \Gamma(B^+ \to K^0\pi^+)} \tag{1.45}$$

A measurement of the $B \to \pi K$ branching fractions is sufficient to reveal such decay rate asymmetries.

1.4.2 Determination of γ from $B \to \pi K$ Decays

Several ingenious methods of measuring the weak CKM phase $\gamma = Arg(|V_{ub}|^*)$ using only the decay rates of $B \to \pi K$ and $B \to \pi\pi$ processes have been proposed. Such a measurement is of particular importance as γ is the least well known parameter of the Unitarity Triangle, and experimentally the most difficult to measure.

In the methods for measuring γ described in the following sections, decays whose amplitude, A_3, can be expressed as the sum of two contributions, A_1 and A_2, are considered:

$$A_3 = A_1 + A_2 = A_1 + |A_2|e^{i\gamma}e^{i\Delta}. \tag{1.46}$$

Such relations between amplitudes are represented geometrically by a triangle construction in the complex plane. If A_1 and A_2 are the two amplitudes which contribute to a given decay, and if the decay has been chosen such that A_2 has a relative CKM phase γ and a relative strong phase $\Delta = \delta_1 - \delta_2$ with respect to A_1, the situation can be presented as shown in Figure 1.3. $\bar{A}_1$ and $\bar{A}_2$ are the corresponding amplitudes for the $\overline{B}$, where the overall phase convention has been selected such that $\bar{A}_1 = A_1$. In addition, since $|\bar{A}_2| = |A_2|$, one finds

$$A_4 = \bar{A}_1 + \bar{A}_2 = A_1 + |A_2|e^{-i\gamma}e^{i\Delta}. \tag{1.47}$$

The variable Δ is the difference in the strong phases for the two amplitudes and A_3 and A_4 are the two total amplitudes for the decays of the B and $\overline{B}$ respectively.

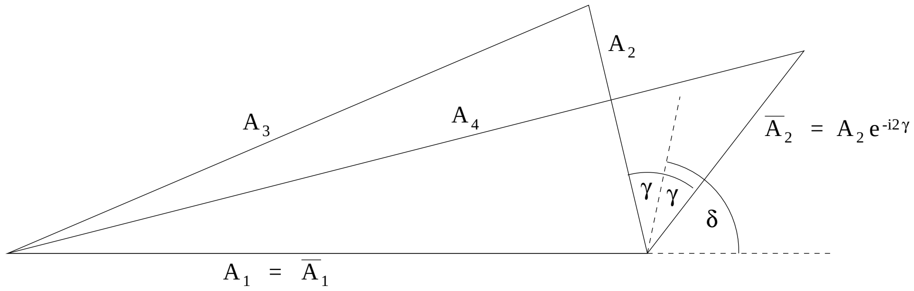

Figure 1.3: *Triangle representation of amplitude relations.*

Direct CP violation manifests itself in the magnitudes of A_3 and A_4 being unequal, if the strong phase δ is different from zero. There are 4 parameters in total for the two triangles corresponding to B and $\overline{B}$; these are taken to be $|A_1|$, $|A_2|$, γ and δ. Gronau, Rosner and London (GRL) [14] proposed an interesting strategy to determine γ using a triangle construction involving the amplitudes for the decays $B^{\pm} \to \pi^0 K^{\pm}$ $B^{\pm} \to \pi^{\pm} K^0_S$ and $B^0 \to \pi^{\pm} K^{\mp}$. The GRL approach uses the $SU(3)$ flavour symmetry of strong interactions, and neglects any electroweak-penguin contributions. However, it was latterly shown that this method is in fact spoiled by electroweak-penguins, which actually play an important role due to the large top quark mass involved in the penguin transition. The colour-allowed “tree” amplitude T' is highly CKM-suppressed. Consequently, one expects that the QCD penguin amplitude P' to play the dominant role and that T' and the colour-allowed EW penguin amplitude P'_{EW}, which contributes to $B^{\pm} \to \pi^0 K^{\pm}$ are equally important:

$$\left|\frac{T'}{P'}\right| = \mathcal{O}(0.20), \quad \left|\frac{P'_{\mathrm{EW}}}{T'}\right| = \mathcal{O}(1.0). \tag{1.48}$$

Fleischer and Mannel proposed a method to extract some information on the angle γ using measurements of the branching fractions of $B^0 \to \pi^{\pm} K^{\mp}$ and $B^{\pm} \to \pi^{\pm} K^0_S$, averaged over CP-conjugate modes [23]. They obtained the bound,

$$R = \frac{\mathcal{B}(B^0 \to \pi^{\pm} K^{\mp})}{\mathcal{B}(B^{\pm} \to \pi^{\pm} K^0_S)} \geq \sin^2\gamma, \tag{1.49}$$

which would exclude a region around $\gamma = 90°$ provided that $R < 1$, a possibility allowed by the first measurement of this ratio by the CLEO Collaboration, yielding $R = 0.65 \pm 0.40$ [24]. It has later been realised that the bound 1.49 may be subject to effects arising from final-state interactions and also colour-suppressed electroweak-penguin contributions [25]. Such effects would require studies of $B \to KK$ channels [26]. In addition to these theoretical obstacles, the prospects for deriving useful information on γ from R are further diminished by the CLEO Collaboration announcing a value of R of $R = 1.0 \pm 0.4$ [27]. Neubert and Rosner proposed using the decays $B^{\pm} \to \pi^{\pm} K_S^0$ and $B^{\pm} \to \pi^0 K^{\pm}$ [28] to extract information on γ. Their method is theoretically cleaner than the Fleischer-Mannel method, taking into account any electroweak-penguin contributions and rescattering effects. The ratio R_*,

$$R_* = \frac{\mathcal{B}(B^{\pm} \to \pi^{\pm} K_S^0)}{2\mathcal{B}(B^{\pm} \to \pi^0 K^{\pm})} \leq \cos\gamma. \tag{1.50}$$

gives a bound on $\cos\gamma$ of ≈ 0.6 [29]. The main disadvantage with this method is that a knowledge of (T+C)/P of spectator to penguin amplitudes in $b \to s$ transitions is required.

1.4.3 Information from Neutral B Decays

The neutral decays $B^0 \to \pi^0 K_S^0$ and $B^0 \to \pi^{\pm} K^{\mp}$ might provide an additional CP violating observable [30], which could also take into account rescattering effects in a theoretically clean way. $B^0 \to \pi^{\pm} K^{\mp}$ is a self-tagging neutral decay, it exhibits only CP violation due to the interference between the "tree" (T) and "penguin" (P) amplitudes, but no mixing-induced CP violation, arising from interference effects between $B - \overline{B}$ mixing and decay processes. $B^0 \to \pi^0 K_S^0$, however, results in a final state which is an eigenstate of the CP operator with eigenvalue -1. In this case, mixing induced CP violation has occured and a time dependent CP asymmetry appears,

$$a_f \equiv \frac{\Gamma(\overline{B}^0(t) \to \bar{f}) - \Gamma(B^0(t) \to f)}{\Gamma(\overline{B}^0(t) \to \bar{f}) + \Gamma(B^0(t) \to f)} \tag{1.51}$$

which can be written:

$$A_{CP}^{dir}(B^0 \to f)\cos(\Delta m_d t) + A_{CP}^{mix-ind}(B^0 \to f)\sin(\Delta m_d t) \tag{1.52}$$

The mixing induced part of this expression can be determined from the measurement of $\sin 2\beta$. However, due to the difficulties of measuring the decay vertex of $B^0 \to \pi^0 K_S^0$ as a function of time, this is not considered to be a realistic method of observing CP violation.

Chapter 2

The PEP-II B Factory and the BaBar Detector

2.1 The PEP-II B Factory

2.1.1 Introduction

The main purpose of an asymmetric B Factory is the systematic study of CP violation in the B meson system. Asymmetric beam energies facilitate the measurement of time dependent CP violating asymmetries in the decay of neutral B mesons. Such asymmetries are expected to be large, so that relatively small samples of events are required. However, B decay channels of interest have extremely small branching fractions, of $\mathcal{O}(10^{-4})$ or below. Therefore samples of tens of millions of B meson pairs must be produced if asymmetries are to be measured with errors at the 10 % level or better. PEP-II [41], the e^+e^- collider at SLAC, was designed to achieve unprecedented luminosities (3.0 x 10^{33} cm^{-2}s^{-1}). This has been exceeded and a luminosity of 3.7 x 10^{33} cm^{-2}s^{-1} has been recorded. The Run 1 data set (figure 2.1), which is used in this dissertation, corresponds to 22 fb^{-1}, about 23 million $B^0\overline{B}^0$ pairs. The 9 GeV electron beam collides with the 3.1 GeV positron beam at the interaction point (IP) inside the BaBar detector [42] with a centre-of-mass (cm) energy of 10.58 GeV, the mass of the $\Upsilon(4S)$ resonance. This resonance decays only to $B^0\overline{B}^0$ and B^+B^- pairs. The asymmetric beam energies results in a Lorentz boost to the $\Upsilon(4S)$ resonance of $\beta\gamma = 0.56$. The boost allows the decay vertices of the B mesons to be reconstructed with a measurable separation. Their relative decay times can, therefore, be determined and thus the time dependence of their decay rates can be measured.

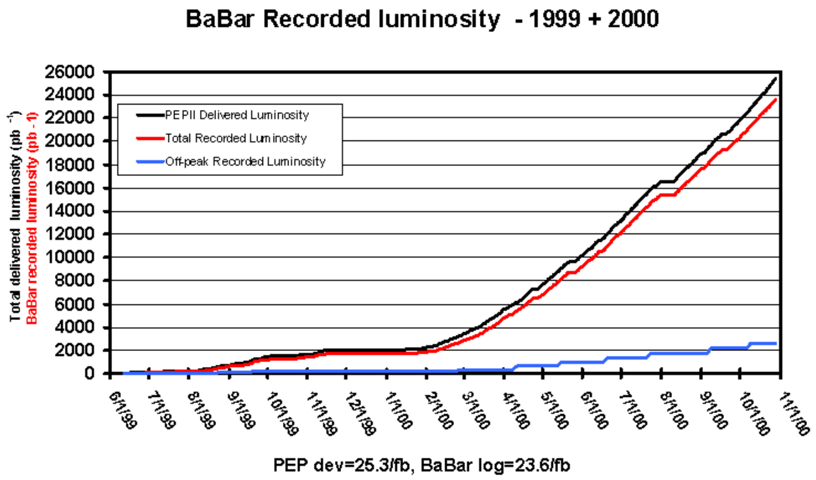

Figure 2.1: *Integrated luminosity of Run 1.*

2.1.2 The PEP-II Storage Rings

The unequal beam energies require a two ring configuration: electrons in a High Energy Ring (HER) colliding with positrons in a Low Energy Ring (LER). Some parameters of the storage rings are presented in table 2.1 which lists both the design values and the values typically obtained during colliding beam operation in this first year after turn on. The LER is located above the HER in the PEP-II tunnel. PEP-II has been an enormous success and has surpassed its design goals both in terms of instantaneous and integrated luminosity. PEP-II typically operates on a 40 minute fill cycle. At the end of a fill, it takes about 3 minutes to replenish the beams. If the storage beams are lost it takes approximately 10-15 minutes to refill. BaBar divides the data into runs, defined as periods of three hours or less during which beam and detector conditions are judged to be stable. About 12% of data are taken at a cm energy 40 MeV below the peak of the $\Upsilon(4S)$ to allow studies of non-resonant background.

Parameters	Design	Typical
Energy HER/LER (GeV)	9.0/3.1	9.0/3.1
Current HER/LER (A)	0.75/2.15	0.7/1.3
# of bunches	1658	553-829
Bunch spacing (ns)	4.2	6.3-10.5
σ_{Lx} (μm)	110	120
σ_{Ly} (μm)	3.3	5.6
σ_{Lz} (mm)	9	9
Luminosity (10^{33} $cm^{-2}s^{-1}$)	3	2.5
Luminosity (pb^{-1}/d)	135	120

Table 2.1: Pep-II beam parameters. Values are given both for the design and for typical colliding beam operation in the first year. HER and LER refer to the high energy e^- and low energy e^+ring, respectively. σ_{Lx}, σ_{Ly}, and σ_{Lz} refer to the horizontal, vertical, and longitudinal rms size of the luminous region.

2.1.3 The PEP-II Interaction Region

High beam currents and a large number of closely-spaced bunches are required to produce the high luminosity of PEP-II. Bunches collide head-on and are separated magnetically in the horizontal plane by a pair of dipole magnets (B1), followed by a series of quadrupoles (see figure 2.2). The tapered B1 magnets are located at ± 21 cm either side of the IP. The IP is enclosed by a water cooled pipe of 27.9 mm outer radius, composed of two layers of Beryllium (0.83 mm and 0.53 mm thick) with a 1.48 mm water channel between them. To attenuate synchrotron radiation, the inner surface of the pipe is coated with gold. The beam pipe, permanent magnets and SVT were assembled and aligned and then enclosed in a 4.5 m long carbon fibre support tube, which spans the IP.

2.1.4 Luminosity and Beam Energies

PEP-II provides fast monitoring of the relative luminosity by measuring radiative Bhabha scattering. BaBar obtains the absolute luminosity offline from other QED processes, mainly e^+e^- and $\mu^+\mu^-$. For a data sample of 1 fb^{-1}, the statistical error is less than 1%, while the systematic error on the absolute value of the luminosity is estimated to be about 1.5%. The mean energies of the beams are calculated from the total magnetic bending strength. To ensure data are recorded near the $\Upsilon(4S)$

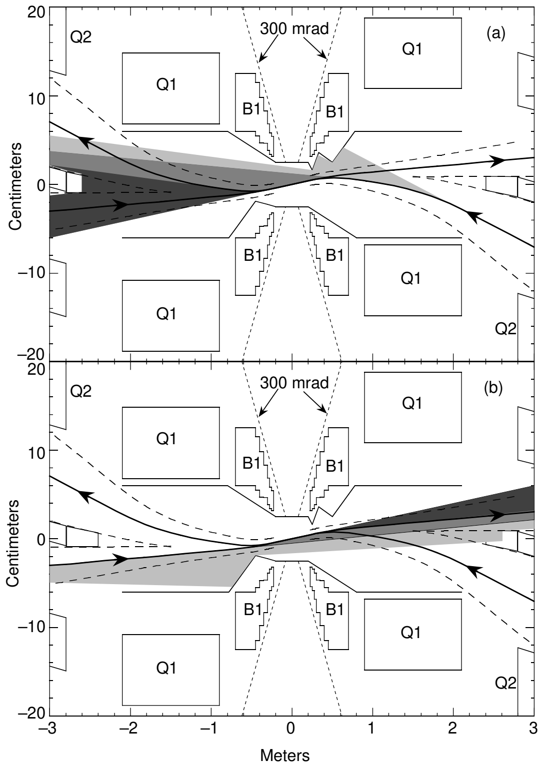

Figure 2.2: *The PEP-II interaction region: The synchrotron radiation deposited by the HER (top) and the LER (bottom).*

resonance peak, the observed ratio of $B\overline{B}$ enriched hadronic events to lepton pair production is monitored online.

2.2 The BaBar Detector

The BaBar detector is a solenoidal spectrometer optimised for the asymmetric beam configuration of PEP-II. Figures 2.3 and 2.4 depict the BaBar detector and the positions of the various subdetectors within it. Charged particle (track) momenta are measured in a tracking system consisting of a 5-layer, double-sided silicon vertex tracker (SVT) and a 40-layer drift chamber (DCH) filled with a gas mixture of helium and isobutane, both operating within a 1.5 T superconducting solenoid magnet. The typical decay vertex resolution for fully reconstructed B decays is approximately 65 μm along the centre-of-mass (CM) boost direction. Photons are detected in an electromagnetic calorimeter (EMC) consisting of 6580 CsI(Tl) crystals arranged in barrel and forward endcap subdetectors. The iron flux return (IFR) is segmented and instrumented with multiple layers of resistive plate chambers for the identification of muons and long-lived neutral hadrons. A crucial part of the $B \to \pi K$ analysis is the identification of charged kaons and pions. The Cherenkov angle, θ_c, of kaons and pions is measured by a Detector of Internally Reflected Cherenkov light (DIRC). The DIRC relies on total internal reflection of photons, produced from charged tracks traversing quartz bars, to deliver Cherenkov light outside the tracking and magnetic volumes [43]. The typical separation between kaons and pions varies from 8σ at 2 GeV/c to 2.5σ at 4 GeV/c, where σ is the average resolution on θ_c.

This section describes briefly all the subsystems of the BaBar detector. A more detailed description can be found in [43].

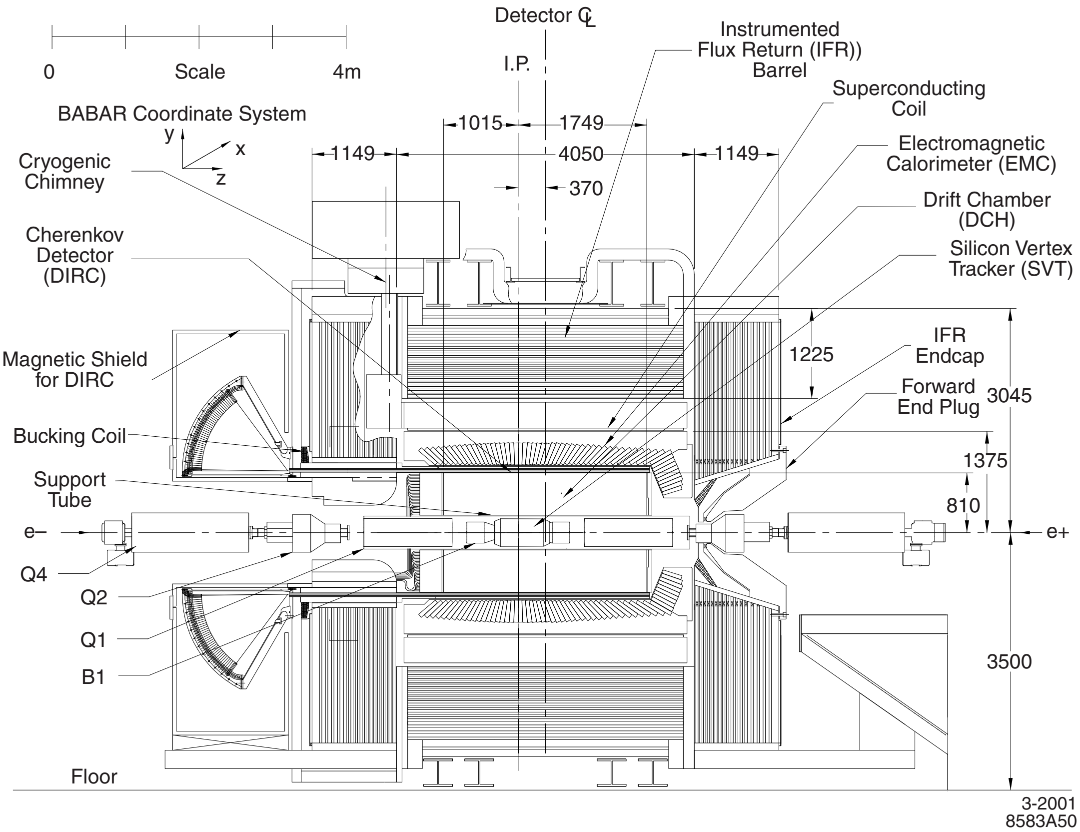

Figure 2.3: *A side view of the BaBar Detector.*

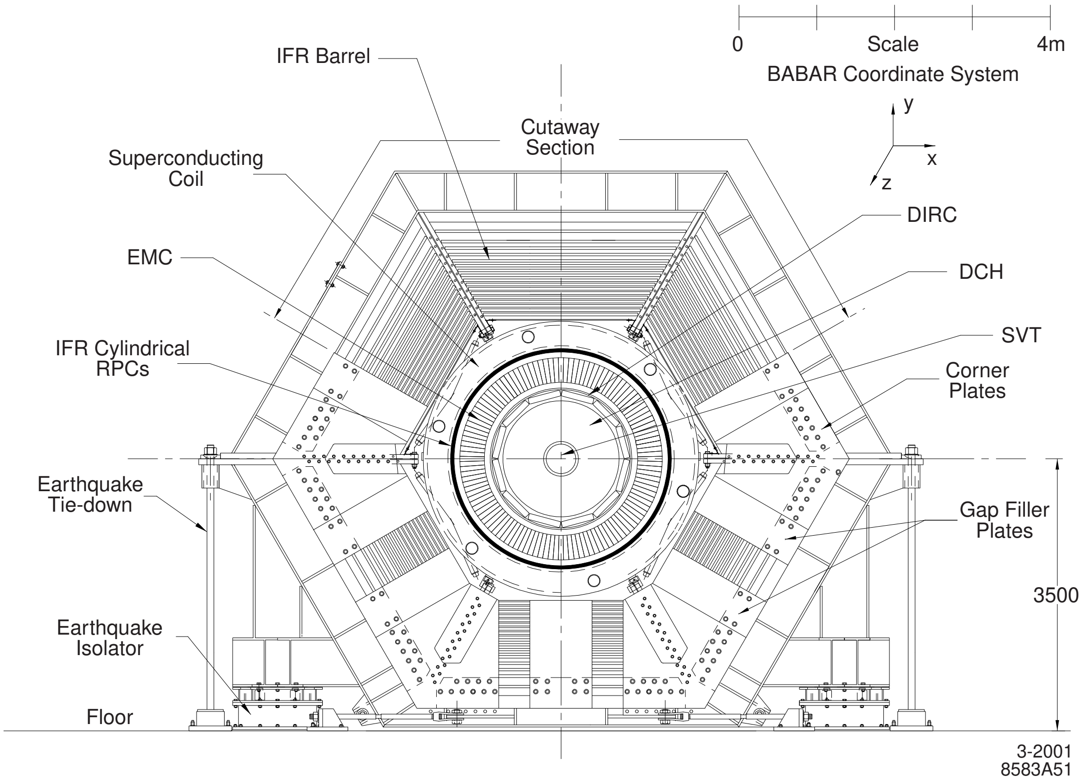

Figure 2.4: *A cross-sectional view of the BaBar Detector.*

2.3 The Silicon Vertex Tracker (SVT)

2.3.1 Physics Requirements

The main purpose of the Silicon Vertex Tracker is to measure time-dependent CP asymmetries by precisely reconstructing the separation of B^0 decay vertices. The mean spatial resolution on the separation of each B^0 decay vertex along the z-axis is 80 μm. The SVT provides tracking information in addition to the drift chamber and is the only tracking detector for particles with $p_T < 100$ MeV/c. Such low momentum tracks, like slow pions from D^* decays, are mostly contained within the SVT volume. The silicon vertex tracker must also be efficient for particles such as K_S^0, which predominantly decays to two charged pions ($K_S^0 \rightarrow \pi^+\pi^-$) and appears in the CP 'Golden Channel' $B^0 \rightarrow J/\psi K_S^0$ and in the context of this thesis, $B^0 \rightarrow \pi^0 K_S^0$, $B^\pm \rightarrow \pi^\pm K_S^0$.

2.3.2 PEP-II Constraints

The design of the SVT is affected by the needs of BaBar and its proximity to the PEP-II interaction region. The SVT is located within the volume of the long PEP-II support tube, which extends all the way through the detector; therefore, there is a limited amount of space. The accelerator B1 bending magnets limit the maximum acceptance in the forward region to 350 mrad in polar angle from the beamline and 400 mrad in the backward direction. The SVT is exposed to $\approx$ 240 krad/yr of ionising radiation in the horizontal plane directly outside the beam pipe and must withstand a total of 2 Mrad during the experiment's ten year lifetime. A radiation monitoring system capable of aborting the beams is required to protect the silicon. The SVT must be cooled and it must operate within the detector's 1.5 T magnetic field. The SVT is made of five layers of double-sided silicon-strip detectors. The arrangment of these layers can be seen in figure 2.5. The inner three layers have spatial resolution for perpendicular tracks of 10-15 μm and about 40 μm in the outer two layers. The inner three layers perform impact parameter measurements, while the outer layers are necessary for pattern recognition and low p_T tracking.

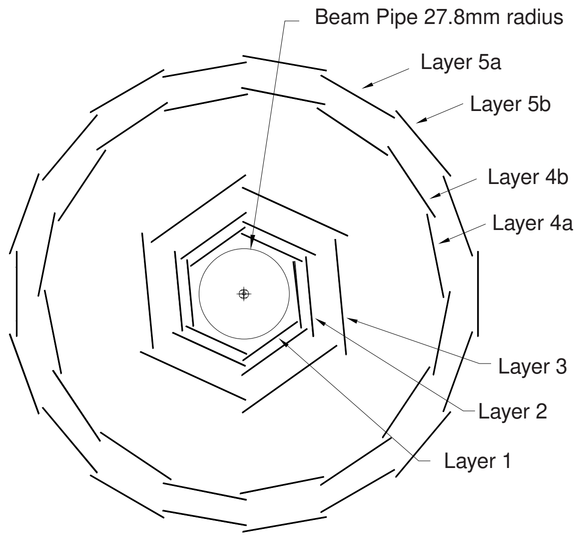

Figure 2.5: *The BaBar Silicon Vertex Tracker: A cross sectional view of the SVT in the rφ plane looking down the beam pipe.*

2.3.3 Mechanical Design

The SVT is mounted inside a carbon fibre support tube of radius 20 cm. The five layers of double-sided silicon strip sensors are concentric around the beam pipe and are divided into modules. Five layers provide five position measurements in ϕ and z for each particle traversing the SVT. The inner three layers have six detector modules which are straight, while the two outer modules have sixteen and eighteen detector modules, respectively (see figure 2.6). The design minimises the amount of silicon required to cover the solid angle and also prevents tracks from having large angles of incidence, which would increase measurement errors. Each module consists of six silicon wafers glued to carbon fibre beams. The inner sides of the modules have strips perpendicular to the beamline and measure the z coordinate (z-side), while the outer sides have strips parallel to the beamline and make the ϕ measurement, (ϕ side). In total, the SVT has 340 silicon detectors, covering a surface area of 0.94 m^2.

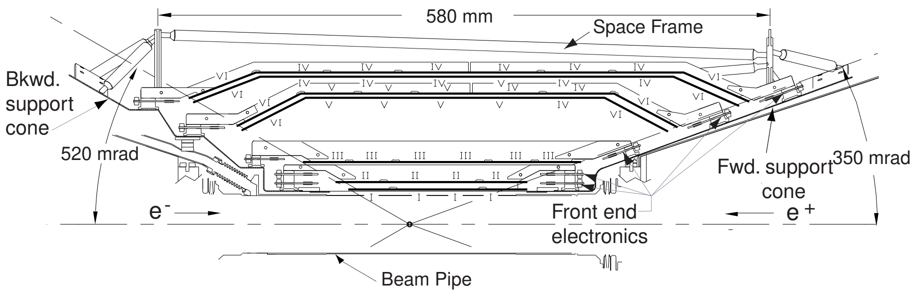

Figure 2.6: *The BaBar Silicon Vertex Tracker: A cross sectional view of the SVT in the yz plane. The IP is marked at the centre.*

2.3.4 Readout

The modules are electrically divided into two half-modules, which are read out at the ends. There are approximately 150 000 readout channels. The signals from the strips are shaped and amplified and then compared to a threshhold, determined by background conditions during running. This 'time-over threshold' method varies approximately logarithmically with induced charge. Digitisation is performed as part of the front end electronics. The digitised signal is passed to a circular buffer, which is read out when a Level 1 trigger accept signal is received.

2.3.5 Reconstruction

SVT clusters are formed by grouping adjacent strips with consistent times. Clusters separated by just one strip are merged into one cluster. The two original clusters plus the merged cluster are passed to a pattern recognition algorithm, which selects the best interpretation. Hit position is expressed in terms of the physical position of the silicon sensors.

2.3.6 Performance

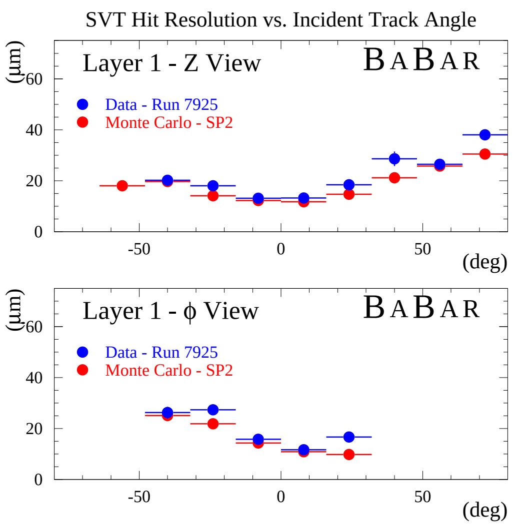

Figure 2.7: *The BaBar Silicon Vertex Tracker: Performance plot showing the position resolution in z (top plot) and ϕ (bottom plot) for the 1st layer. A z resolution of between 15-40 μm is obtained.*

A comparison between data and Monte Carlo (MC) for the first SVT layer resolution as a function of the incident track angle is shown in figure 2.7. The top plot shows the resolution for the first z layer and the bottom one for the first ϕ layer. A resolution of between 15 μm to 40 μm can thus be obtained in the first z layer and between 10 μm to 30 μm in ϕ.

2.4 The Drift Chamber (DCH)

2.4.1 Physics Requirements

The Drift Chamber is the principal charged particle tracking system of the BaBar detector, providing a precision measurement of transverse momentum (p_T) from the curvature of charged particle trajectories in the 1.5 T field. To reconstruct exclusive final states from B^0 decays, with minimal background, the DCH must reconstruct tracks with $0.1 < p_T < 5$ GeV/c. Excellent spatial resolution is required for accurate momentum measurements, matching tracks to those in the SVT and facilitating the identification of charged particles entering the DIRC and EMC. The DCH also measures ionisation loss (dE/dx) for low momenta particles (below 700 MeV/c) and supplies single cell hit information to the Level 1 trigger.

2.4.2 Mechanical Design

The DCH is a 280 cm long cylinder, with an inner radius of 23.6 cm and outer radius of 80.9 cm. The DCH is mounted from the rear endplate to the Cherenkov light detector (DIRC) central support tube, within the volume inside the DIRC and outside the PEP-II support tube. The centre of the tube is displaced forward by 36.7 cm to accommodate the asymmetric boost of the $\Upsilon(4S)$ events. To minimise the material between the SVT and the DCH, the inner cylinder is made from 1 mm thick beryllium. The outer cylinder is constructed from two carbon fibre layers on a Nomex core. The endplates are made from thin aluminium; 12 mm in the forward endplate, 24 mm in the rear. The forward endplate is thinner to reduce the material in front of the calorimeter. 20 μm diameter gold plated tungsten-rhenium sense wires are stretched between the endplates along the length of the DCH cylinder. A nominal voltage of +1960 V is applied to the sense wires. The chamber voltage was lowered to 1900 V for part of the run, due to concern about a small region of the chamber that was damaged during the commissioning phase. Each sense wire is surrounded by an hexagonal field cage composed of two field wires and one guard wire, see figure 2.8. The field and guard wires are 120 μm and 80 μm diameter gold-plated aluminium, respectively, held at 350 V. Therefore, the drift system consists of 7104 hexagonal cells, approximately 1.8 cm wide by 1.2 cm high, arranged in 40

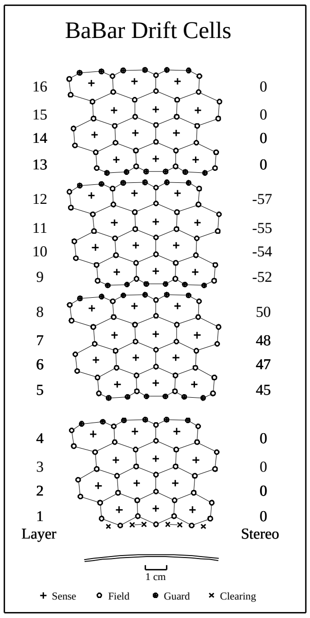

Figure 2.8: *The BaBar Drift Chamber: drift cells.*

concentric layers between a radius of 25.3 and 79.0 cm. The forty layers are grouped into ten superlayers of four layers each. The superlayer structure facilitates fast local segment finding as the first step in pattern recognition, particularly important in Level 1 trigger decisions. Superlayers are alternate in orientation: first axial (A), then a small positive stereo angle (U), followed by a small negative stereo angle (V) (figure 2.9). The gas is an 80:20 mixture of He:Isobutane.

2.4.3 Readout

The DCH electronic system provides a measurement of the drift time and the integrated charge. The HV distribution boards and readout electronics are located on the rear endplate to keep the additional material out of the fiducial volume of the detector. Drift time is extracted from the leading edge of the amplified signal produced from drifting electrons arriving at the sense wire, using a TDC. The total charge deposited in a cell is measured using a 15 MHz flash ADC. Data readout is via only four optical fibre links to ROM's in the electronics house.

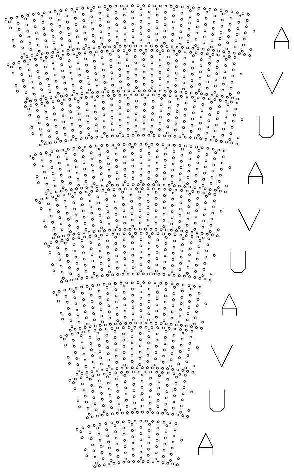

Figure 2.9: *The BaBar Drift Chamber: The Axial (A) and Stereo (U,V) superlayers containing the hexagonal drift cells.*

2.4.4 Reconstruction

Charged tracks are defined by five parameters (d_0, ϕ_0, ω, z_0 and $\tan\lambda$), which are measured at the point of closest approach to the z axis; d_0 and z_0 are the distances of this point from the origin of the coordinate system in the $x-y$ plane and along the z axis, respectively. ϕ_0 is the azimuthal angle of the track, λ is the dip angle relative to the transverse plane and $\omega = 1/p_T$ is its curvature. The signs of d_0 and ω depend on the charge of the track. The track finding and fitting procedures make use of a Kalman filter algorithm [45].

2.4.5 Performance

The track reconstruction efficiency for the DCH has been measured as a function of transverse momentum p_T, polar (θ), and azimuthal angles (ϕ) in multi-track events. The efficiency is determined as the ratio of reconstructed DCH tracks to the number of tracks detected in the SVT. Figure 2.10 shows the efficiency as a function of p_T for the two voltage settings. At the design voltage of 1960 V, the efficiency is $(98 \pm 1)\%$ per track of more than 200 MeV/c. At 1900 V, the efficiency is reduced by about 5%. Cosmic rays provide a simple method of measuring track resolution. The upper and lower halves of cosmic ray tracks traversing the DCH and SVT are fitted as two separate tracks and the resolution is taken as the difference of the

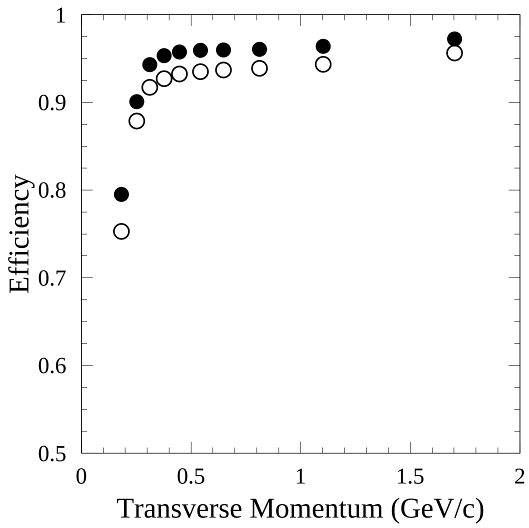

Figure 2.10: *The BaBar Drift Chamber: The track reconstruction efficiency in the DCH at operating voltages of 1900 V (open circles) and 1960 V (closed circles) as a function of transverse momentum.*

measured parameters for the two track halves. The dependence of the resolution on the transverse momentum is shown in figure 2.11. The measured $\mathrm{d}E/\mathrm{d}x$ for various track species as a function of track momenta are given in figure 2.12. The curves show the Bethe-Bloch predictions derived from selected control samples of particles of different masses.

2.5 Detector for Internally Reflected Cherenkov light (DIRC)

2.5.1 Physics Requirements

The need to distinguish between high momenta kaons and pions up to 4 GeV/c necessitates a dedicated charged particle identification system. The novel DIRC (Detection of Internally Reflected Cherenkov light) [43], figure 2.13, satisfies the demands of π/K separation to tag B^0 flavour and discriminate rare two-body decays, such as $B^0 \to \pi^{\mp}\pi^{\pm}$ and $B^0 \to \pi^{\pm}K^{\mp}$, the subject of this thesis. The DIRC also provides muon identification below 750 MeV/c, where the IFR is inefficient, and proton identification with momenta above 1.3 GeV/c.

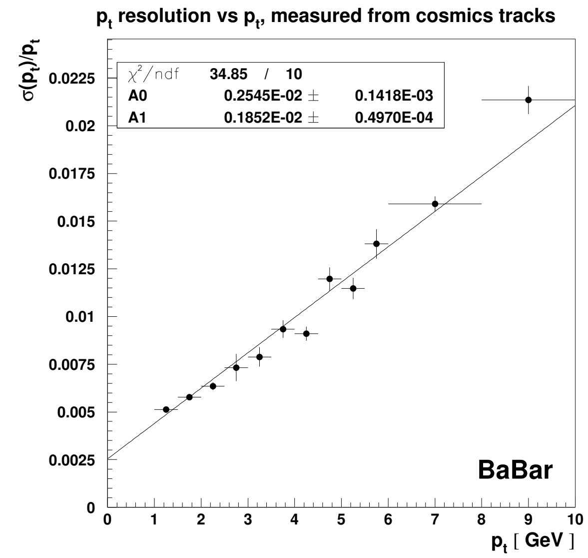

Figure 2.11: *The BaBar Drift Chamber: The track resolution as a function of transverse momentum, p_T.*

2.5.2 Mechanical Design

A charged particle, velocity $v = c\beta$, where c is the velocity of light in a vacuum, exiting the barrel section of the DCH traverses an array of synthetic quartz bars with refractive index n (~ 1.473) and, if $\beta > 1/n$, generates a cone of Cherenkov photons (half angle θ_c) with respect to the particle direction, where $\cos\theta_c = 1/\beta n$. The bars act as waveguides to photons within the total internal reflection limit, directing them towards an array of 10,752 photomultiplier tubes (PMT's) located in the backward direction, outside the fiducial volume of the detector, in a region of low magnetic field. A mirror is located at the forward end, perpendicular to the bar axis, to reflect forward going photons back towards the rear instrumented end. Figure 2.14 is a schematic showing how light is directed towards the PMT's. The DIRC bars are arranged in a 12-sided polygonal barrel between the drift chamber and the calorimeter, occupying a radial space of 8 cm. The polar angle coverage is -0.84 $< \cos\theta_{Lab} <$ 0.90. The bars are grouped in 12 hermetically sealed units (bar boxes) made of thin aluminium-hexal panels. Each bar box contains 12 long bars placed side by side, giving a total of 144 long bars. The bars are 1.7 cm thick, 3.5 cm wide and 4.9 m long. Each long bar is assembled from four 1.225 m 'short' bars, glued end-to-end. Cherenkov photons exit the bar through a wedge and quartz

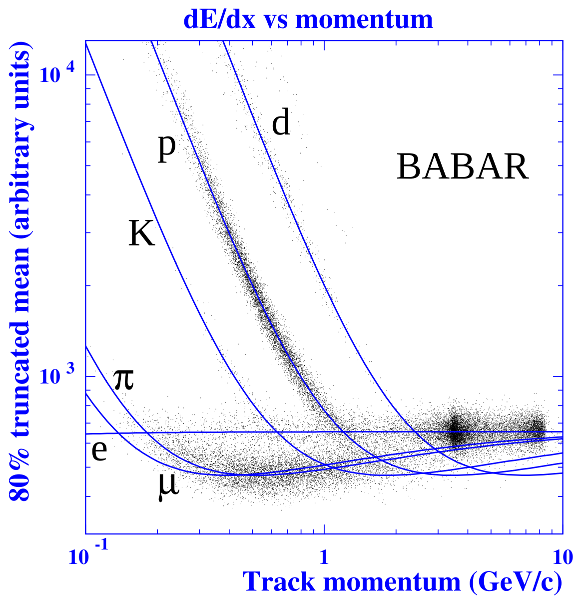

Figure 2.12: *The BaBar Drift Chamber: Measurement of* dE/dx *in the DCH as a function of track momenta. The curves show the Bethe-Bloch predictions for electrons, muons, pions, kaons, protons and deuterium as a function of the track momentum.*

window into a water filled expansion region, called the standoff box (SOB). The stainless steel SOB consists of a cone, cylinder and 12 sectors of PMT's, on the surface of a half torus, with major radius 3 m and minor radius 1.2 m. The SOB is filled with 6000 litres of purified water. The Cherenkov angle, θ_c, is deduced from the location of the PMT observing a Cherenkov photon and the position and angles of a charged track, known from the BaBar tracking system. An additional observable is the time a PMT hit occurs, measured to a precision of 1.7 ns. For a given momentum, particles of different mass produce different Cherenkov angles.

2.5.3 Readout

The DIRC front-end electronics is designed to measure the arrival of each Cherenkov photon. The 168 DIRC Front-end Boards (DFB) are located outside the SOB and each processes 64 PMT inputs. The boards are highly integrated and have 8 analogue chips, 4 TDC chips and one 8-bit flash ADC. The PMT signals are amplified and pulse shaped. The TDC chip contains a 16-channel TDC. To cope with the L1 maximum trigger latency of 12 μs, the selective readout process extracts data in time with the trigger within a programmable time window between 64 ns and 2 μs

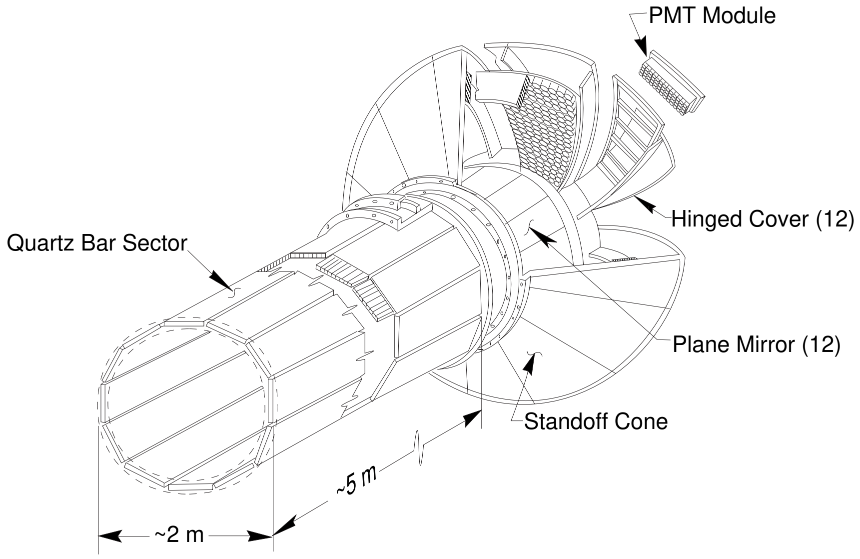

Figure 2.13: *The BaBar DIRC: A schematic of the DIRC, depicting the quartz radiators and the stand off box.*

and is typically set at 600 ns. The six readout modules (ROM's) are connected by 1.2 Gbytes/s optical fibres to twelve DIRC crate controllers which form the interface to the DIRC VME front-end crates.

2.5.4 Reconstruction

The emission angle and arrival time (figure 2.15) of Cherenkov photons are reconstructed from the space-time coordinates of the PMT hits. A timing measurement is also part of the PMT reconstruction. The timing resolution is used to suppress beam induced background and exclude other tracks in the same event as the source of the photon. A likelihood value for each of the five stable particle species is assigned to a track passing through the DIRC, while track hypotheses are tested. If enough photons are found, a fit is made.

2.5.5 Performance

The DIRC has been extremely successful. The Cherenkov angle and π/K separation are shown in figure 2.16 and as a function of momentum for tracks from a D^0 control sample. A separation of around 3σ is possible for the highest momentum kaons and pions. Figure 2.17 shows the invariant π/K inclusive mass spectrum of this D^0

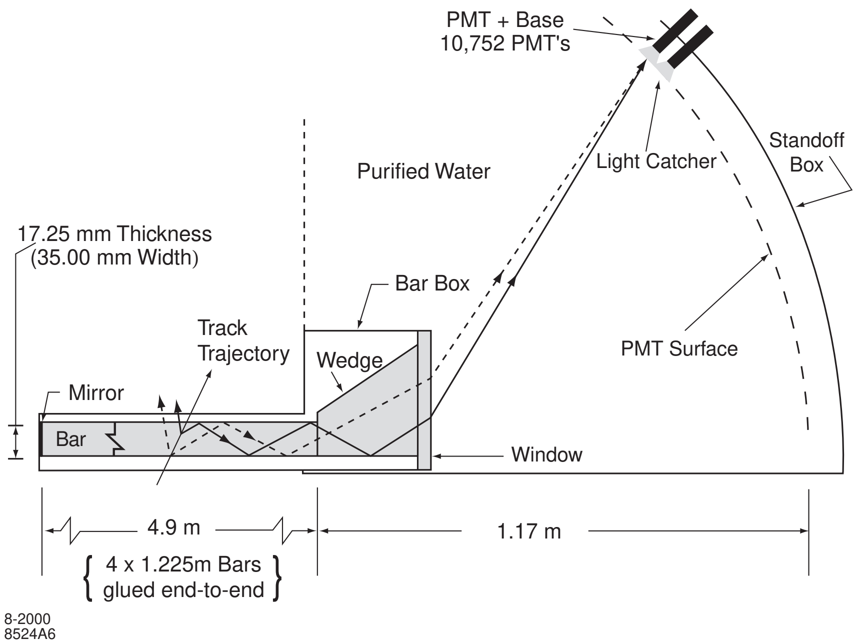

Figure 2.14: *The BaBar DIRC: The Cherenkov radiation produced by charged particles traversing the quartz are total internally reflected to the detector surface. In doing this, the production angle of the radiation is preserved.*

control sample, with and without the use of the DIRC for kaon identification. The mass peak corresponds to the decay of the D^0 particle. This plot clearly shows that the DIRC dramatically reduces the background.

2.6 The Electromagnetic Calorimeter (EMC)

2.6.1 Physics Requirements

The BaBar EMC is designed to measure precisely and efficiently the energies of electromagnetically interacting particles through the initiation of electromagnetic showers in a scintillating crystal material, over an energy range 20 MeV to 9 GeV. This allows the detection of photons from π^0 and η decays as well from electromagnetic and radiative processes. The reconstruction of extremely rare B meson decays containing π^0 (eg. $B^0 \to \pi^0\ \pi^0$) requires high resolution calorimetry, with a resolution of $\mathcal{O}(1\%)$. Below 2 GeV, the π^0 mass resolution is dominated by the energy resolution. At higher energies, the angular resolution dominates and is a few mrads. Electron identification in the EMC also contributes to the tagging of neutral B mesons.

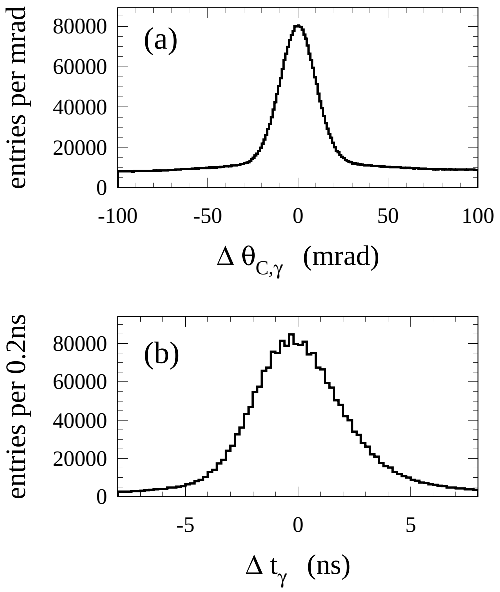

Figure 2.15: *The BaBar DIRC: The difference between (a) measured and expected Cherenkov angle for single photons, $\Delta\theta_{c\gamma}$, and (b) measured and expected photon arrival time, for single muons in $\mu^+\mu^-$ events.*

2.6.2 Mechanical Design

Thallium-doped Ceasium Iodide (CsI(Tl)) has been chosen as the crystal material due to its high light yield. A radiation length of $X_0 = 1.86$ cm accommodates complete shower containment with a compact design (see table 2.2). There are a total of 6580 crystals in the barrel and forward endcap, arranged in a quasi-projective geometry, giving a solid angle coverage of $-0.775 < \cos\theta_{Lab} < 0.962$ corresponding to $-0.916 < \cos\theta_{CM} < 0.895$. The barrel contains 5760 crystals divided into 48 rings along its 2.8 m length; each ring of inner radius 0.9 m consists of 120 crystals. The endcap is contiguous with the barrel and has 820 crystals divided into 8 rings. The outer three rings each have 120 crystals, the next three each have 100 and the inner two rings both have 80 crystals, with inner radius 0.5 m. The crystals have a tapered trapezoidal cross-section and vary in length from 16 X_0 in the backward end to 17.5 X_0 in the forward direction to compensate for the effects of shower leakage due to the increasing particle energy. Light is both totally internally reflected and transmitted at the crystal surface; to recover lost light the crystals are wrapped in a dispersive white reflector (165 μm Tyvek 1056D) and 25 μm aluminium foil

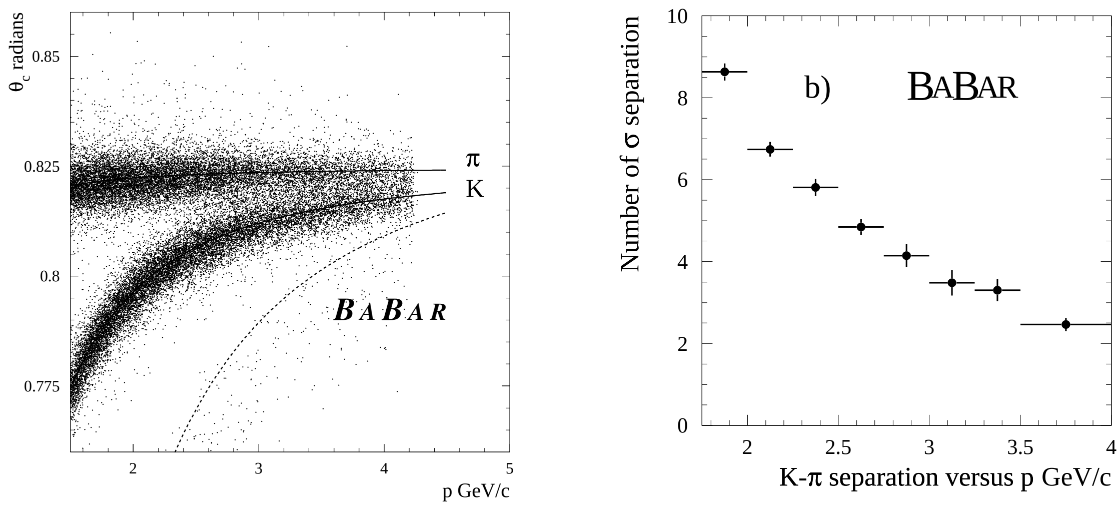

Figure 2.16: *The BaBar DIRC: The DIRC π/K separation, in terms of Cherenkov angle, θ_C, plotted against the track momentum.*

to provide RF shielding. The aluminium is further wrapped in 40 μm Mylar to electrically isolate it from the carbon fibre support structure of thickness 300 μm. This gives a total gap of 1.25 mm between crystals.

Properties	CsI(Tl)
Radiation Length (cm)	1.85
Moliere Radius (cm)	3.6
Absorption Length for 5GeV pions (cm)	41.7
Density (g/cm^3)	4.53
$dE/dx\|\|_{mip}$ (MeV/cm)	5.6
Light Yield (photons/ MeV $\times 10^3$)	40-50
Light Yield Temperature Coefficient ($\%/^\circ C$)	0.1
Peak Emission (nm)	565
Refractive Index at Emission Maximum	1.79
Decay Time (ns)	940
Radiation Hardness (rad)	$10^3 - 10^4$

Table 2.2: Properties of Thallium doped Caesium Iodide CsI(Tl), used by the BaBar EMC.

2.6.3 Readout

The crystals are read out with two independent low noise silicon PIN diodes epoxied to their rear faces. The photodiode ouput is sent through a preamplification

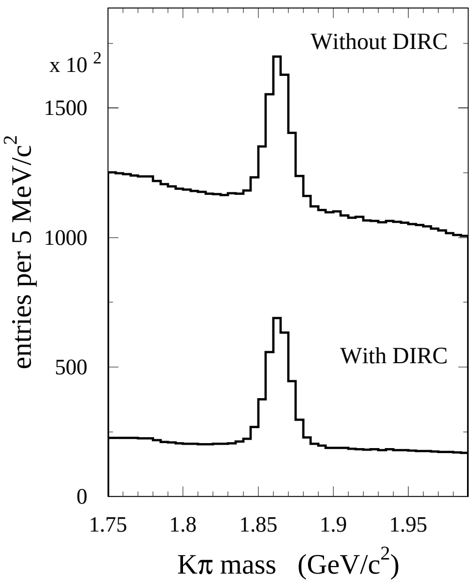

Figure 2.17: *The BaBar DIRC: The $K\pi$ reconstructed mass with and without DIRC. The DIRC clearly reduces the combinatoric background dramatically*

circuit, positioned directly behind the photodiodes. The preamplifier is a low-noise charge-sensitive amplifier implemented as a custom application specific integrated circuit (ASIC). Shielded ribbon cables carry analog signals to the end flanges of the barrel and the back plate of the endcap where the amplification/digitisation electronics (ADB) reside. The two preamplifiers on each crystal each provide amplification factors of 1 and 32 and thus reduce the dynamic range of the signal that is transmitted to the mini-crates to 13 bits. A custom auto-ranging encoding (CARE) circuit further amplifies the signal to arrive at a total gain of 256, 32, 4 or 1 for four energy ranges, 0-50 MeV, 50-400 MeV, 0.4-3.2 GeV and 3.2-13.0 GeV, respectively. The appropriate range is identified by a comparator and the signal is digitised by a 10-bit, 3.7 MHz Analogue to Digital Converter (ADC). The ADC signal is sent across a 30 m fibre optic cable to the real-time processor boards (UPC) located in the elctronics house. The UPC boards perform feature extraction and provide the digital sum of crystals for input to the L1 trigger.

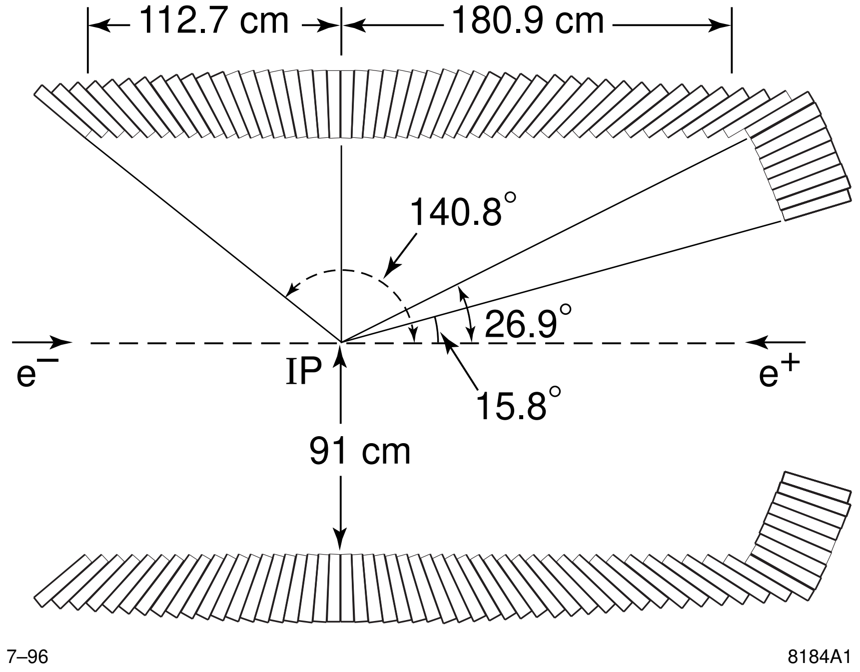

Figure 2.18: *The BaBar Electromagnetic Calorimeter: A side view of the barrel and forward endcap EMC.*

2.6.4 Reconstruction

A particle showering in the calorimeter will typically deposit energy over several crystals. The individual crystals are then grouped into 'clusters', which are further separated into 'bumps'. A 'bump' is a local maximum within a cluster and facilitates resolution of particles which shower close to each other. A correction factor must be applied to the bump energy to account for energy lost through leakage and particles showering in the material in front of the calorimeter. Finally, a track-matching algorithm is applied to determine whether a shower is a charged or neutral candidate.

2.6.5 Performance

The energy resolution of a homogeneous crystal calorimeter can be described empirically in terms of a sum of two terms added in quadrature

$$\frac{\sigma_E}{E} = \frac{a}{\sqrt[4]{E(\,\mathrm{GeV})}} \oplus b, \tag{2.1}$$

where E and σ_E refer to the energy of a photon and its rms error, measured in GeV. The energy dependent term a arises primarily from the fluctuations in photon statistics, but it is also impacted by electronic noise of the photon detector and electronics. The angular resolution is determined by the transverse crystal size and the distance from the interaction point. It can also be empirically parameterized as a sum of an energy dependent and a constant term,

$$\sigma_{\theta=90^0} = \sigma_\phi = \frac{c}{\sqrt{E(\mathrm{~GeV})}} + d, \tag{2.2}$$

where the energy E is measured in GeV. At low energy, the energy resolution of the

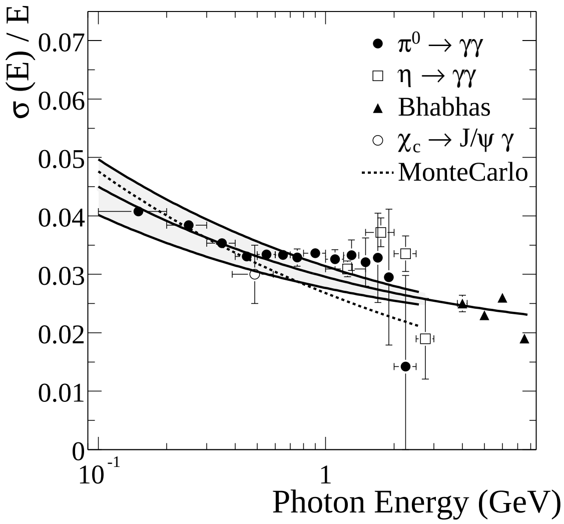

Figure 2.19: *The BaBar Electromagnetic Calorimeter: energy resolution measured for photons and electrons from various processes. The solid curve is a fit to equation 2.1*

EMC is measured directly with the radioactive source yielding $\sigma_E/E = (5.0 \pm 0.8)\%$ at 6.13 MeV. At high energy, the resolution is derived from Bhabha scattering, where the energy of the detected shower can be predicted from the polar angle of the $e^{\pm}$. The measured resolution is $\sigma_E/E = (1.9 \pm 0.1)\%$ at 7.5 GeV. Figure 2.19 shows the energy resolution extracted from a variety of processes as a function of energy. Below 2 GeV, the mass resolution of π^0 and η mesons decaying into two photons of approximately equal energy is used to infer the EMC energy resolution. A fit to the energy dependence results in,

$$\frac{\sigma_E}{E} = \frac{(2.32 \pm 0.30)\%}{\sqrt[4]{E(\mathrm{~GeV})}} \oplus (1.85 \pm 0.12)\%. \tag{2.3}$$

The values of these fitted parameters are higher than the somewhat optimistic earlier estimates [42], but they agree with detailed Monte Carlo simulations which include the contributions from electronic noise and beam background, as well as the impact of the material and the energy thresholds. The measurement of the angular resolu-

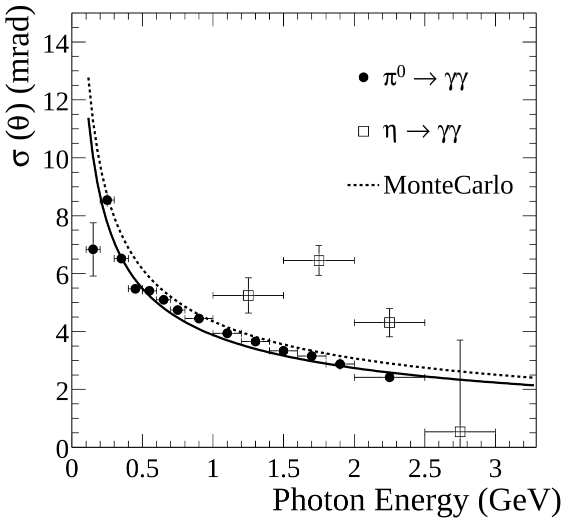

Figure 2.20: *The BaBar Electromagnetic Calorimeter: angular resolution from π^0 and η decays to two photons. The solid curve is a fit to equation 2.2.*

tion is also based on the analysis of π^0 and η decays to two photons of approximately equal energy. The result is presented in Figure 2.20. The resolution varies between about 12 mrad at low energies and 3 mrad at high energies. A fit to the empirical parameterization of the energy dependence results in,

$$\sigma_\theta = \sigma_\phi = \left[\frac{(3.87 \pm\ 0.07)}{\sqrt{E(\,\mathrm{GeV})}} + (0.00 \pm\ 0.04)\right] \mathrm{mrad}. \tag{2.4}$$

These fitted values are slightly better than one would expect from detailed Monte Carlo simulations. The reconstructed π^0 mass is measured to be 135.1 MeV/c^2 and is stable to better than 1% over the full photon energy range (figure 2.21). The width of 6.9 MeV/c^2 agrees well with the prediction obtained from detailed Monte-Carlo simulations.

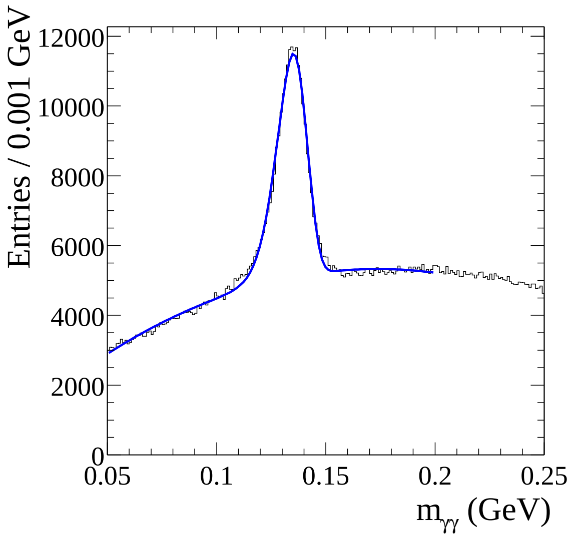

Figure 2.21: *The BaBar Electromagnetic Calorimeter: invariant mass of two photons in $B\overline{B}$ events. The energies of the photons and the π^0 are required to exceed 30* MeV *and 300* MeV *respectively. The solid line is a fit to the data.*

2.7 The Instrumented Flux Return (IFR)

2.7.1 Physics Requirements

The IFR is the outermost detector at BaBar, consisting of a main barrel section and forward and backward endcaps to identify neutral hadrons and muons for tagging. Muons are important in the reconstruction of the J/ψ to study semileptonic decays and rare modes involving leptons. K_L^0 detection allows the measurement of sin2β in the CP decay $B^0 \to J/\psi K_L^0$. The detection of neutral hadrons is also required in the study of charmless decays to reduce backgrounds. A good efficiency in muon identification over a wide momentum range is necessary. In the barrel region, the minimum detectable momentum of particles coming from the interaction region is 450 MeV/c, while in the forward and backward endcaps it is 250 MeV/c. The endcaps provide solid angle coverage down to 300 mrad in the forward direction and 400 mrad in the backward direction. For efficient tagging, a hadron should be misidentified as a muon as seldom as possible. The IFR does not measure the energy of particles, only their direction of flight.

2.7.2 Mechanical Design

The graded segmentation of the iron in the IFR is a novel feature of this subsystem. The iron segmentation has been optimised on the basis of Monte Carlo studies of muon penetration and K_L^0 interaction. The barrel is composed of flat steel plates arranged hexagonally about the beam axis and is 4.05 m in length, with an inner radius of 1.78 m and outer radius of 3.01 m, see figure 2.22. The endcaps are hexagonal vertical steel plates, divided into two parts, allowing detector access. There is a gap of 15 cm between the endcaps and the barrel, causing a loss in solid angle of 7 %. There are 18 plates contained in the barrel (total thickness 65 cm) and the endcaps (60 cm). Both the barrel and endcaps have nine inner plates each 2 cm thick, four middle plates each 3 cm thick and 3 outer plates each 5 cm thick. The two outermost plates are 10 cm in the barrel and 10 cm and 5 cm in the endcaps. The active detectors are Resistive Plate Chambers (RPC), figure 2.23, and

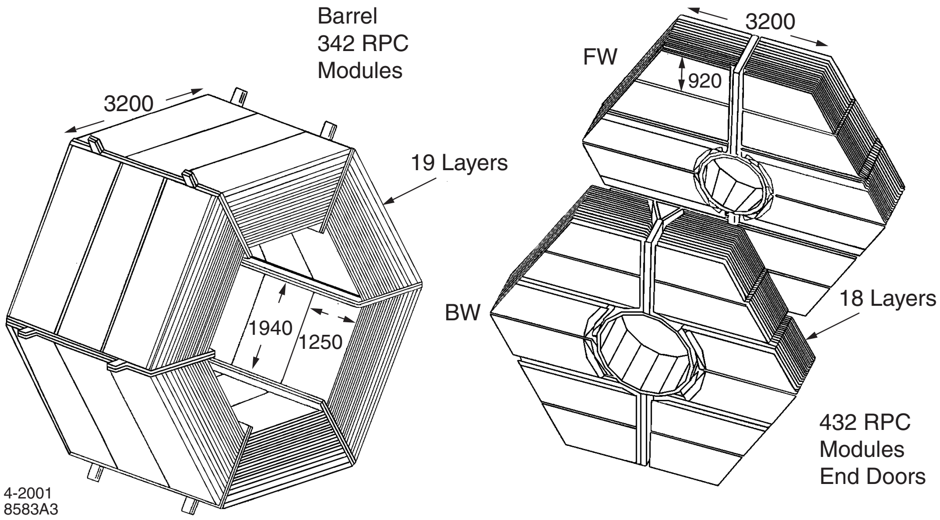

Figure 2.22: *The BaBar Instrumented Flux Return: Barrel and Endcaps*

are located in the gaps (3.2 cm wide) between the steel plates. Planar RPC's consist of two bakelite (phenolic polymer) electrode plates, each 2 mm thick, separated by 2 mm. The space between the plates is filled with an argon based gas. The potential difference between the electrodes is approximately 8 kV. There is a double layer of curved RPC's placed between the outer radius of the CsI calorimeter and the inner radius of the superconducting solenoid, to provide information on particles which lose most of their momentum in the EMC. The RPC modules are 1.25 m wide and vary in length from 1.81 m to 3.2 m.

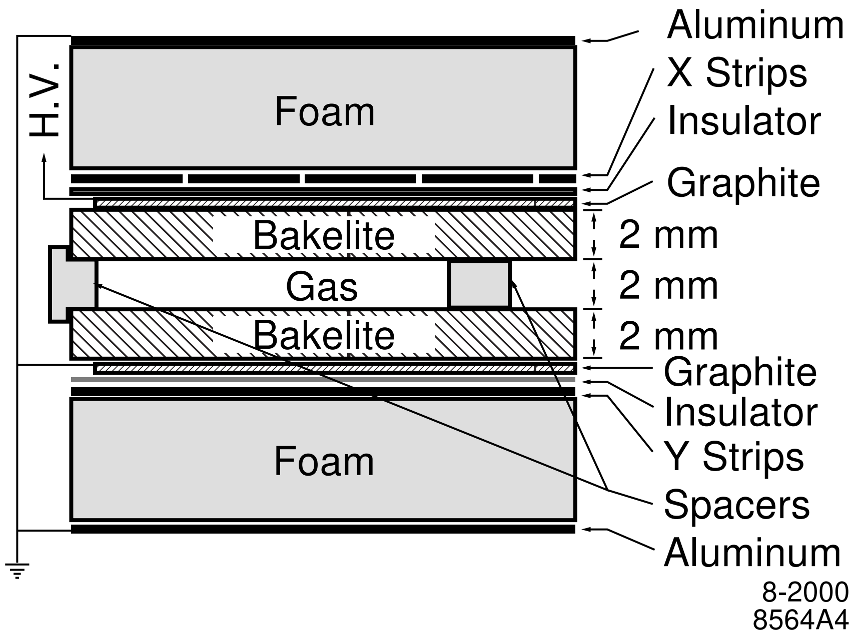

Figure 2.23: *The BaBar Instrumented Flux Return: Design of the Resistive Plate Counters (RPCs) used by the IFR*

2.7.3 Readout

A charged particle passing through the IFR loses energy via ionisation, producing a spark as it traverses each RPC. The electrical discharge is picked up by aluminium strips present on both sides of the RPC chamber. The strips on one side are orthogonal to those on the other side of the chamber, so that three-dimensional positional information can be extracted. Data from sixteen strips is passed to a Front End readout Card (FEC), which then passes the active strips to a TDC circuit. The TDC output is stored in buffers, which allow for the trigger latency before being passed along an optical fibre link to the BaBar DAQ system.

2.7.4 Reconstruction

Charged tracks reconstructed in the DCH are extrapolated to the IFR. The predicted average position of intersections with the RPC's are computed. Hits found within a specific distance from the predicted intersection are associated with a charged track. A number of variables are used to distinguish μ/π. μ candidates are required to meet the criteria for minimum ionising particles in the EMC. K_L^0 and other neutral hadrons are identified as clusters that are not associated with a charged track.

2.7.5 Performance

As shown in figure 2.24 a muon efficiency of close to 90 % has been achieved in the momentum range $1.5 < p < 3.0$ GeV/c with a fake rate for pions of about 6 - 8%. The K_L^0 detection efficiency has been found to vary between 20 - 40 % in the $1.0 < p < 4.0$ GeV/c momentum range. During the first months of running it was found that the RPC dark current was very temperature dependent, and a 14 - 20 % current increase was observed per °C. Each FEC dissipates 3 W, adding up to a total power of 3.3 kW in the barrel and 1.3 kW in the forward end door. Temperatures in the IR hall often exceeded 31 °C and the temperature inside the steel rose to more than 37 °C. The dark currents in many modules exceeded the capabilities of the HV system and and some RPC's had to be temporarily disconnected. Water cooling was installed on the barrel and the end door steel, removing $\approx$ 10 kW of heat and stabilising the temperature to 20 - 21 °C in the barrel. During the operation at high temperatures more than 50 % of the RPC's showed a reduction in efficiency. After cooling was installed and the RPC's were reconnected, some of them continued to deteriorate while others remained stable, with about 30 % at full efficiency.

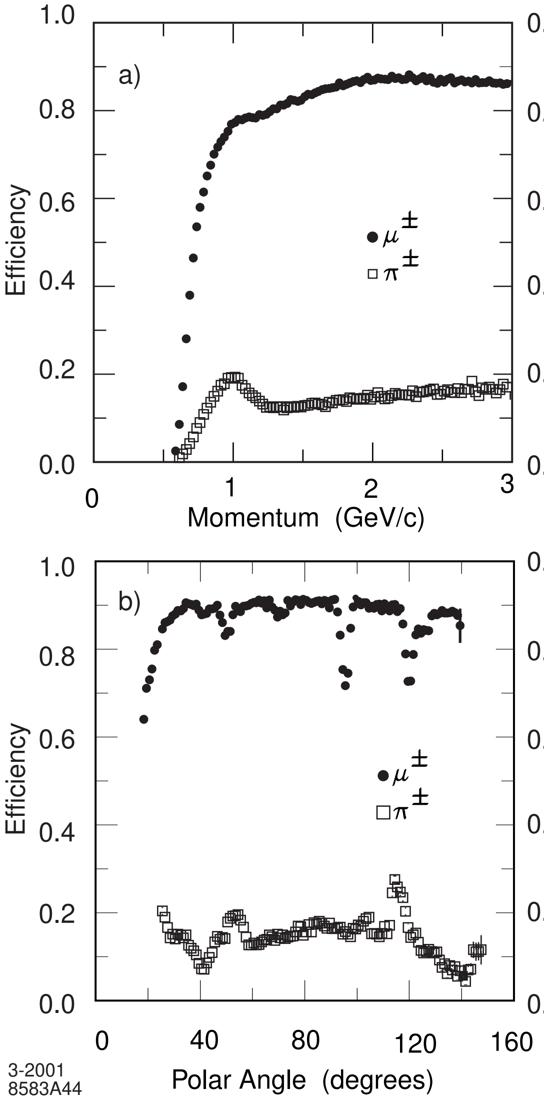

Figure 2.24: *Muon Efficiency (left scale) and pion misidentification probability (right scale) as a function of a) track momentum in the lab and b) the polar angle in momentum range* $1.5 < p < 3.0$ GeV/c.

2.8 The Superconducting Magnet

The BaBar magnet system consists of a superconducting solenoid, a segmented flux return and a field-compensating or bucking coil. This system provides the magnetic field which enables charged particle momentum measurement, serves as the hadron absorber for hadron/muon separation and provides the overall structure and support for the detector components. The solenoid has a magnetic field of 1.5 T. This value gives the desired momentum resolution for charged particles.

2.9 The Trigger

2.9.1 Design Requirements

The BaBar trigger system involves a Level 1 hardware trigger and a Level 3 software trigger. The trigger system must select physics events with a high efficiency, while keeping the output rate below 100 Hz. The Level 1 should be as 'open' as possible to physics events and act solely to reduce the background. The Level 3 trigger then selects the events of most interest. High statistics are vital in the study of CP channels, therefore the efficiency for $b\overline{b}$ events must be at least 99% and at least 95% for $q\overline{q}$ events, which are needed for background subtraction. The high rate of Bhabha events, used in the luminosity determination, requires that only the error on the efficiency need be known to 0.5%. The Level 1 trigger decision is issued with a latency of 11-12 μs after the corresponding beam crossing to initiate the Data Aquisition system (DAQ). In practise, hadronic events have a smaller latency range of $\pm$ 150 ns. Samples of events failing the trigger conditions and events from random beam crossings are also accepted for diagnostic and background studies.

2.9.2 Level 1

The Level 1 trigger system comprises the Drift Chamber Track trigger (DCT), the Calorimeter trigger (EMT), the IFR muon trigger (IFT) and the Global trigger (GLT). The DCT and EMT output basic data objects, called primitives, to the GLT. These are ϕ maps of tracks or energy deposits. The IFT primitive is a three-bit pattern representing hit topologies of muon candidates in the IFR. The GLT then combines primitives into 24 trigger output lines. Typical triggers require at least two tracks in the DCH, one with $p_T > 0.18$ GeV/c and one with $p_T > 0.12$ GeV/c or at least three clusters in the EMC with $E > 100$ MeV, so as to be maximally efficient for minimum ionising particles. These two independent triggers allow good cross-calibrations of efficiencies to be made. $b\bar{b}$ events are triggered at $> 99\%$ efficiency from either the DCT or EMT information and the combined efficiency is 99.9%. The total Level 1 trigger rate for a typical run with HER (LER) currents at 700 mA (1100 mA) and a luminosity of $3.0{\times}10^{33}$ cm^{-2}s^{-1} is approximately 700 Hz. The combined trigger/DAQ rate has a design rate of 2 kHz. This avoids significant deadtime and accommodates the anticipated increase in luminosity.

2.9.3 Level 3

The Level 3 trigger must tag physics processes for permanent storage with a rate of 100 Hz at the design luminosity of $3.0{\times}10^{33}$ cm^{-2}s^{-1}. In order to do this Level 3 must reject background events from beam-induced scattering, cosmic rays and two photon events of no physics interest. The Level 3 trigger is embedded into the Online Event Processing (OEP) framework running in parallel on 32 event filter farm nodes. Track and cluster objects are passed to a set of filter algorithms. The Level 3 DCH and EMC algorithms, independently, perform fast look-up table based track finding and 3-dimensional track fitting, efficient for tracks with $p_T > 250$ MeV/c and clustering for clusters with $E > 30$ MeV to reduce noise. The Level 3 logging decision is based on generic track/cluster topologies rather than on the identification of specific physics processes. However, Bhabha events must be vetoed to reduce their rate. The physics trigger is a logical OR of two orthogonal filters. The track filter requires either one track with $p_T > 800$ MeV/c coming from the interaction point, or two tracks with $p_T > 250$ MeV/c and slightly looser vertex cuts. The cluster filter accepts events with high multiplicity or large total energy and a high invariant (pseudo) mass.

2.10 Data Acquisition (DAQ) and Online System

The detector-mounted front end electronics are connected via 1 Gbytes/s optical fibre links to standard Readout Modules (ROM's), located in the electronics hut.

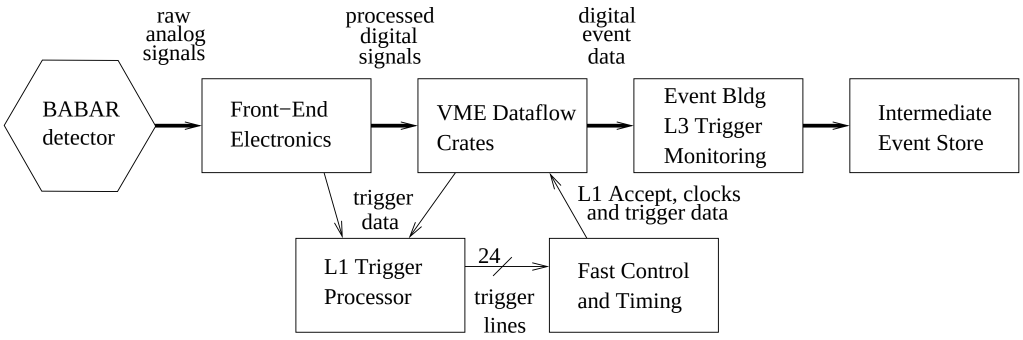

Figure 2.25: *The BaBar ODF : A schematic of the ODF system.*

Each ROM is composed of a single board computer, running VxWorks, linked to three custom boards, one of which is the 'Personality Card'. The EMC uses an 'Untriggered Personality Card (UPC)', which means the ROM's continuously collect data from up to three input data fibres, separating out in software the data corresponding to Level 1 triggers. All other detector subsystems use a 'Triggered Personality Card' (TPC), which requests and collects event data directly from the front end electronics upon receipt of a Level 1 trigger. ROM's are arranged into crates in groups of two to eleven, including a Master ROM. The Master builds partial events from the data acquired from other ROM's in the crates. These data fragments are sent via 100 Mbytes/s switched Ethernet to the nodes of the Online Event Processing (OEP) farm. The OEP farm nodes apply the Level 3 trigger algorithms. Events passing the Level 3 selection are sent via TCP/IP to a single server process which logs them to disk files. Data quality monitoring results are collected from all nodes and compared with defined references by shifters. The online computing system also includes 'The Detector Control' system, which monitors and controls the detector's environmental systems, *i.e.* temperature, high voltage power, gas supplies and PEP-II conditions. Also, the 'Run Control' system coordinates the action of the online and DAQ components.

2.11 Online Prompt Reconstruction (OPR)

After data aquisition, Online Prompt Reconstruction (OPR) is performed by a farm of about 150 Unix processors. All colliding beam events are filtered and tagged.

Interesting events are completely reconstructed and written to the object database. 'Rolling calibrations' extract updated reconstruction constants from the data, which are then also written to the database. Finally, detailed monitoring distributions are plotted and used in the experiment's data quality monitoring program. OPR has been designed to keep up with DAQ with a minimum latency. A second farm of processors, using the same mechanisms as OPR, is used to reprocess older data once newer code or improved constants become available.

Chapter 3

Optimisation of Event Selection

3.1 Introduction

This chapter describes a 'cut-and-count' based analysis procedure required to obtain estimates of the branching fractions for $B^0 \to \pi^\pm K^\mp$, $B^\pm \to \pi^0 K^\pm$, $B^\pm \to \pi^\pm K^0_S$ and $B^0 \to \pi^0 K^0_S$. The two most critical issues of the analysis strategy are background suppression and particle identification. The dominant background in charmless two-body decays is from continuum $e^+e^- \to q\overline{q}$ production. Given the small branching fractions of $B \to \pi K$ decays ($\mathcal{O}$ (10^{-5})) and relatively large $q\overline{q}$ cross-section, obtaining a sample of $B \to \pi K$ is challenging.

The charged tracks resulting from charmless two-body B decays are of relatively high momentum (1.7-4.2 GeV/c). It is necessary to discriminate between kaons and pions. The Cherenkov angle θ_c, determined from the DIRC provides excellent K/π separation.

To separate signal from background events, a combination of sophisticated variables describing the topology of signal and background events are employed. A set of optimal selection cuts are chosen using these event shape variables and the number of signal events surviving the cuts are counted. This straightforward 'cut-and-count' analysis provides 'first-order' estimates of the numbers of signal events for each channel and a good approximation of the branching fractions to be expected.

The main goal of the whole analysis is to obtain an accurate determination of the yield of $B \to \pi K$ signal events. This is achieved by carrying out an Extended Maximum Likelihood fit to the data in 'Energy Substituted Mass' ($m_{\rm ES}$) and 'Delta

Energy' (ΔE). The tuned cuts are applied to the on-resonance data and the unbinned maximum likelihood fit is carried out. The fit incorporates the Cherenkov angle, θ_c, which is used to distinguish between the different types of signal. For example, $B^0 \to \pi^{\pm}K^{\mp}$ could have contributions from the decays $B^0 \to \pi^{\mp}\pi^{\pm}$ and $B^0 \to K^{\mp}K^{\pm}$. The details of the maximum likelihood analysis technique are given in Chapter 4.

In this chapter, the real and Monte Carlo data samples are described. The initial event selection criteria, which identify 'two body' events, are outlined. The reconstruction of K^0_S and π^0 and the use of the DIRC in K/π separation are also described. A discussion of the reduction of the number of background events contributing to the signal is also presented. An optimisation algorithm was used to identify the best combinations of cuts on various event shape variables. The efficiencies of these cuts are derived from samples of signal Monte Carlo events. Finally, the optimal selection criteria are applied to the on-resonance data and branching fractions are calculated.

3.2 Data Samples

The analyses presented in this thesis use the entire Run 1 data set of 20.7 fb^{-1} integrated luminosity, collected with the BaBar detector at the Stanford Linear Accelerator Center's PEP-II B Factory, between October 1999 and August 2000. This sample corresponds to 23 million $B\overline{B}$ pairs decaying from the $\Upsilon(4S)$ resonance with a c.m. energy of 10.58 GeV (on-resonance). A total of 3371 runs were required to accumulate this enormous amount of data. Only good runs, as flagged by the BaBar data quality processing, are used in this analysis. The main criteria for the goodness of a run are the status and performance of all subdetectors, as well as the total luminosity of the run. The DCH high voltage was decreased to 1900 V from 1960 V for a large part of Run 1, such that 11.2 fb^{-1} was collected using 1900 V and 9.4 fb^{-1} was collected using 1960 V. This contributed to a lower track reconstruction efficiency. At 1960 V, the average efficiency is measured to be $(98 \pm 1)\%$ per track, for tracks with $p_T > 200$ MeV/c and polar angles $\theta > 500$ mrad. At 1900 V, the average efficiency is about 5% lower for tracks of normal incidence. Monte Carlo events were generated with the correct mix of events with 1960 V and 1900 V. 2.6 fb^{-1} of data was also collected at 40 MeV below the $B\overline{B}$ threshold (off-resonance) for continuum background studies. The total amount of Run 1 on- and off-resonance data is summarised below.

- 22.57 ± 0.36 million on-resonance $B\overline{B}$ events (20.7 ± 0.3 fb^{-1}) [50]
- 2.61 ± 0.04 fb^{-1} off-resonance events

3.3 Monte Carlo Samples

Large quantities of `GEANT` 3 based Monte Carlo samples were generated in order to perform effective data/simulation comparisons. The generic background Monte Carlo samples include continuum u, d, s and c and $B\overline{B}$ events, with an approximately equal number of $B^0\overline{B}^0$ and B^+B^- events. A sample of MC charmless B decays was also used to obtain information on whether other charmless B decays contributed to the background events in the $B \to \pi K$ channels. This sample consisted of all channels which do not decay via a $b \to c$ transition. In order to estimate signal efficiencies for a given set of selection criteria, several samples of Monte Carlo signal were also generated. The size of the samples used are summarised below:

- 8.7 fb^{-1} $u\overline{u}$, $d\overline{d}$, $s\overline{s}$ continuum
- 9.4 fb^{-1} $c\overline{c}$ continuum
- 8.1 fb^{-1} generic $B\overline{B}$
- 112.2 fb^{-1} $B\overline{B}$ decay charmless final state
- 28 k events $B^0 \to \pi^\pm K^\mp$
- 22 k events $B^0 \to K^\mp K^\pm$
- 19 k events $B^0 \to \pi^\mp \pi^\pm$

- 22 k events $B^{\pm} \rightarrow \pi^0 K^{\pm}$
- 19 k events $B^{\pm} \rightarrow \pi^{\pm}\pi^0$
- 28 k events $B^{\pm} \rightarrow \pi^{\pm}K^0_S$
- 19 k events $B^{\pm} \rightarrow K^{\pm}K^0_S$
- 29 k events $B^0 \rightarrow \pi^0 K^0_S$

To make a realistic comparison to real data, the background Monte Carlo samples must be scaled to the data luminosity. The scaling factors, F_{sc}, are calculated in the following way.

If N_{sample} is the number of Monte Carlo events in a given sample, then:

$$F_{sc} = \frac{\sigma_{sample}\mathcal{L}}{N_{sample}} \tag{3.1}$$

where $\mathcal{L}$ is the integrated data luminosity and σ_{sample} is the cross-section of the process in question. The number of events in each generic Monte Carlo sample, the scaling factors F_{sc} used and the cross-sections used in equation 3.1 are shown in table 3.1. The cross-section for charmless B decays is not well known. The ratio $||V_{ub}|/|V_{cb}||^2 \sim 0.01$ and this value is adopted as an approximate magnitude of the cross-section of the charmless B decays. When scaling the number of signal

Sample	N_{sample}	$\sigma_{sample}(nb)$	F_{sc}
$B\overline{B}$	8482763	1.05	2.56
$u\overline{u}$ $d\overline{d}$ $s\overline{s}$	18191830	2.09	2.38
$c\overline{c}$	12222226	1.30	2.20
charmless	1122100	0.01	0.20

Table 3.1: The number of events in the generic Monte Carlo samples. The scaling factors, F_{sc}, and the process cross-sections are also given.

Monte Carlo events, an assumption of the branching fraction for each channel must be made. The branching fractions obtained recently by the Belle collaboration for $B \rightarrow \pi K$ [51] modes are adopted in this analysis. Table 3.2 summarises the number of events in the signal Monte Carlo samples and the Belle branching fractions $\mathcal{B}_{Belle}$ used in the calculation. The scaling factors are defined as:

$$F_{sc} = \frac{\sigma_{B\overline{B}}\mathcal{L}\mathcal{B}_{Belle}}{N_{sample}^{corrected}} \tag{3.2}$$

Using the Belle branching fractions, the signal yield for each channel in the Run 1 data set can be predicted. The Monte Carlo events were all forced to have the

Sample	$\mathcal{B}_{Belle} \times 10^{-6}$	Pred. Evts.	N_{sample}	$N_{sample}^{corrected}$	F_{sc}
$B^0 \to \pi^\pm K^\mp$	$19.3^{+3.4}_{-3.2}$	438	28000	28000	0.015
$B^\pm \to \pi^0 K^\pm$	$16.3^{+3.5}_{-3.3}$	370	22000	22268	0.016
$B^\pm \to \pi^\pm K^0_S$	$13.7^{+5.7}_{-4.8}$	310	28000	81621	0.004
$B^0 \to \pi^0 K^0_S$	$16.0^{+7.2}_{-5.9}$	363	29000	85564	0.004

Table 3.2: The number of events in the Signal Monte Carlo samples, the Belle branching fractions $\mathcal{B}_{Belle}$ used in the calculation (errors are statistical), the predicted number of events in the Run 1 sample and the scaling factors, F_{sc}, are given.

K^0_S decaying to two pions *i.e.* $K^0 \to K^0_S \to \pi^+\pi^-$ and π^0 mesons all decayed to two photons ($\pi^0 \to \gamma\gamma$). $K^0_S \to \pi^+\pi^-$ occurs $(68.61 \pm 0.28)\%$ [18] of the time (approximately two thirds). $K^0 \to K^0_S$ occurs 50 % of the time. Therefore, N_{sample} must be multiplied by ~ 2.915 in order to obtain $N_{sample}^{corrected}$. Similarly, $\pi^0 \to \gamma\gamma$ occurs $(98.798 \pm 0.032)\%$ [18] of the time. Thus, for channels containing a π^0, N_{sample} must be increased by $\sim 1\%$.

Use was also made of several other $B \to h'h$ channels in order to determine the degree to which other such channels might contribute to the $B \to \pi K$ signal yields. For example, $B^0 \to \pi^\pm K^\mp$ might have contributions from $B^0 \to \pi^\mp\pi^\pm$ and $B^0 \to K^\mp K^\pm$. The channels used and their quantities are shown in table 3.3.

3.4 Event Selection

3.4.1 Preselection

The analysis begins with the data being filtered to reduce backgrounds and select two body B decay candidates. Much of the background can be eliminated by simple

Sample	N_{sample}	$N^{corrected}_{sample}$
$B^0 \to \pi^{\mp}\pi^{\pm}$	19000	19000
$B^0 \to K^{\mp}K^{\pm}$	22000	22000
$B^{\pm} \to \pi^{\pm}\pi^0$	19000	19231
$B^{\pm} \to K^{\pm}K^0_S$	19000	55385

Table 3.3: The number of signal Monte Carlo events from other channels.

kinematic cuts which exploit the topological differences between $B\overline{B}$ and background events. A cut on the Fox-Wolfram moment [52] of $R_2 < 0.95$ removes two-prong τ decays. A sphericity cut, sphericity> 0.01, removes additional τ backgrounds and Bhabha events. The 'twobody' selector is designed to flag events which may be two body charmless decays. The decay products $h'^{+}h^{-}$, $h^{+}K^0_S$, $h^{+}\pi^0$, $\pi^0\pi^0$ $\pi^0K^0_S$ and $K^0_SK^0_S$ are formed by combining pairs of particles from charged tracks $h^{\pm}$, K^0_S and π^0. A set of loose cuts is used to select only those candidates which are consistent with a $B \to hh'$ decay (where h and h' are kaons or pions). The two daughter particles should also have approximately equal but opposite momenta in the c.m. The 'twobody' selector algorithm requires,

- invariant B mass cut, $|M_B - M_{B_{PDG}}| < 0.600$ GeV
- pion hypothesis assumed for charged tracks
- CMS momentum of B candidate $p^* < 1.5$ GeV

The efficiency of the selector, for various two body decays, evaluated with Monte Carlo signal events is shown in table 3.4. The efficiency is calculated as the raw number of events flagged as 'twobody' divided by the number of generated events.

3.4.2 Track Reconstruction

Tracks are reconstructed using the SVT and DCH detectors. Track candidates have a non-zero charge and are assigned the pion mass hypothesis. To be used in this analysis, tracks must also pass the following criteria:

- Minimum number of hits in the DCH is 12

channel	efficiency (%)
$B^0 \to \pi^\pm K^\mp$	84.0
$B^\pm \to \pi^0 K^\pm$	71.6
$B^\pm \to \pi^\pm K^0_S$	67.5
$B^0 \to \pi^0 K^0_S$	58.7
$B^0 \to \pi^\mp \pi^\pm$	84.0
$B^0 \to K^\mp K^\pm$	83.3
$B^\pm \to \pi^\pm \pi^0$	71.3
$B^\pm \to K^\pm K^0_S$	67.1

Table 3.4: The 'two-body' efficiency evaluated from Monte Carlo simulated signal decays.

- $p_T > 0.1\,\mathrm{GeV}$
- $p < 10.0$ GeV
- $0.41 < \theta < 2.54$ rads
- The absolute value of the distance of closest approach (DOCA) to the beam-spot in the $x - y$ plane is less than 1.5 cm
- The absolute value of the distance of closest approach to the beam-spot in the z direction is less than 10.0 cm

3.4.3 π^0 Reconstruction

π^0 mesons appear in the $B^\pm \to \pi^0 K^\pm$ and $B^0 \to \pi^0 K^0_S$ decay channels. The standard BaBar π^0 selection criteria, which produces a π^0 candidate list, is described here. This π^0 list is then included in the $B \to \pi K$ analysis at the stage when pions and kaons are being combined to form B candidates. π^0 mesons are reconstructed [46] in the two photon decay channel, $\pi^0 \to \gamma\gamma$. π^0 candidates are formed from neutral bumps with $E_\gamma > 30\,\mathrm{MeV}$. A cut on the 'lateral moment' of showers in the EMC is applied to further select π^0.

The lateral shower distributions from hadronic showers differ significantly from those from electromagnetic showers. If the number of crystals associated with a shower is given by N, the LAT of a shower is defined as [48],

$$LAT = \frac{\sum_{i=3}^{N} E_i r_i^2}{\sum_{i=3}^{N} E_i r_i^2 + E_1 R_0^2 + E_2 R_0^2} \tag{3.3}$$

Here, the energy deposits are labeled such that $E1 \geq E_2 \geq ..... \geq E_N$, R_0 is the average distance between crystals (=5 cm at BaBar) and r_i is the distance from the centre of the cluster to the centre of the i^{th} crystal. The discriminating power of this variable comes from the fact that electromagnetic showers are typically confined to one or two crystals, so that LAT is smaller for such showers than for hadronic ones. In this analysis, a cut on the LAT variable of LAT < 0.8 was used.

Only resolved π^0 candidates are used in this analysis, which mean that the two constituent photons form two distinct bumps in the EMC. If the π^0 mesons decay into two almost collinear photons, so that just one bump is recorded in the EMC, this is said to be a merged π^0. The merged π^0 candidates are rejected in this analysis. Previous studies have shown that merged π^0 make up only $\sim 10\%$ of the total number in the $B^{\pm} \to \pi^0 K^{\pm}$ and $B^0 \to \pi^0 K^0_S$ decay channels [58]. Candidates are initially required to have a raw mass $115 < m_{\pi^0} < 150\,\mathrm{MeV}/c$. The π^0 then has a mass fit applied, with the photon pair invariant mass constrained to the PDG value of the π^0 mass.

3.4.4 K^0_S Reconstruction

K^0_S mesons are used in the $B^{\pm} \to \pi^{\pm} K^0_S$ and $B^0 \to \pi^0 K^0_S$ analyses. Only $K^0_S \to \pi^+\pi^-$ is reconstructed. The standard BaBar selection criteria select K^0_S candidates and produce a common K^0_S list. Two oppositely charged pions are combined and form a K^0_S candidate by attempting to find a common vertex. The K^0_S has a $c\tau$ of 2.68 cm with an average boost of $\beta\gamma \sim 2.4$ and so has a decay distribution which extends away from the interaction point by a considerable amount. The vertex fit is required to have $\chi^2_{prob} > 0.01$ and the resultant invariant mass must be between 450 MeV/c^2 and 550 MeV/c^2. The decay point must be at least 2 mm from the primary vertex in the xy plane and no more than 50 cm away in any direction. The latter cut ensures that there are enough hits in the tracking system to provide an accurate measurement of the K_S^0 momentum. To ensure that the candidate really came from the primary vertex, a cut is made on the angle between the K_S^0 momentum vector and a line pointing from the primary vertex to its decay point. This angle must be no more than 150 mrad in the xy plane. Finally, only candidates which are within 25 MeV of the PDG K_S^0 mass are accepted. The mass is then recomputed at the vertex.

3.4.5 Selection of B Candidates

The beam energies are used in the calculation of two kinematic variables m_{ES} and ΔE, which are commonly used to separate signal from background events in the analysis of exclusive B meson decays. These variables are Lorentz invariants, are largely uncorrelated and can be evaluated in both the centre-of-mass and laboratory frames. The first variable, ΔE, can be expressed in Lorentz invariant form as,

$$\Delta E = (2q_B q_0 - s)/2\sqrt{s}, \tag{3.4}$$

where $\sqrt{s} = 2E^*_{beam}$ (E^*_{beam} is the beam energy in the centre-of-mass) is the total energy of the e^+e^- system in the c.m. frame, *i.e.* the invariant mass, and q_B and $q_0 = (E_0, \vec{p}_0)$ are the Lorentz 4-vectors representing the 4-momentum of the B candidate and of the e^+e^- system, $q_0 = q_{e^+} + q_{e^-}$. In the c.m. frame, ΔE takes the familiar form

$$\Delta E = E^*_B - E^*_{beam}, \tag{3.5}$$

where E^*_B is the reconstructed energy of the B meson. The ΔE distribution receives a sizable contribution from the beam energy spread, but is generally dominated by detector resolution. This energy distribution is taken as a calibration of E^*_{beam}, with an absolute error of 1.1 MeV, dominated by the error in the measurement of the B mass.

The second variable is the energy-substituted mass, m_{ES}, defined as ${m_{\mathrm{ES}}}^2 = q_B^2$. with the constraint $\Delta E = 0$. In the laboratory frame, m_{ES} can be determined from the measured three-momentum $\vec{p}_B$ of the B candidate without explicit knowledge of the masses of the decay products:

$$m_{\rm ES} = \sqrt{\frac{(s/2 + \vec{p}_B.\vec{p}_0)^2}{E_0^2 - p_B^2}}. \tag{3.6}$$

In the c.m. frame ($\vec{p}_0 = 0$), this variable takes the familiar form

$$m_{\rm ES} = \sqrt{E^{*2}_{beam} - p^{*2}_B}, \tag{3.7}$$

where the B meson energy is substituted by E^*_{beam}. The direction of the beams relative to BaBar is determined using $e^+e^-\to e^+e^-$ and $e^+e^-\to\mu^+\mu^-$ events. The resultant uncertainty in the direction of the boost from the laboratory to the center-of-mass frame, $\vec{\beta}$, is approximately 1 mrad, dominated by alignment errors. This leads to an uncertainty of about 0.3 MeV in $m_{\rm ES}$.

In the analysis of $B^0 \to \pi^\pm K^\mp$, two charged tracks (h, h') are combined to reconstruct the B^0. A vertex algorithm is used to estimate the decay vertex of the candidate B. The momentum vectors of the daughter particles are recalculated using this point as their production vertex. Simple 4-vector addition is then used to form the $B \to h^{'+}h^-$. Similarly, a track is combined (without vertexing) with a π^0 or a K^0_S to form $B \to \pi^0 h$ and $B \to K^0_S h$. Whether h is a kaon or a pion is determined later by using information from the DIRC. The pion mass is assigned to a track when reconstructing the B candidate and when calculating ΔE. Therefore, modes such as $B^0 \to \pi^\pm K^\mp$ and $B^0 \to K^\mp K^\pm$ will have a ΔE value which is not centred on zero, but is shifted to negative values by a quantity which depends on the momenta of the kaon tracks. This is due to the fact that the candidate energies are calculated in the CM system and the boost to that frame depends on the mass hypothesis of the track. The fully reconstructed B candidates are then required to have $\mid \Delta E \mid < 0.5\,\mathrm{GeV}$ and $5.2 < m_{\rm ES} < 5.3\,\mathrm{GeV}$.

3.5 Particle Identification

It is crucial in the analyis of $B \to \pi K$ channels to be able to distinguish between charged kaons and pions. Since the charged tracks resulting from charmless two body decays are of relatively high momentum, 1.7 - 4.2 GeV/c, the Cherenkov angle, θ_c, determined from the DIRC, is the most effective tool for K/π discrimination. Two complementary methods of exploiting the particle identification capabilities of the DIRC are used in this analysis. The first method is used in the cut-based analysis and utilises measurements of θ_c and track momentum, p, to derive an expression for the mass of the track. From the equations,

$$\cos\theta_c = \frac{1}{\beta n_{quartz}} \tag{3.8}$$

and,

$$p = \gamma\beta m \tag{3.9}$$

it can be shown that,

$$m^2 = p^2(n_{quartz}^2 \cos^2\theta_c - 1) \tag{3.10}$$

Figure 3.1 shows the distribution of the square of the masses of the charged tracks in the DIRC. The mass squared is used in order to avoid problems with the square root of a negative number. The three peaks are pions, kaons and protons, respectively. Events with $m^2 < 0.5$ are selected, thus rejecting protons. Cuts on m^2 to select charged kaons and pions are applied: $0.20 \leq m_{K^{\mp}}^2 \leq 0.30$ GeV^2 and $-0.10 \leq m_{\pi^{\mp}}^2 \leq 0.10$ GeV^2. These cuts are not incorporated in the cut optimisation procedure and are used only to provide an approximate method of differentiating between kaons and pions for the 'cut-and-count' analysis. The maximum likelihood fit analysis in Chapter 4 includes θ_c in the fit, and is therefore a more sophisticated and reliable technique of separating the kaons and pions.

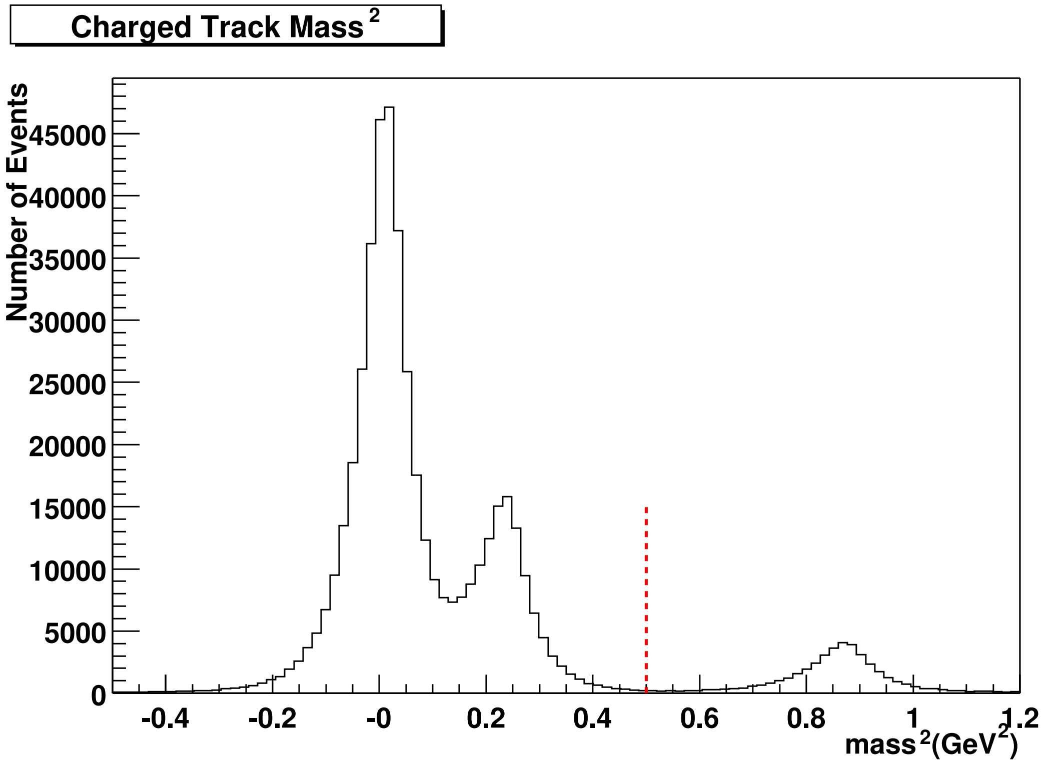

Figure 3.1: *The mass of charged tracks, obtained from the θ_c measurement from the DIRC. The peaks are (from left to right) $\pi^{\mp}$, $K^{\mp}$ and protons.*

3.6 Background Suppression

The cross-section for $e^+e^- \to q\overline{q}$ (where q can be u, d, s, or c) is larger than the cross-section for the process $e^+e^- \to b\overline{b}$ (see table 3.1). Therefore, at the $\Upsilon(4S)$ resonance there is a considerable background from the continuum production of light quarks. Charmless hadronic $B \to \pi K$ decays are dominated by a background of such continuum events. The main focus of the analysis is to effectively extricate the signal events from the background, without compromising the efficiency of the signal selection. To differentiate between background and signal events, the differences in topology of signal and continuum events are exploited. In $\Upsilon(4S)$ production of $B\overline{B}$ pairs, the B mesons are produced almost at rest in the centre-of-mass frame, and their decay axes are uncorrelated. These events are rather spherical in shape and can be distinguished from jetlike continuum events using a variety of event shape variables.

3.6.1 Event Shape Variables

This section briefly gives the definitions of the event shape variables which were considered in this analysis. The Fox-Wolfram moment and the sphericity are used by the 'twobody' selector as described in section 3.4.1. A number of event shape variables were used during the analysis optimisation procedure, which attempts to maximise the number of signal events, while minimising the number of background events using a combination of cuts on event shape variables. The variables used in this process were; the Fox-Wolfram moment, sphericity and the angle between the K and the thrust axis in the CM frame. All of these variables were evaluated for the 'rest of the event', *i.e.* the event with the $B \to \pi K$ candidate removed. The K_S^0 decay length significance and the 'helicity' of the π^0 were also considered as means to reject fake K_S^0 and π^0 respectively.

The Fox-Wolfram moment (R_l)

The Fox-Wolfram moment (R_l) is defined as,

$$R_l = \sum_{i,j} \frac{|\vec{p}_i||\vec{p}_j|}{E_{vis}^2} P_l\Big(\cos(\theta)\Big) \tag{3.11}$$

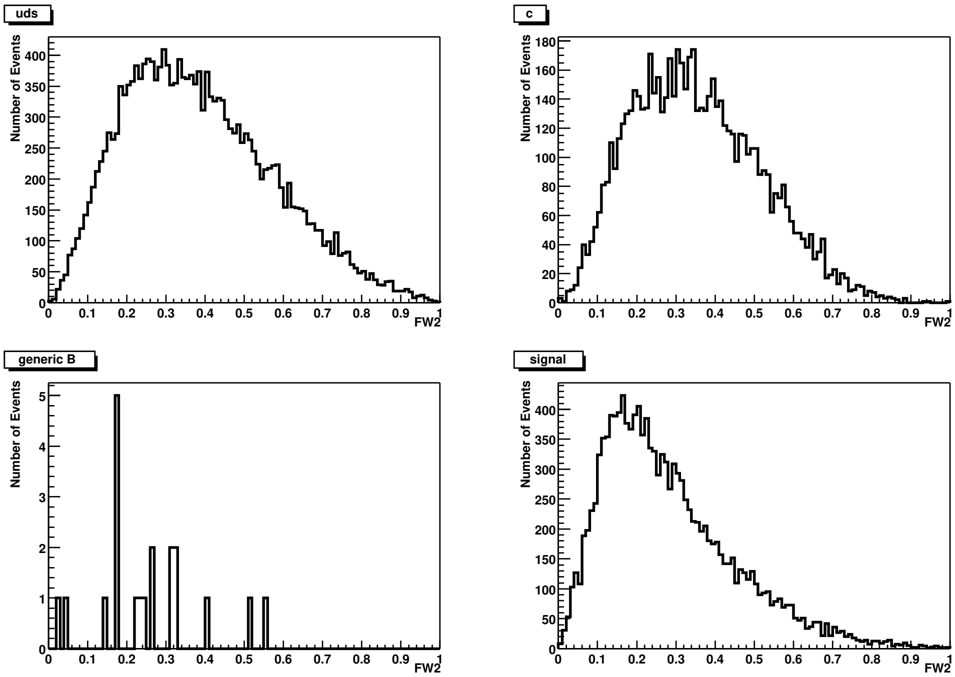

Figure 3.2: *The second Fox-Wolfram moment (FW2) distribution for; top left: $u\overline{u}$, $d\overline{d}$, $s\overline{s}$, top right: $c\overline{c}$, bottom left: generic $B\overline{B}$ and bottom right: signal MC are shown*

Here, P_l are the Legendre polynomials, E_{vis} is the total visible energy, $\vec{p}_i$ is the momentum of particle i and θ_{ij} is the opening angle between particles i and j. The zeroth order Legendre polynomial is given by

$$P_0 = \frac{1}{2} \tag{3.12}$$

and the second order polynomial, P_2, is given by,

$$P_2 = \frac{1}{2}(3\cos^2\theta_{i,j} - 1) \tag{3.13}$$

The normalised second Fox-Wolfram moment is then given by,

$$FW2 = \frac{R_2}{R_0} = 3\sum_{i,j} \frac{|\vec{p}_i||\vec{p}_j|}{E_{vis}^2}\left[\cos^2(\theta_{ij}) - 1\right] \tag{3.14}$$

R_2 is 0 for a perfectly spherical event, and 1 for an event completely collimated around the jet axis. Figure 3.2 shows an example of the distributions obtained for signal and continuum Monte Carlo in $B \to \pi K$ modes. The signal and background distributions do not differ significantly and would therefore be ineffective in separating signal from background. The 'twobody' selector does make use of the

Fox-Wolfram moment and retains events with $R_2 < 0.95$, rejecting μ and τ two-prong events.

Sphericity

The 'sphericity' axis [53] of an event is calculated by minimising the quantity:

$$S = MIN\left(\frac{\sum_i {p_T}_i^2}{\sum_i |\vec{p}_i|^2}\right) \tag{3.15}$$

The alignment of a daughter of the B candidate is calculated with respect to the sphericity axis $\vec{\hat{n}}_S$, which describes the global orientation of the tracks assigned to the recoiling B. p_T is relative to $\vec{\hat{n}}_S$ and $\vec{\hat{n}}_S$ defines the jet direction and the minimised value of S gives the nature of the shape of the event. A value of $S = 1$ would represent a spherically symmetrical event, while a value of $S = 0$ would mean that the event was particularly jetty in nature. Figure 3.3 indicates that for

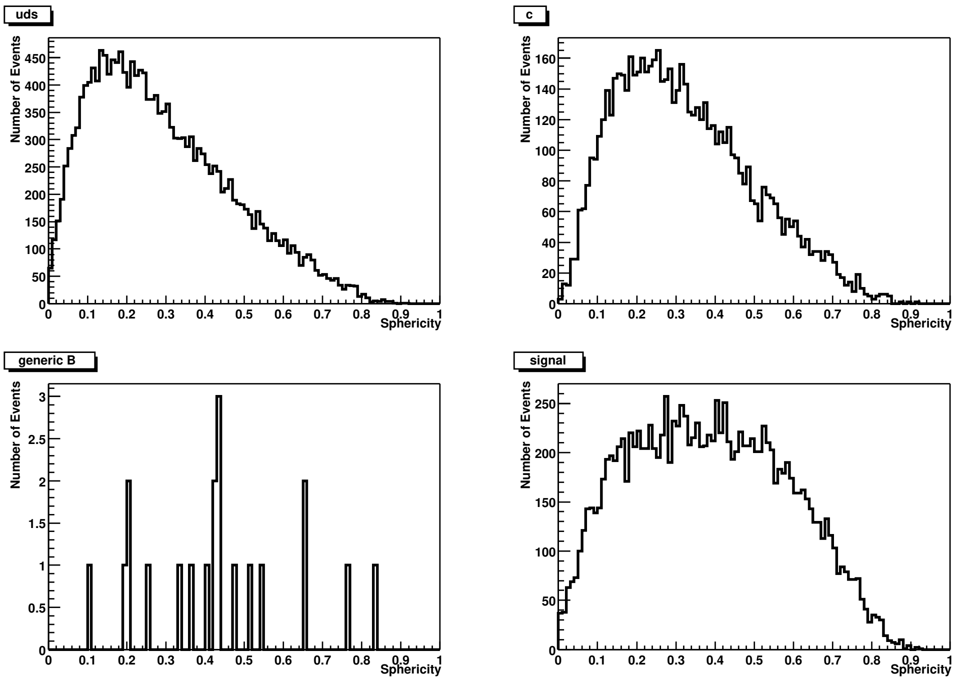

Figure 3.3: *The sphericity distributions for; top left: $u\overline{u}$, $d\overline{d}$, $s\overline{s}$, top right: $c\overline{c}$, bottom left: generic $B\overline{B}$ and bottom right: signal MC are shown.*

the $B \to \pi K$ events being analysed, no significant difference between signal and background Monte Carlo events is evident. The distribution of signal Monte Carlo extends over the region $0 \leq S \leq 0.9$. Therefore, the sphericity offers no convincing discriminating power in this instance. However, the 'twobody' selector utilises the sphericity variable and removes events with sphericity > 0.01, thus eliminating additional τ backgrounds and Bhabha events.

Angle between Thrust Axis and Kaon Decay $\cos\theta_K$

A powerful variable used to reject background in this analysis is the cosine of the angle between thrust axis of the rest of the event and the direction of flight of the K candidate ($\cos\theta_K$) coming from a $B \to \pi K$ decay. The thrust [54] of an event is calculated by maximising the quantity:

$$T = MAX\left(\frac{\sum_i |\vec{n}_T.\vec{p}_i|}{\sum_i |\vec{p}_i|}\right) \tag{3.16}$$

where $\vec{n}_T$, the thrust axis, is a unit vector along the jet direction. The direction of $\vec{n}_T$ is adjusted to maximise the thrust T (the forward and backward thrust direction are equivalent). Low values of T, near zero, imply spherical events, while values of T near 1 reveal the jettiness of an event. Figure 3.4 shows the distributions of signal and background Monte Carlo for thrust. The thrust was not used as a separate variable in the cut optimisation procedure. In the CM frame, the K and π candidates are approximately back-to-back. The $B \to \pi K$ candidate is removed and the thrust axis ($\vec{n}_T$) of the 'rest of the event' is calculated. The angle between the K candidate and $\vec{n}_T$ in the CM frame is then θ_K. The exact meaning of this variable is best described by figure 3.5. Signal events have a flat distribution in $\cos\theta_K$, while the jetty continuum background events will peak at one and minus one in $\cos\theta_K$.

Figure 3.6 shows that a clear difference in the distributions of the signal $B \to \pi K$ decays and the continuum background is evident.

K_S^0 Decay Length Significance

True K_S^0 candidates are selected using the decay length significance $l_{K_S^0}/\sigma_l$, where $l_{K_S^0}$ is the measured 2-dimensional decay distance of the K_S^0 and σ_l is its error.

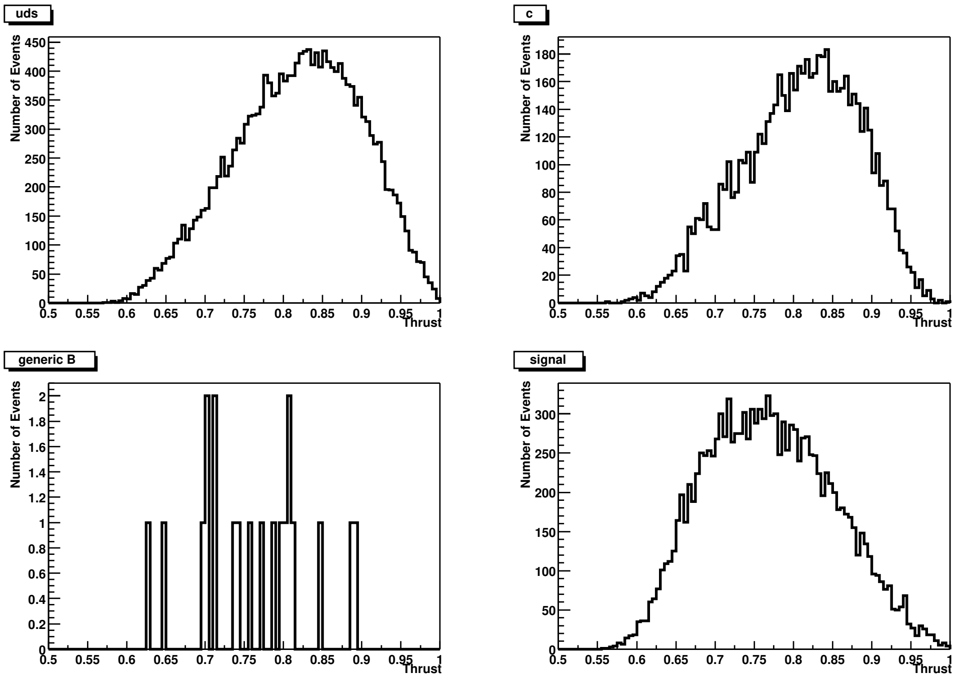

Figure 3.4: *The thrust distributions for; top left: $u\overline{u}$, $d\overline{d}$, $s\overline{s}$, top right: $c\overline{c}$, bottom left: generic $B\overline{B}$ and bottom right: signal MC.*

Figure 3.7 clearly shows the noticable difference in the K_S^0 decay length significance distributions of true and fake K_S^0. True K_S^0 particles have a flat distribution, whereas fake K_S^0 mesons peak at zero.

π^0 Helicity

The helicity is defined as the photon decay angle in the π^0 rest frame with respect to the π^0 laboratory momentum. Fake π^0 in charmless two body decays are dominated by random combinations of one high and one low energy photon. The fake candidates appear as highly asymmetric decays and are easily identified in the π^0 helicity distribution. Fake π^0 mesons are seen to strongly peak at $\cos\theta \sim 1$. Figure 3.8 shows that the π^0 mesons in signal and background are real and have not been misidentified, therefore, this variable does not provide good signal/backgound differentiation. The spike at zero is due to the presence of merged π^0 mesons in the sample.

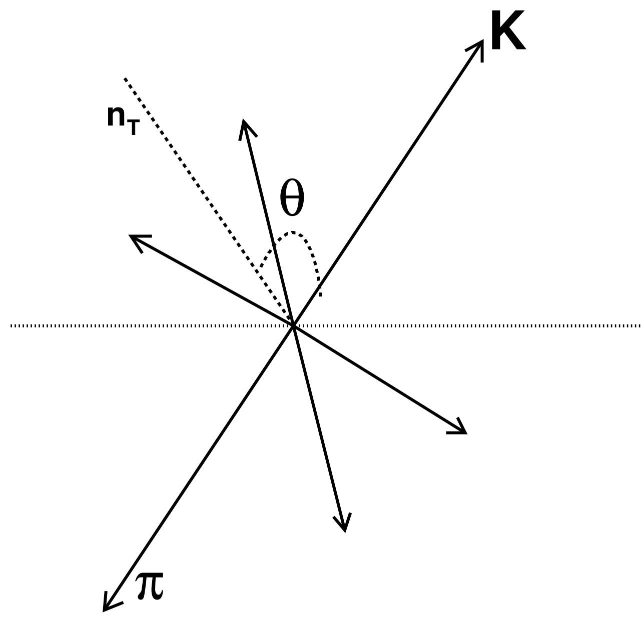

Figure 3.5: *Schematic showing the angle, θ_K, between the thrust axis ($\hat{\mathbf{n_T}}$) of the rest of the event and the direction of flight of the K candidate.*

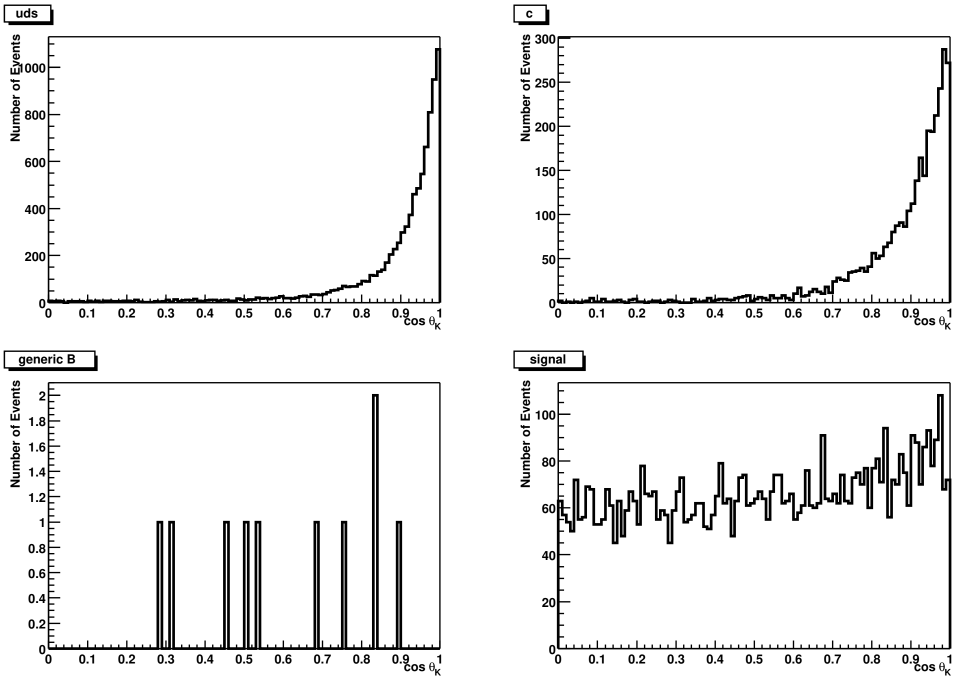

Figure 3.6: *The distributions of the cosine of the angle between the K and the rest of the event, $\cos\theta_K$ for; top left: $u\overline{u}$, $d\overline{d}$, $s\overline{s}$, top right: $c\overline{c}$, bottom left: generic $B\overline{B}$ and bottom right: signal MC.*

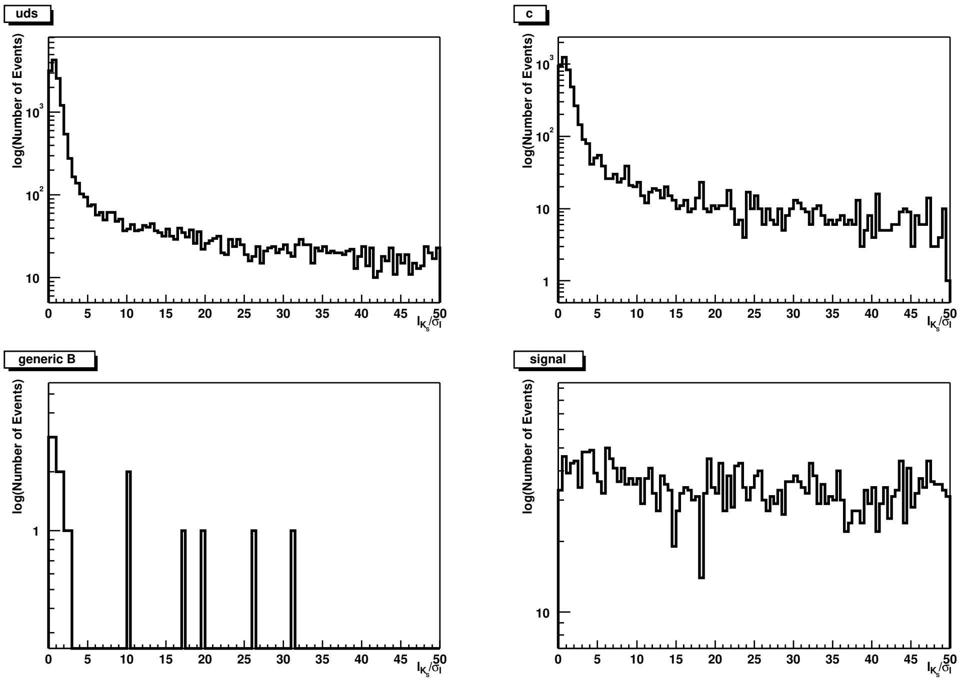

Figure 3.7: *The K^0_S decay length significance, $l_{K^0_S}/\sigma_l$ for; top left: $u\overline{u}$, $d\overline{d}$, $s\overline{s}$, top right: $c\overline{c}$, bottom left: generic $B\overline{B}$ and bottom right: signal MC.*

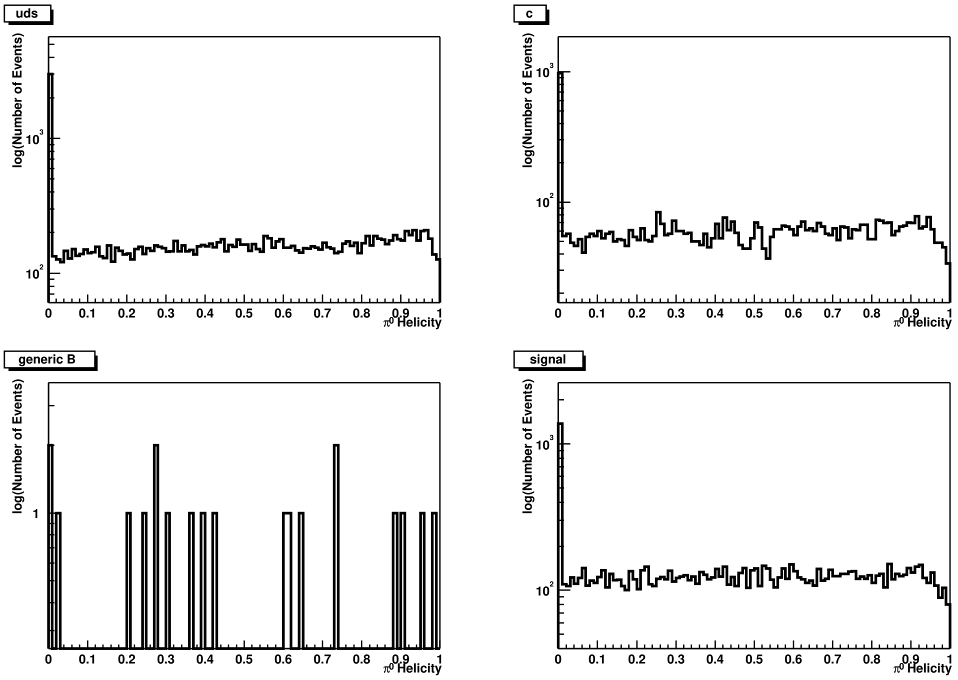

Figure 3.8: *The distributions of the cosine of the π^0 helicity for; top left: $u\overline{u}$, $d\overline{d}$, $s\overline{s}$, top right: $c\overline{c}$, bottom left: generic $B\overline{B}$ and bottom right: signal MC .*

3.7 Optimisation of Cuts

A set of selection criteria must be found which reduces the background effectively without compromising the yield of signal events. Samples of Monte Carlo simulated background and signal events were used to maximise the statistical significance of the signal yield. The statistical significance is defined as a quality factor, Q, where,

$$Q = \frac{N_S}{\sqrt{(N_S + N_B)}} \tag{3.17}$$

and N_S is the number of signal events and N_B is the number of background events. For each sample of signal and background Monte Carlo events, a large plane in m_{ES} and ΔE was defined with $5.2 < m_{\mathrm{ES}} < 5.3\,\mathrm{GeV}/c^2$ and $-0.5 < \Delta E < 0.5\,\mathrm{GeV}$. A small area around the expected signal region was then also defined. Figures 3.9, 3.10, 3.11, 3.12 show scatter plots of signal Monte Carlo in m_{ES} and ΔE for each $B \to \pi K$ mode and the boundaries of the signal regions chosen. The boundaries of the signal region for each channel studied are summarised in table 3.5. The expected signal region was defined to be within $\sim 1 - 2\sigma$ of the B mass for each mode, since the maximum likelihood fit, to be carried out later, would identify real $B \to \pi K$ in such an area. Modes containing a π^0 have wider boundaries in ΔE to accommodate low energy tails due to energy leakage from the EMC crystals.

Channel	m_{ES} low (GeV/c^2)	m_{ES} high (GeV/c^2)	ΔE low (GeV)	ΔE high (GeV)
$B^0 \to \pi^{\pm} K^{\mp}$	5.275	5.283	-0.10	0.00
$B^{\pm} \to \pi^0 K^{\pm}$	5.271	5.285	-0.15	0.05
$B^{\pm} \to \pi^{\pm} K^0_S$	5.275	5.285	-0.06	0.06
$B^0 \to \pi^0 K^0_S$	5.274	5.287	-0.17	0.10

Table 3.5: The boundaries in the m_{ES} and ΔE plane of the small signal region.

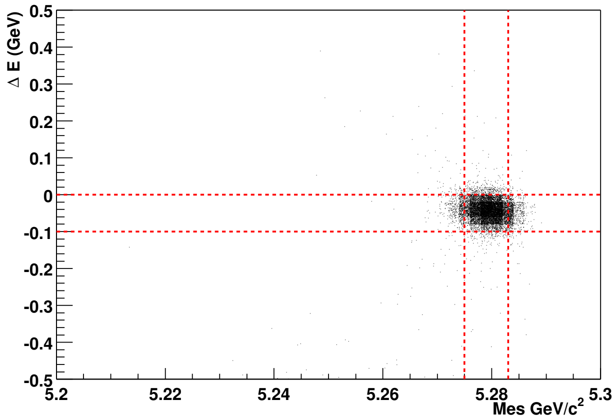

Figure 3.9: *$B^0 \to \pi^\pm K^\mp$ scatter plot in m_{ES} and ΔE, with $5.2 < m_{\mathrm{ES}} < 5.3\,\mathrm{GeV}/c^2$ and $-0.5 < \Delta E < 0.5\,\mathrm{GeV}$.*

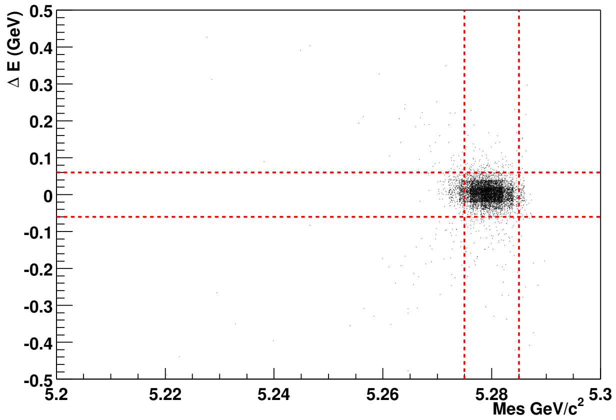

Figure 3.10: *$B^\pm \to \pi^\pm K^0_s$ scatter plot in m_{ES} and ΔE, with $5.2 < m_{\mathrm{ES}} < 5.3\,\mathrm{GeV}/c^2$ and $-0.5 < \Delta E < 0.5\,\mathrm{GeV}$.*

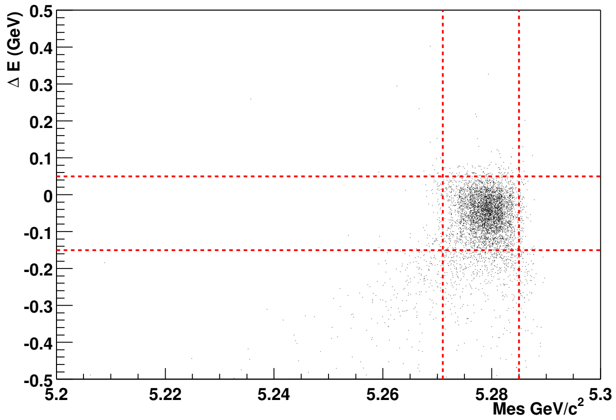

Figure 3.11: *$B^\pm \to \pi^0 K^\pm$ scatter plot in $m_{\rm ES}$ and ΔE, with $5.2 < m_{\rm ES} < 5.3\,{\rm GeV}/c^2$ and $-0.5 < \Delta E < 0.5\,{\rm GeV}$.*

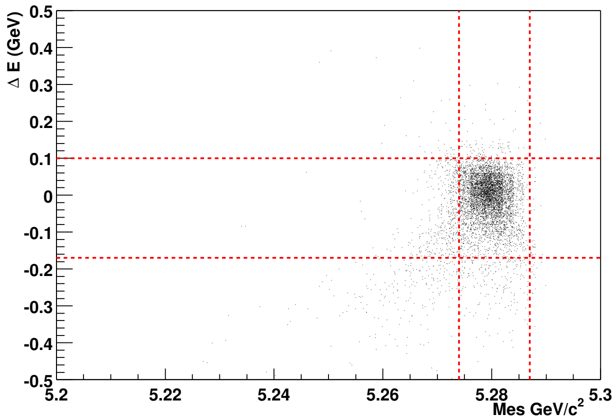

Figure 3.12: *$B^0 \to \pi^0 K^0_s$ scatter plot in $m_{\rm ES}$ and ΔE, with $5.2 < m_{\rm ES} < 5.3\,{\rm GeV}/c^2$ and $-0.5 < \Delta E < 0.5\,{\rm GeV}$.*

While the samples of signal Monte Carlo were more than adequate in size, the available amount of continuum backround Monte Carlo was not sufficient to accurately model the backgound present in $B \to \pi K$ decays. Simply applying cuts to the background and signal Monte Carlo samples and obtaining values of N_S and N_B was not a viable method of cut optimisation. In order to circumvent this problem, a cut optimisation algorithm was devised, which was based on the assumption that as a series of cuts was varied, the ratio of the number of events in the 'large box' (defined by the plane in $5.2 < m_{\mathrm{ES}} < 5.3\,\mathrm{GeV}/c^2$ and $-0.5 < \Delta E < 0.5\,\mathrm{GeV}$) to the number of events in the small signal region ('small box') would remain constant. This ratio was determined by the numbers of events in the large and small boxes without applying any of the cuts. The number of events was scaled to the luminosity accordingly, thus giving an estimate of N_B. N_S was ascertained directly from the number of signal events in the small box surviving the cuts. All possible permutations of the event shape variables were tried until a maximum value of Q was reached. The combination of cuts giving such a Q value was considered to be the optimal selection criteria for the particular $B \to \pi K$ channel being studied. The optimal selection criteria for each of the four $B \to \pi K$ channels, their corresponding Q values and signal efficiency (ϵ) are summarised in table 3.6.

The column labelled 'π^0 dau' is the number of daughter particles from the decay

Channel	FW2	sph	$\cos\theta_K$	K_S^0 Life	π^0 helicity	π^0 dau	Q value	ϵ
$B^0 \to \pi^\pm K^\mp$	1.0	0.0	0.80	NA	NA	NA	7.92	21.14
$B^\pm \to \pi^0 K^\pm$	1.0	0.0	0.69	NA	1.0	2	5.24	16.38
$B^\pm \to \pi^\pm K_S^0$	1.0	0.0	0.66	14	NA	NA	1.92	7.71
$B^0 \to \pi^0 K_S^0$	1.0	0.0	0.64	14	1.0	2	1.79	6.28

Table 3.6: Summary of optimal selection criteria, Q values and efficiency, ϵ, for signal.

of the π^0 in the channels $B^\pm \to \pi^0 K^\pm$ and $B^0 \to \pi^0 K_S^0$. One daughter would imply that the two photons were colinear, and therefore 'merged'. Two daughters means the π^0 to two resolvable photons in the EMC. The optimisation procedure showed that the two-daughter π^0 mesons should be used in the analysis. As expected, some of the variables used in the optimisation procedure have very little discriminating power and no increase in efficiency or statistical significance is obtained by cutting on them. The variation of Q against cut value for the event shape variables are shown in figures 3.13 to 3.17.

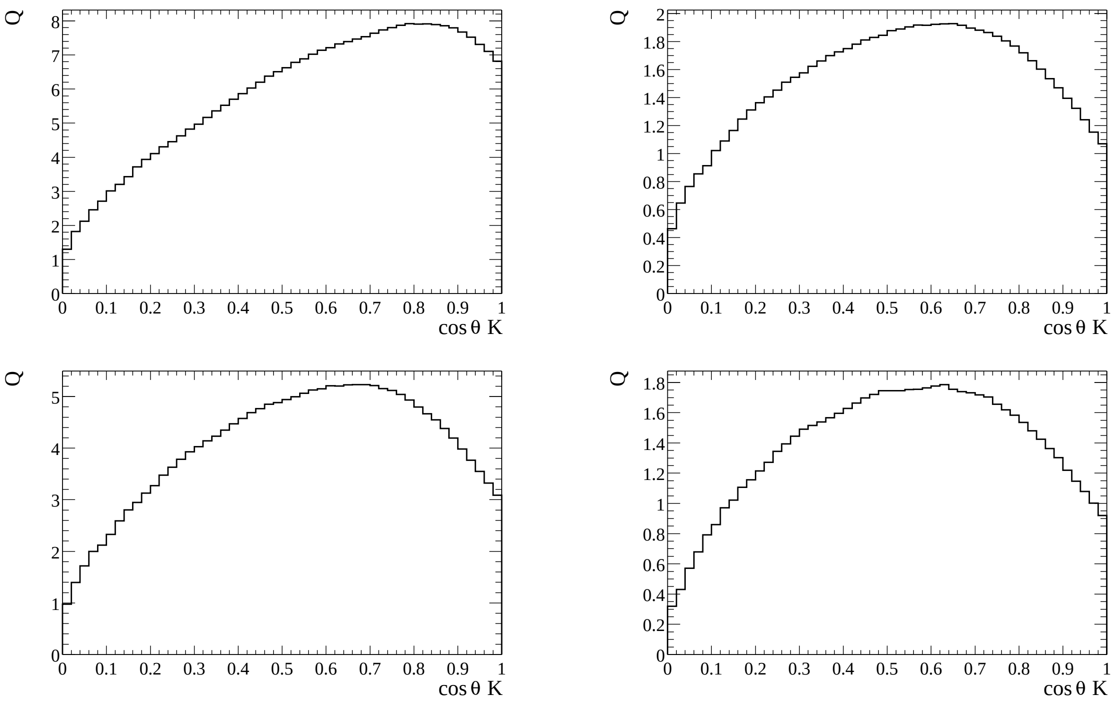

Figure 3.13: *Variation of Q value with $\cos\theta_K$ for; top left: $B^0 \rightarrow \pi^{\pm}K^{\mp}$, top right: $B^{\pm} \rightarrow \pi^{\pm}K^0_s$, bottom left: $B^{\pm} \rightarrow \pi^0 K^{\pm}$ and bottom right: $B^0 \rightarrow \pi^0 K^0_s$.*

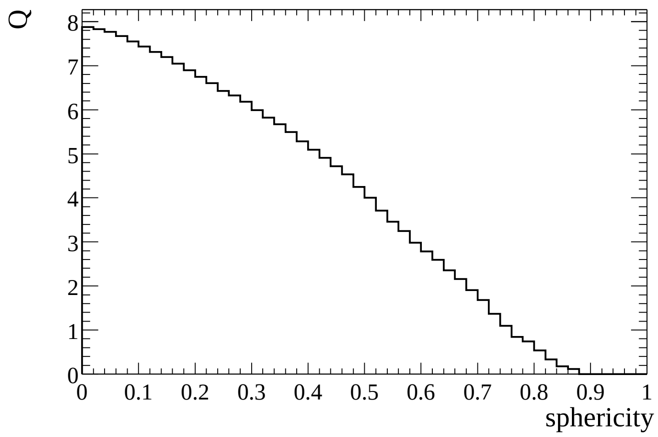

Figure 3.14: *Variation of Q value with sphericity for $B^0 \to \pi^{\pm}K^{\mp}$.*

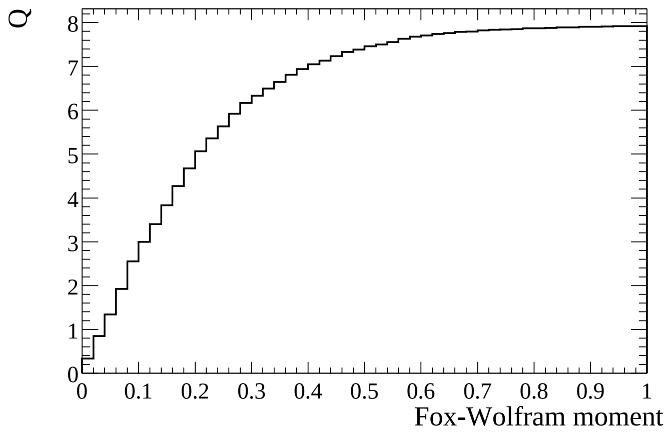

Figure 3.15: *Variation of Q value with Fox-Wolfram Moment for $B^0 \to \pi^{\pm}K^{\mp}$.*

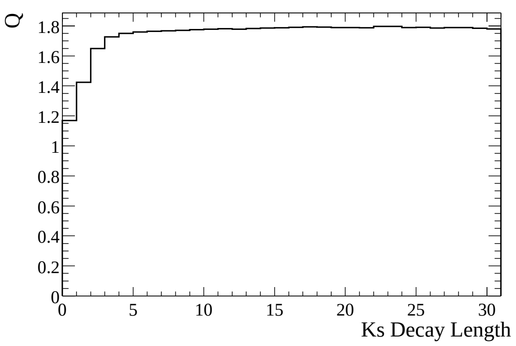

Figure 3.16: *Variation of Q value with K_s^0 decay length significance for $B^0 \to \pi^0 K_s^0$.*

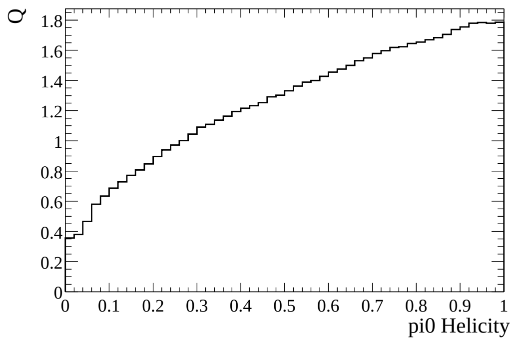

Figure 3.17: *Variation of Q value with the cosine of the π^0 helicity for $B^0 \to \pi^0 K^0_S$.*

3.8 Cut-Based Analysis

The optimal cuts were applied to the on-resonance data and the number of events remaining in the signal region (N_{on}) were counted. The number of real signal events (N_{real}) could be derived from,

$$N_{real} = N_{on} - N_B \tag{3.18}$$

An estimate of the branching fraction for each mode could then be obtained from,

$$\mathcal{B} = \frac{N_{real}}{\epsilon \cdot N_{B\overline{B}}} \tag{3.19}$$

where ϵ is the signal efficiency and $N_{B\overline{B}}$ is the total number of $B\overline{B}$ pairs. The statistical error on the branching fraction, $\sigma_{\mathcal{B}}$, is given by,

$$\sigma_{\mathcal{B}} = \left(\frac{\sqrt{N_{on}}}{\epsilon \cdot N_{B\overline{B}}} \right) \tag{3.20}$$

Table 3.7 summarises the yields of the real signal events and the branching fractions for each $B \to \pi K$ mode. The scaled number of events remaining in the off-resonance sample, N_{off}, after applying the cuts (which should be compared to N_B, the number of Monte Carlo background events) are also given in table 3.7. The branching fraction ($\mathcal{B}$) has been calculated using N_B, $\mathcal{B}_{off}$ has been calculated using N_{off}.

Channel	N_B	N_{off}	N_S	N_{on}	N_{real}	$\mathcal{B} \times (10^{-6})$	$\mathcal{B}_{off} \times (10^{-6})$
$B^0 \to \pi^{\pm} K^{\mp}$	47.49	18.88	94.30	86	38.51	8.0 ± 1.9	14.1 ± 1.9
$B^{\pm} \to \pi^0 K^{\pm}$	73.90	40.11	60.81	80	6.09	1.6 ± 2.4	10.7 ± 2.4
$B^{\pm} \to \pi^{\pm} K^0_S$	27.73	25.08	24.27	54	26.27	15.0 ± 4.2	16.6 ± 4.2
$B^0 \to \pi^0 K^0_S$	34.49	30.96	24.29	43	8.50	5.8 ± 4.5	8.5 ± 4.5

Table 3.7: The number of signal Monte Carlo events surviving the cuts and the number of real signal events and branching fractions. The errors are statistical only.

3.9 Conclusions

The main purpose of the cut-based analysis was to obtain a set of optimal selection cuts using Monte Carlo generated events and apply these cuts to the data and thus calculate preliminary values for the branching fractions of $B^0 \to \pi^\pm K^\mp$, $B^\pm \to \pi^\pm K^0_S$, $B^\pm \to \pi^0 K^\pm$ and $B^0 \to \pi^0 K^0_S$. This form of analysis revealed the possible number of $B \to \pi K$ decay events in the BaBar Run 1 data sample. Branching fractions of $\mathcal{O}\ (10^{-6})$ (table 3.7) are to be expected. Table 3.7 also shows that there can be a considerable difference between the number of off-resonance events, N_{off}, and the number of Monte Carlo simulated background events, N_B. This discrepancy will naturally effect the branching fraction results listed in table 3.7, since $N_{real} = N_{on} - N_B$ or $N_{real} = N_{on} - N_{off}$. If the amount of background in the signal regions is estimated using the off-resonance data, different branching fractions are calculated. These values are also given in table 3.7. The Monte Carlo appears to over estimate the number of background events. The distributions of event shape variables in figures 3.2 - 3.8 indicate that the main contribution to the background comes from continuum events, rather than generic $B\overline{B}$ events. A further observation is that a large over-estimation in the number of Monte Carlo background events appears to be confined to decays containing a $K^\pm$.

While the 'cut-and-count' analysis provides us with a general idea of what the $B \to \pi K$ branching fractions are, it is not adequate to state definite results. The extended maximum likelihood fit analysis, to be described in the next chapter, is a much more sophisticated and reliable method for ascertaining signal event yields and thus calculating branching fractions. However, it is useful to be able to compare the results of the 'cut-and-count' analysis with the extended maximum likelihood fit analysis as a sanity check.

Chapter 4

Maximum Likelihood Fit Analysis

4.1 Introduction

The analysis technique described in this chapter uses an unbinned multivariate extended maximum likelihood (ML) fit based on fitting to the variables m_{ES}, ΔE and θ_c for the Run 1 on-resonance data sample. This chapter describes and documents the Probability Density Functions (PDF's) adopted for the maximum likelihood fit for each of the $B \to \pi K$ channels being studied ($B^0 \to \pi^{\pm} K^{\mp}$, $B^{\pm} \to \pi^{\pm} K_S^0$, $B^{\pm} \to \pi^0 K^{\pm}$ and $B^0 \to \pi^0 K_S^0$). The yields of signal and background events from the fit are tabulated and the branching ratios are calculated for each mode. A discussion of the possible sources of systematic errors in the analysis then follows. A 'Toy Monte Carlo' study was also performed to examine the correctness of the fitting procedure and the potential correlations between the fit components. A maximum likelihood fit was also carried out to investigate any charge asymmetries in the $B^0 \to \pi^{\pm} K^{\mp}$, $B^{\pm} \to \pi^{\pm} K_S^0$ and $B^{\pm} \to \pi^0 K^{\pm}$ channels. Systematic errors in the charge asymmetry results are dealt with in the final part of this chapter.

4.2 Extended Maximum Likelihood Fit

For each input event, the likelihood ($\mathcal{L}_i$) is defined as,

$$\mathcal{L}_i = \sum_{j=1}^{m} n_j \mathcal{P}_j(x_i), \tag{4.1}$$

where $\mathcal{P}_j(x_i)$ are the probabilities for each of the m event types evaluated with the observables $\vec{x}_i$ of the i^{th} event. n_j are the free parameters of the fit and give the total number of events of each event type. The PDF's for each variable are assumed to be uncorrelated and so $\mathcal{P}_j$ are the product of the probability distribution functions (PDF's) for each of the observables. Each of the PDF's typically involves several parameters that are determined with Monte Carlo samples and are fixed for the ML fit.

For N input events, the overall likelihood is,

$$\mathcal{L} = \frac{e^{-(\sum n_i)}}{N!} \prod_{i=1}^{N} \mathcal{L}_i, \tag{4.2}$$

where the first term takes into account the Poisson fluctuations in the total number of events. This expression represents the extended maximum likelihood function (EML). The aim of the extended maximum likelihood method is to find the number of signal and background events in a given data sample that maximises the likelihood function $\mathcal{L}$.

Before the fit is carried out, the optimised cuts, chosen during the 'cut and count' procedure, are applied to the full Run 1 data sample. After the relevant PDF's have been found, they are used to form the likelihood function. The fit then finds the values of n_i, the number of events for each hypothesis i. The PDF input variables, x_i, used in the EML fits are m_{ES}, ΔE and θ_c.

4.3 Probability Distribution Functions (PDF's)

In this section, the functional forms of the PDF's used in the maximum likelihood fit are described. Table 4.1 summarises the types of function used to characterise m_{ES} and ΔE in the signal Monte Carlo samples for each $B \to \pi K$ channel. The values of the parameters of each PDF are then documented as the maximum likelihood fit analysis of each mode is dealt with.

4.3.1 The Gaussian Distribution

The Gaussian distribution,

$$G(x : \mu : \sigma) = \frac{1}{\sigma\sqrt{2\pi}}.e^{(-(x-\mu)^2/(2\sigma^2))} \tag{4.3}$$

where μ is the mean of the distribution and σ is the peak width.

channel	m_{ES}	ΔE
$B^0 \to \pi^{\pm} K^{\mp}$	Double Gaussian	Double Gaussian
$B^0 \to \pi^{\mp} \pi^{\pm}$	Double Gaussian	Double Gaussian
$B^0 \to K^{\mp} K^{\pm}$	Double Gaussian	Double Gaussian
$B^{\pm} \to \pi^{\pm} K^0_S$	Crystal Ball	Crystal Ball
$B^{\pm} \to K^{\pm} K^0_S$	Crystal Ball	Crystal Ball
$B^{\pm} \to \pi^0 K^{\pm}$	Crystal Ball	Crystal Ball
$B^{\pm} \to \pi^{\pm} \pi^0$	Crystal Ball	Crystal Ball
$B^0 \to \pi^0 K^0_S$	Crystal Ball	Crystal Ball

Table 4.1: Summary table of functions used to determine the PDF's for the ML fit.

4.3.2 Crystal Ball Lineshape distribution

The Crystal Ball Lineshape distribution [56] consists of a Gaussian signal peak matched to a power law tail:

$$f(x) = N \cdot \begin{cases} exp(-\frac{(x-\bar{x})^2}{2\sigma^2}) & (x-\bar{x})/\sigma > \alpha \\ A \times (B - \frac{(x-\bar{x})}{\sigma})^{-n} & (x-\bar{x})/\sigma \leq \alpha \end{cases}$$

where $A \equiv (n/|\alpha|)^n \times exp(-|\alpha|^2/2)$ and $B \equiv n/|\alpha| - |\alpha|$. N is a normalisation factor, $\bar{x}$ and σ are the fitted peak position and width of the Gaussian portion of the function, and α is the fitted point at which the function crosses over to the power function and n is the exponent of the power function. A and B are defined so as to maintain the continuity of the function and its first derivative at α.

4.3.3 The Argus Background Distribution

The ARGUS distribution [57] was used to parameterise the background shape in an m_{ES} plot,

$$A(x : x_0, c) = \frac{1}{N} x \sqrt{1 - (x/x_0)^2} e^{(\xi(1-(x/x_0)^2))}, \tag{4.4}$$

where, x_0 represents the kinematic upper limit for the constrained mass and is held fixed at half the centre of mass energy (5.29 GeV for $e^+e^- \to \Upsilon(4S)$). The minimum value of x_0 must be $\geq$ the maximum value of x. N is a normalisation factor and ξ is a fit parameter.

4.3.4 Polynomial distribution

The polynomial distribution, of order n

$$P(x : c_0, ..., c_n) = \frac{1}{N}\left(1 + \sum_{k=1}^{n} c_k x^k\right) \tag{4.5}$$

A first order polynomial distribution was used to describe the background shape in ΔE distributions.

4.3.5 DIRC Cherenkov Angle PDF's

The method used to determine the DIRC Cherenkov PDF's is described in [58], but a brief outline of the technique is also given here. A very pure sample of kaon and pion tracks is derived from reconstructed $D^{*+} \to D^0\pi^+ \to (K^-\pi^+)\pi^+$ decays. The $\pi(K)$ track is always the one with the same (opposite) charge as the D^*. The control sample used is limited to those decays for which one of the D^0 daughter tracks is in the momentum range 1.75-4.25 GeV/c. This sample is used to evaluate and parameterise the θ_c measurement from the DIRC for high momentum tracks.

4.3.6 Analysis of $B^0 \to \pi^\pm K^\mp$

The $B^0 \to \pi^\pm K^\mp$ signal Monte Carlo distributions for m_{ES} and ΔE are described using double Gaussians. Since the pion mass is assigned to a track when calculating ΔE, the ΔE distributions for $B^0 \to \pi^\pm K^\mp$ and $B^0 \to K^\mp K^\pm$ are not centered on zero, but are shifted to negative values of $-50\,\mathrm{MeV}$ and $-90\,\mathrm{MeV}$, respectively. Table 4.2 summarises the values of the m_{ES} signal peak means (μ) and widths (σ), fm_{ES} is the proportion of the main Gaussian in the fit. The statistical errors on these values are negligible and are not included in the tables below. Table 4.3 summarises

Channel	μ_1 GeV/c^2	$\sigma_1(\times 10^{-3})$ GeV/c^2	μ_2 GeV/c^2	$\sigma_2(\times 10^{-2})$ GeV/c^2	fm_{ES}
$B^0 \to \pi^\pm K^\mp$	5.279	2.473	5.271	1.552	0.986
$B^0 \to \pi^\mp \pi^\pm$	5.279	2.479	5.277	2.253	0.988
$B^0 \to K^\mp K^\pm$	5.279	2.485	5.271	1.821	0.991

Table 4.2: Double Gaussian parameters for m_{ES} distributions of $B \to h^\pm h^\mp$.

Channel	$\mu_1(\times 10^{-2})$ GeV	$\sigma_1(\times 10^{-2})$ GeV	$\mu_2(\times 10^{-2})$ GeV	σ_2 GeV	$f_{\Delta E}$
$B^0 \to \pi^{\pm} K^{\mp}$	-4.306	2.378	-12.734	0.244	0.979
$B^0 \to \pi^{\mp}\pi^{\pm}$	0.167	2.083	-7.434	0.1885	0.975
$B^0 \to K^{\mp}K^{\pm}$	-8.819	2.064	-12.445	0.267	0.981

Table 4.3: Double Gaussian parameters for ΔE distributions of $B \to h^{\pm}h^{\mp}$.

the values of the ΔE signal peak means (μ) and widths (σ), $f_{\Delta E}$ is the proportion of the main Gaussian in the fit. The two distributions, each comprising a double Gaussian, are multiplied together. Figures 4.1, 4.2, 4.3 show the fitted Monte Carlo signal samples for $B^0 \to \pi^{\pm}K^{\mp}$, $B^0 \to \pi^{\mp}\pi^{\pm}$ and $B^0 \to K^{\mp}K^{\pm}$. The combined PDF's describing $m_{\rm ES}$ and ΔE are then used in the EML fit. The positively and negatively charged tracks are considered separately and the Cherenkov angles, θ_+ and θ_-, of the positively and negatively charged tracks are used in the fit. The unbinned extended maximum likelihood fit technique developed for the analysis of $B^0 \to \pi^{\pm}K^{\mp}$ determines a total of ten parameters from the data:

- $N_{\pi K}$, the number of $B \to \pi K$ decays, of either charge combination;
- fraction, $f_{\pi K}$, of $\pi^- K^+$ in $N_{\pi K}$;
- $N_{\pi\pi}$, the number of $B \to \pi^+\pi^-$ decays;
- N_{KK}, the number of $B \to K^+K^-$ decays;
- $N_{b\pi K}$, the number of background $\pi^{\mp}K^{\mp}$ decays;
- fraction, $f_{b\pi K}$, of background $\pi^- K^+$ in $N_{b\pi K}$;
- $N_{b\pi\pi}$, the number of background $\pi^+\pi^-$ decays;
- N_{bKK}, the number of background K^+K^- decays;
- ξ, Argus background shape parameter;
- the first order polynomial ΔE background shape parameter.

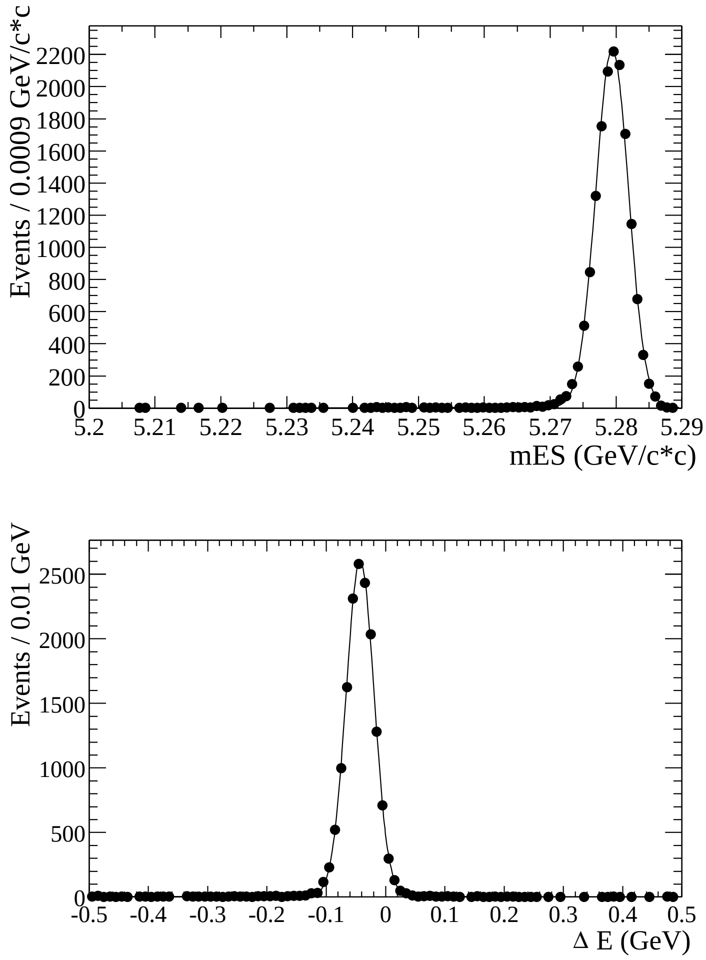

Figure 4.1: *$m_{\rm ES}$ (top) and ΔE (bottom) distributions in the signal $B^0 \to \pi^\pm K^\mp$ Monte Carlo sample.*

The PDF $\mathcal{P}_j$ is the sum of signal and background terms,

$$\begin{aligned}
\mathcal{P}(m_{\rm ES}, \Delta E, \theta_c) &= \frac{N_{\pi\pi}}{N}\mathcal{P}_{\pi\pi} + \frac{N_{b\pi\pi}}{N}\mathcal{P}_{b\pi\pi} \\
&+ \frac{N_{KK}}{N}\mathcal{P}_{KK} + \frac{N_{bKK}}{N}\mathcal{P}_{bKK} \\
&+ \frac{N_{\pi^-K^+}}{N} f_{\pi K}\mathcal{P}_{\pi^-K^+} + \frac{N_{b\pi^-K^+}}{N} f_{b\pi K}\mathcal{P}_{b\pi^-K^+} \\
&+ \frac{N_{\pi^+K^-}}{N}(1 - f_{\pi K})\mathcal{P}_{\pi^+K^-} + \frac{N_{b\pi^+K^-}}{N}(1 - f_{b\pi K})\mathcal{P}_{b\pi^+K^-} \quad (4.6)
\end{aligned}$$

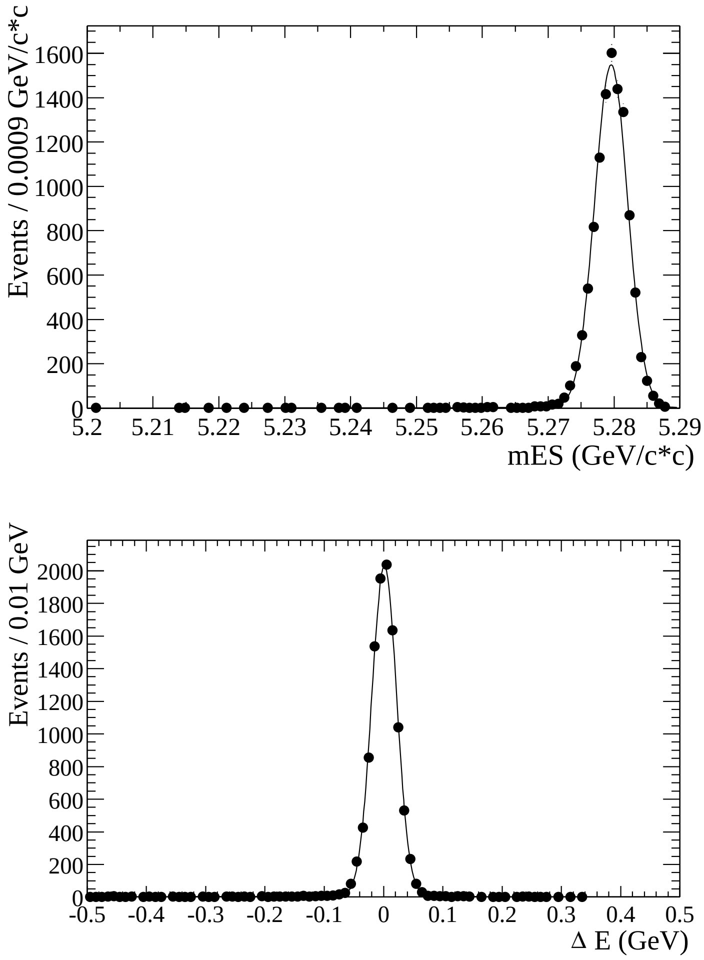

Figure 4.2: *m_{ES} (top) and ΔE (bottom) distributions in the signal $B^0 \to \pi^{\mp}\pi^{\pm}$ Monte Carlo sample.*

where $N \equiv \sum_k N_k$ is the total number of events. The PDF for each component, in turn, is the product of the PDF's for each of the input variables:

$$\mathcal{P}_k = \mathcal{P}_k m_{\mathrm{ES}} \mathcal{P}_{k\Delta E} \mathcal{P}_{k\theta_+} \mathcal{P}_{k\theta_-} \tag{4.7}$$

The signal and background event yields obtained from the EML fit are summarised in table 4.4. Figure 4.4 shows the m_{ES} and ΔE distributions fitted to real data. The m_{ES} data mass peak plot was produced by first cutting on ΔE in the interval $-0.10 \leq \Delta E \leq 0.00\,\mathrm{GeV}$. The integral of the background was calculated. The fit was then normalised from this integral. The ΔE data plot was also calculated in a

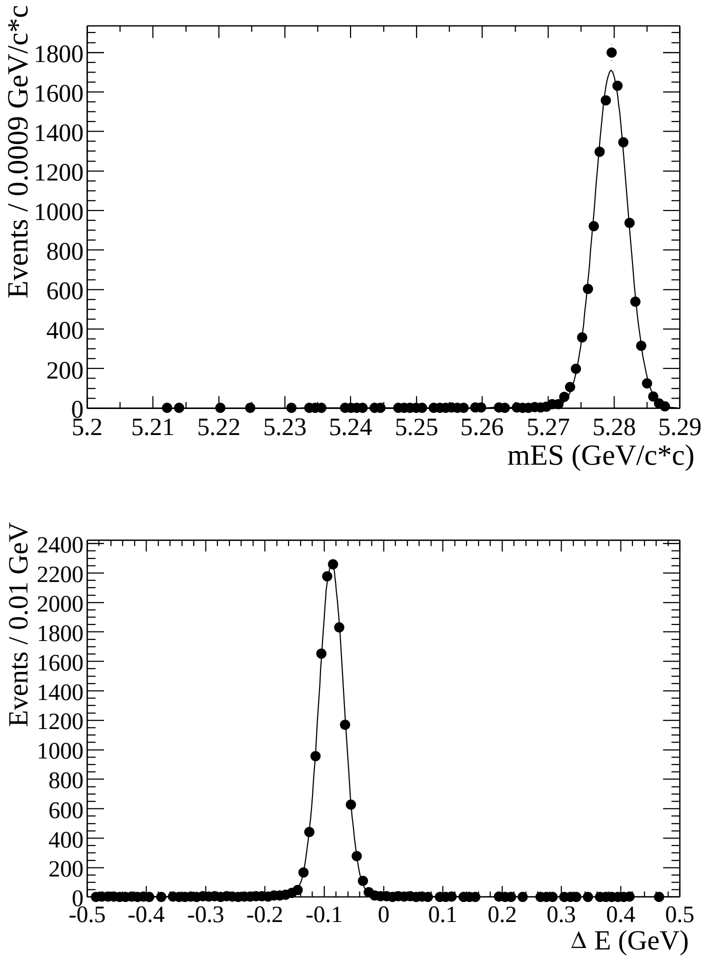

Figure 4.3: *m_{ES} (top) and ΔE (bottom) distributions in the signal $B^0 \to K^{\mp}K^{\pm}$ Monte Carlo sample.*

similar way, but a cut of $5.275 \leq m_{\mathrm{ES}} \leq 5.283$ GeV was applied. The data plots for the remaining $B \to \pi K$ modes were also made using this method. The m_{ES} and ΔE cuts which were applied to each data sample are summarised in table 3.5.
The $B^0 \to \pi^{\pm}K^{\mp}$ m_{ES} distribution has a clear invariant mass peak at 5.279 GeV/c^2, with the background fitted with the Argus function. The ΔE distribution also has a signal peak, which is negatively offset from zero at approximately -50 MeV, due to the pion mass having been assigned to the charged tracks.

Fit Variable	Fitted Value
$N_{\pi\pi}$	23.0 $\pm$ 11.0
$N_{\pi K}$	126.0 $\pm$ 16.0
N_{KK}	17.0 $\pm$ 7.0
$N_{b\pi\pi}$	14309.0 $\pm$ 125.0
$N_{b\pi K}$	9078.0 $\pm$ 150.0
N_{bKK}	4704.0 $\pm$ 74.0
$f_{\pi K}$	0.5 $\pm$ 0.1
$f_{b\pi K}$	0.5 $\pm$ 0.1
ξ	-15.1 $\pm$ 0.7
bkg ΔE	-0.83 $\pm$ 0.02

Table 4.4: Signal and background event yield obtained from maximum likelihood fit of $B \to h^{\pm}h^{\mp}$.

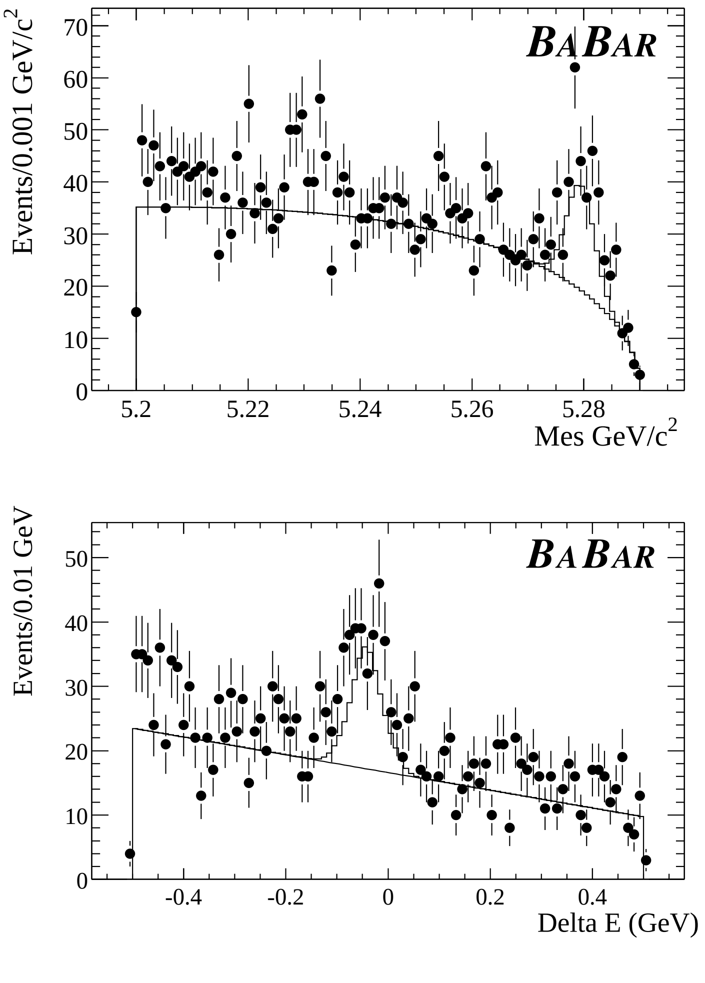

Figure 4.4: *Distributions of m_{ES} (top) and ΔE (bottom) for events enhanced in signal $B^0 \to \pi^{\pm}K^{\mp}$ decays. The solid curve shows the shape of the background and signal.*

4.3.7 Analysis of $B^{\pm} \to \pi^{\pm} K_S^0$

The m_{ES} and ΔE distributions of $B^{\pm} \to \pi^{\pm} K_S^0$ and $B^{\pm} \to K^{\pm} K_S^0$ signal Monte Carlo were fitted using the Crystal Ball function. The parameters obtained from the fits are summarised in tables 4.5 and 4.6. The fits are shown in figures 4.5 and 4.6. The unbinned extended maximum likelihood fit technique developed for the

Channel	μ_1 GeV/c^2	$\sigma_1(\times 10^{-3})$ GeV/c^2	α	n
$B^{\pm} \to \pi^{\pm} K_S^0$	5.279	2.479	3.068	1.459
$B^{\pm} \to K^{\pm} K_S^0$	5.279	2.457	2.185	3.379

Table 4.5: Crystal Ball fit parameters for m_{ES} distributions of $B^{\pm} \to h^{\pm} K_S^0$.

Channel	$\mu_1(\times 10^{-2})$ GeV	$\sigma_1(\times 10^{-2})$ GeV	α	n
$B^{\pm} \to \pi^{\pm} K_S^0$	0.504	2.026	2.000	1.568
$B^{\pm} \to K^{\pm} K_S^0$	-4.185	2.283	2.284	1.119

Table 4.6: Crystal Ball fit parameters for ΔE distributions of $B^{\pm} \to h^{\pm} K_S^0$.

analysis of $B^{\pm} \to \pi^{\pm} K_S^0$ determines a total of six parameters from the data:

- $N_{\pi K_S^0}$, the number of $B \to \pi K_S^0$ decays;
- $N_{K K_S^0}$, the number of $B \to K K_S^0$ decays;
- $N_{b\pi K_S^0}$, the number of background $B \to \pi K_S^0$ decays;
- $N_{bK K_S^0}$, the number of background $B \to K_S^0 K$ decays;
- ξ, Argus background shape parameter;
- the first order polynomial ΔE background shape parameter.

The PDF is the sum of signal and background terms,

$$\begin{aligned} \mathcal{P}(m_{\text{ES}}, \Delta E, \theta_c) &= \frac{N_{\pi K_S^0}}{N} \mathcal{P}_{\pi K_S^0} + \frac{N_{b\pi K_S^0}}{N} \mathcal{P}_{b\pi K_S^0} \\ &+ \frac{N_{K K_S^0}}{N} \mathcal{P}_{K K_S^0} + \frac{N_{bK K_S^0}}{N} \mathcal{P}_{bK K_S^0} \end{aligned} \tag{4.8}$$

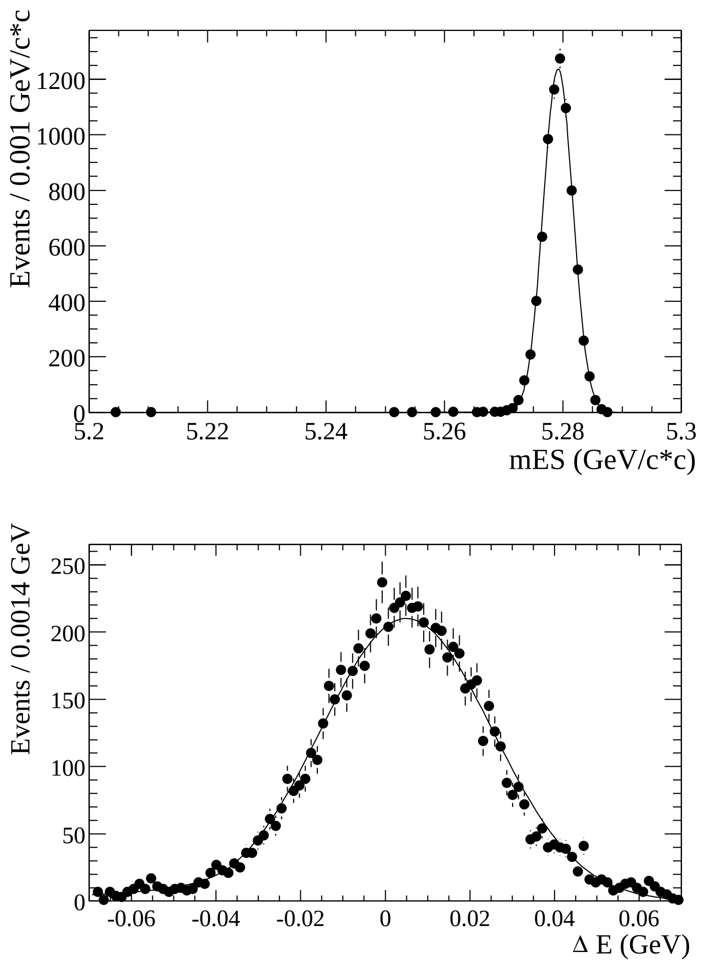

Figure 4.5: *$m_{\rm ES}$ (top) and ΔE (bottom) distributions in the signal $B^{\pm} \to \pi^{\pm} K^0_s$ Monte Carlo sample.*

The signal and background event yields obtained from the EML fit are summarised in table 4.7. Figure 4.7 shows the data distributions of $m_{\rm ES}$ and ΔE. The $B^{\pm} \to \pi^{\pm} K^0_s$ $m_{\rm ES}$ distribution has a clear invariant mass peak at 5.279 GeV/c^2, with the background fitted with the Argus function. ΔE has a clear peak centered on zero.

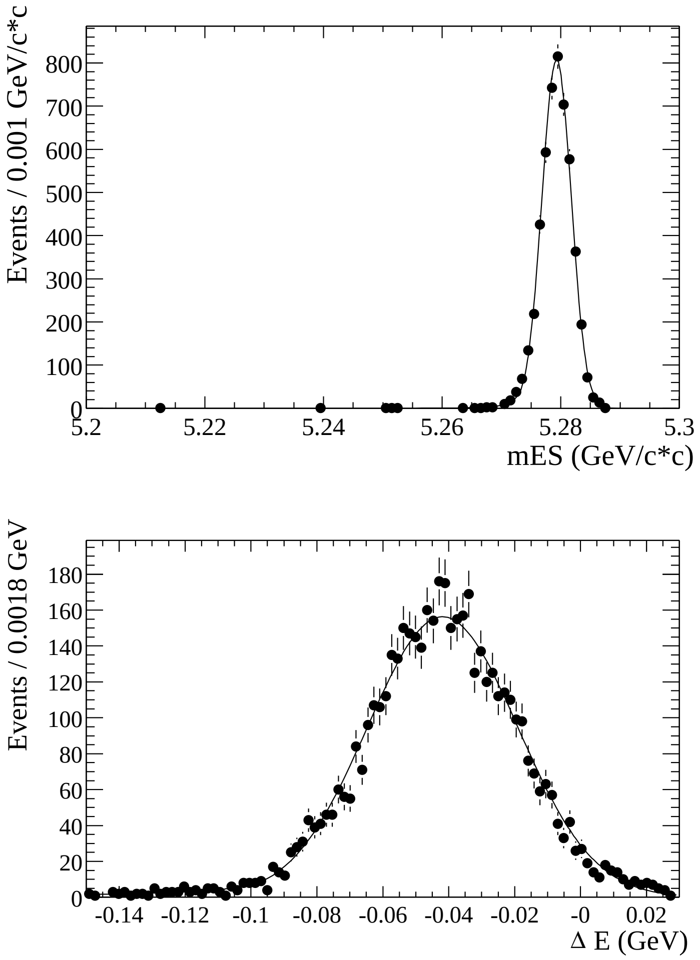

Figure 4.6: m_{ES} *(top) and* ΔE *(bottom) distributions in the signal* $B^{\pm} \rightarrow K^{\pm} K_s^0$ *Monte Carlo sample.*

Fit Variable	Fitted Value
$N_{\pi K_S^0}$	31.0 $\pm$ 7.0
$N_{KK_S^0}$	0.0 $\pm^{9.0}_{0.0}$
$N_{b\pi K_S^0}$	3064.0 $\pm$ 60.0
$N_{bKK_S^0}$	2202.0 $\pm$ 46.0
ξ	-19.0 $\pm$ 2.0
bkg ΔE	-1.10 $\pm$ 0.04

Table 4.7: Event yields obtained from the maximum likelihood fit of $B^{\pm} \rightarrow h^{\pm} K_s^0$.

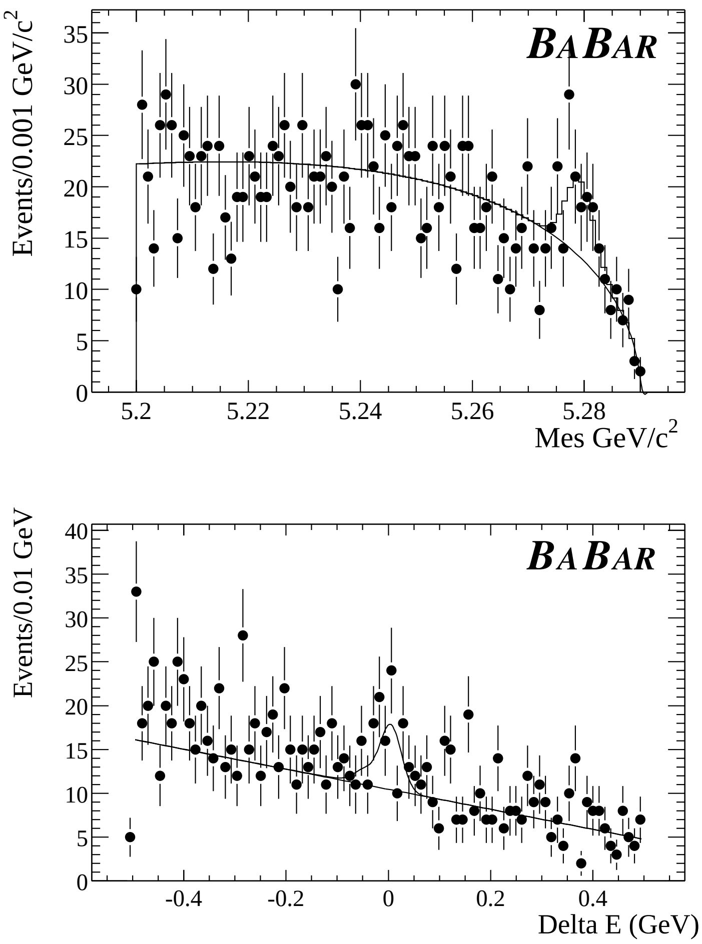

Figure 4.7: *Distributions of m_{ES} (top) and ΔE (bottom) for events enhanced in signal $B^{\pm} \rightarrow \pi^{\pm} K_s^0$ decays. The solid curve shows the shape of the background and signal.*

4.3.8 Analysis of $B^{\pm} \to \pi^0 K^{\pm}$

The $m_{\rm ES}$ and ΔE distributions of $B^{\pm} \to \pi^0 K^{\pm}$ and $B^{\pm} \to \pi^{\pm}\pi^0$ signal Monte Carlo were also fitted using the Crystal Ball function. The parameters obtained from the fits are summarised in tables 4.8 and 4.9. The fits, with the Crystal Ball function superimposed, are shown in figures 4.8 and 4.9. The unbinned extended maximum likelihood fit technique developed for the analysis of $B^{\pm} \to \pi^0 K^{\pm}$ determines a total of six parameters from the data:

Channel	μ_1 GeV/c^2	$\sigma_1(\times 10^{-3})$ GeV/c^2	α	n
$B^{\pm} \to \pi^0 K^{\pm}$	5.279	2.928	1.099	3.851
$B^{\pm} \to \pi^{\pm}\pi^0$	5.279	2.974	1.371	2.435

Table 4.8: Crystal Ball fit parameters for $m_{\rm ES}$ distributions of $B^{\pm} \to h^{\pm}\pi^0$.

Channel	$\mu_1(\times 10^{-2})$ GeV	$\sigma_1(\times 10^{-2})$ GeV	α	n
$B^{\pm} \to \pi^0 K^{\pm}$	-4.321	4.718	0.785	3.833
$B^{\pm} \to \pi^{\pm}\pi^0$	0.932	4.233	7.546	2.841

Table 4.9: Crystal Ball fit parameters for ΔE distributions of $B^{\pm} \to h^{\pm}\pi^0$.

- $N_{\pi^0 K}$, the number of $B \to \pi^0 K$ decays;
- $N_{\pi^0 \pi}$, the number of $B \to K^0_S K$ decays;
- $N_{b\pi^0 K}$, the number of background $B \to \pi^0 K$ decays;
- $N_{b\pi^0 \pi}$, the number of background $B \to \pi^0 \pi$ decays;
- ξ, Argus background shape parameter;
- the first order polynomial ΔE background shape parameter.

$$\begin{aligned} \mathcal{P}(m_{\rm ES}, \Delta E, \theta_c) &= \frac{N_{\pi^0 K}}{N}\mathcal{P}_{\pi^0 K} + \frac{N_{b\pi^0 K}}{N}\mathcal{P}_{b\pi^0 K} \\ &+ \frac{N_{\pi^0 \pi}}{N}\mathcal{P}_{\pi^0 \pi} + \frac{N_{b\pi^0 \pi}}{N}\mathcal{P}_{b\pi^0 \pi} \end{aligned} \tag{4.9}$$

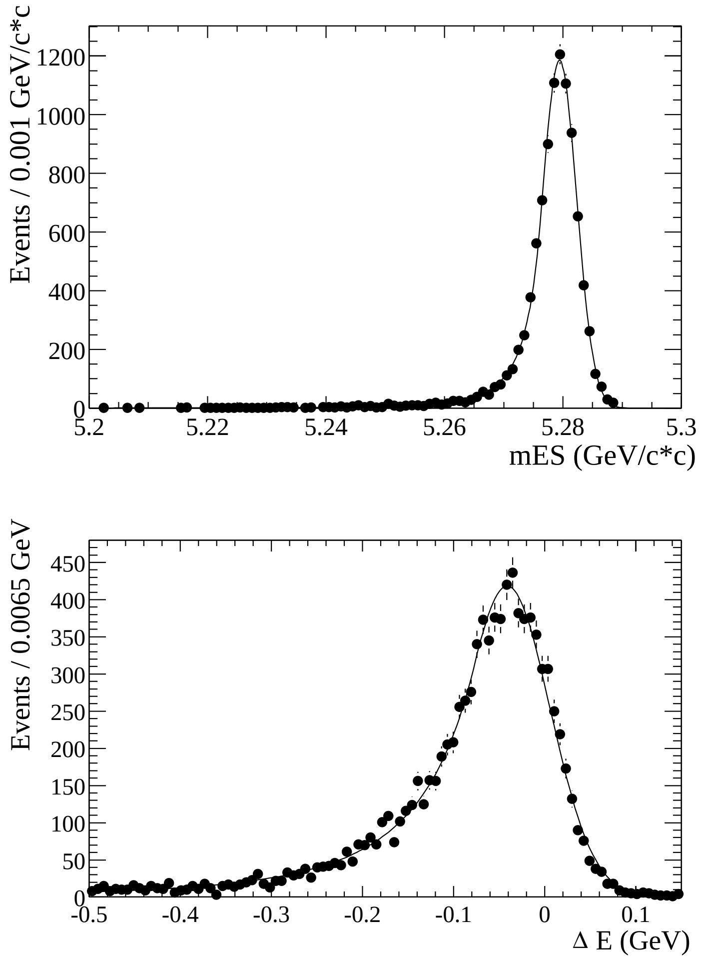

Figure 4.8: *$m_{\rm ES}$ (top) and ΔE (bottom) distributions in the signal $B^{\pm} \to \pi^0 K^{\pm}$ Monte Carlo sample.*

The signal and background event yields obtained from the EML fit are summarised in table 4.10. Figure 4.10 shows the data distributions of $m_{\rm ES}$ and ΔE. A reasonable signal is visible at 5.279 GeV/c^2, with the background fitted with the Argus function. The ΔE distribution does not really have a convincing peak in this projection.

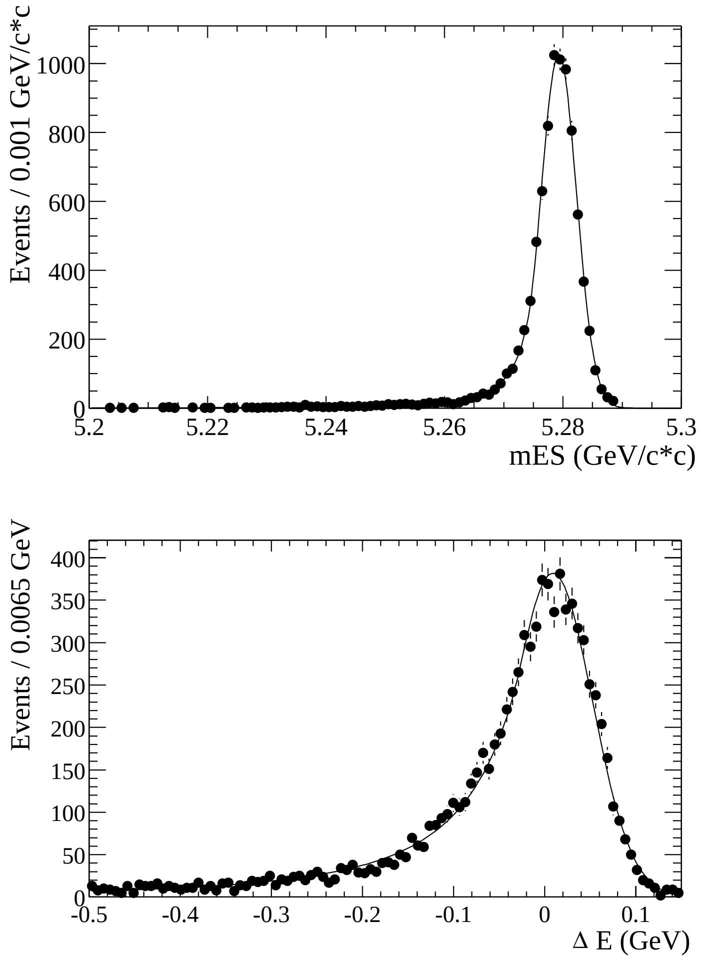

Figure 4.9: *$m_{\rm ES}$ (top) and ΔE (bottom) distributions in the signal $B^{\pm} \to \pi^{\pm}\pi^{0}$ Monte Carlo sample.*

Fit Variable	Fitted Value
$N_{\pi^0 K}$	70.0 ± 15.0
$N_{\pi^0 \pi}$	32.0 ± 15.0
$N_{b\pi^0 K}$	3829.0 ± 65.0
$N_{b\pi^0 \pi}$	9165.0 ± 98.0
ξ	-17.0 ± 1.0
bkg ΔE	-0.94 ± 0.03

Table 4.10: Event yields obtained from the maximum likelihood fit of $B^{\pm} \to \pi^0 K^{\pm}$.

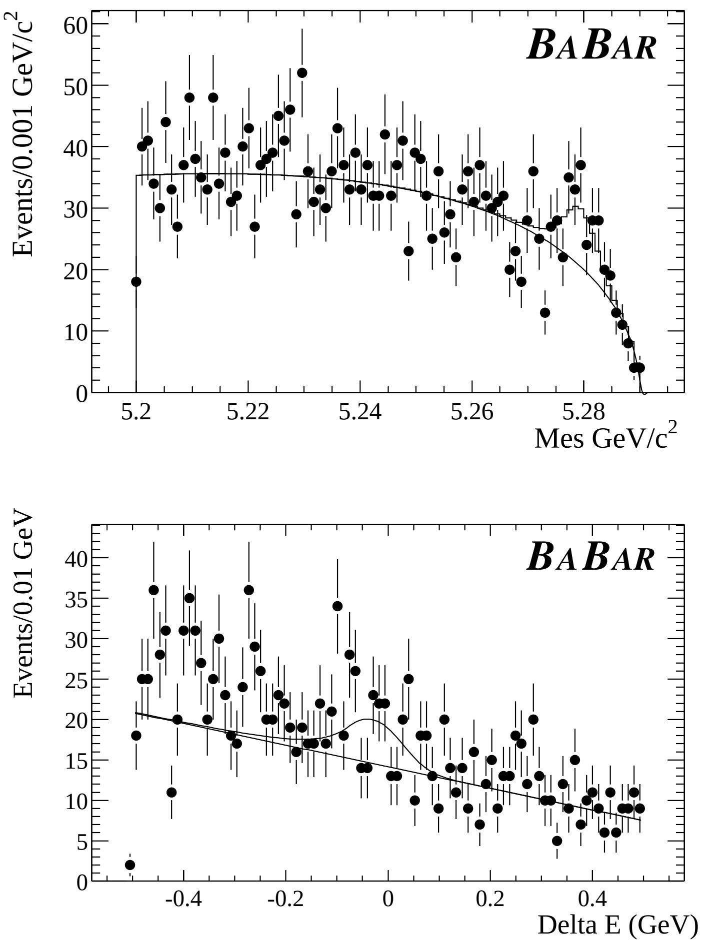

Figure 4.10: *Distributions of $m_{\rm ES}$ (top) and ΔE (bottom) for events enhanced in signal $B^{\pm} \rightarrow \pi^0 K^{\pm}$ decays. The solid curve shows the shape of the background and signal.*

4.3.9 Analysis of $B^0 \to \pi^0 K^0_S$

Again, the Crystal Ball function is used to fit the $m_{\rm ES}$ and ΔE distributions. The parameters obtained are outlined in tables 4.11 and 4.12. The actual distributions and fits for $B^0 \to \pi^0 K^0_S$ are shown in figure 4.11. The unbinned extended maximum

Channel	μ_1 GeV/c^2	$\sigma_1(\times 10^{-3})$ GeV/c^2	α	n
$B^0 \to \pi^0 K^0_S$	5.279	2.961	1.275	3.071

Table 4.11: Crystal Ball fit parameters for $m_{\rm ES}$ distributions of $B^0 \to \pi^0 K^0_S$.

Channel	$\mu_1(\times 10^{-2})$ GeV	$\sigma_1(\times 10^{-2})$ GeV	α	n
$B^0 \to \pi^0 K^0_S$	1.352	4.317	0.627	4.948

Table 4.12: Crystal Ball fit parameters for ΔE distributions of $B^0 \to \pi^0 K^0_S$.

likelihood fit technique developed for the analysis of $B^0 \to \pi^0 K^0_S$ determines four parameters from the data:

- $N_{\pi^0 K^0_S}$, the number of $B^0 \to \pi^0 K^0_S$ decays;
- $N_{b\pi^0 K^0_S}$, the number of background $B^0 \to \pi^0 K^0_S$ decays;
- ξ, Argus background shape parameter;
- the first order polynomial ΔE background shape parameter.

$$\mathcal{P}(m_{\rm ES}, \Delta E, \theta_c) = \frac{N_{\pi^0 K^0_S}}{N}\mathcal{P}_{\pi^0 K^0_S} + \frac{N_{b\pi^0 K^0_S}}{N}\mathcal{P}_{b\pi^0 K^0_S} \tag{4.10}$$

The signal and background event yields obtained from the EML fit are summarised in table 4.13. Figure 4.12 shows the data distributions of $m_{\rm ES}$ and ΔE. The signal peaks for this mode are not at all convincing. The fit has resolved a bump at 5.279 GeV/c^2, along with a zero centered ΔE distribution, but whether this is due to any real signal events is doubtful.

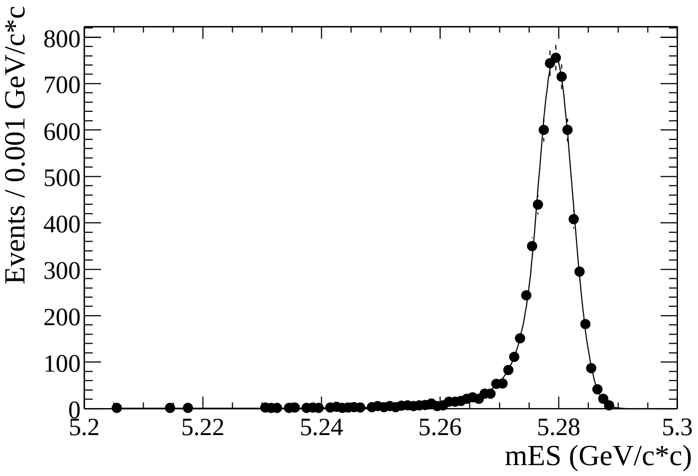

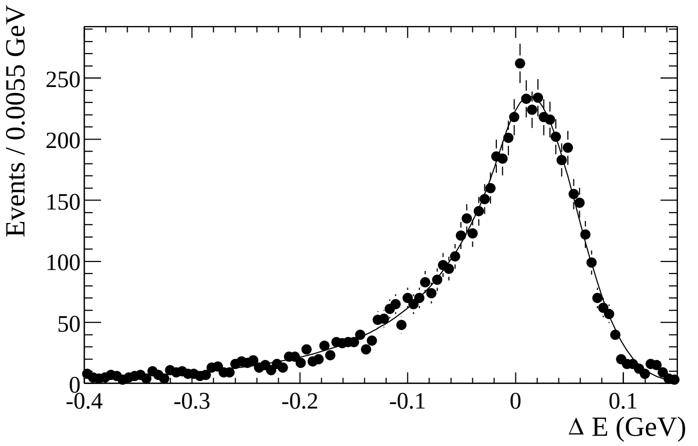

Figure 4.11: *m_{ES} (top) and ΔE (bottom) distributions in the signal $B^0 \to \pi^0 K^0_S$ Monte Carlo sample.*

Fit Variable	Fitted Value
$N_{\pi^0 K^0_S}$	5.0 $\pm$ 6.0
$N_{b\pi^0 K^0_S}$	909.0 $\pm$ 28.0
ξ	-28.0 $\pm$ 4.0
bkg ΔE	-3.0 $\pm$ 0.1

Table 4.13: Event yields obtained from the maximum likelihood fit of $B^0 \to \pi^0 K^0_S$.

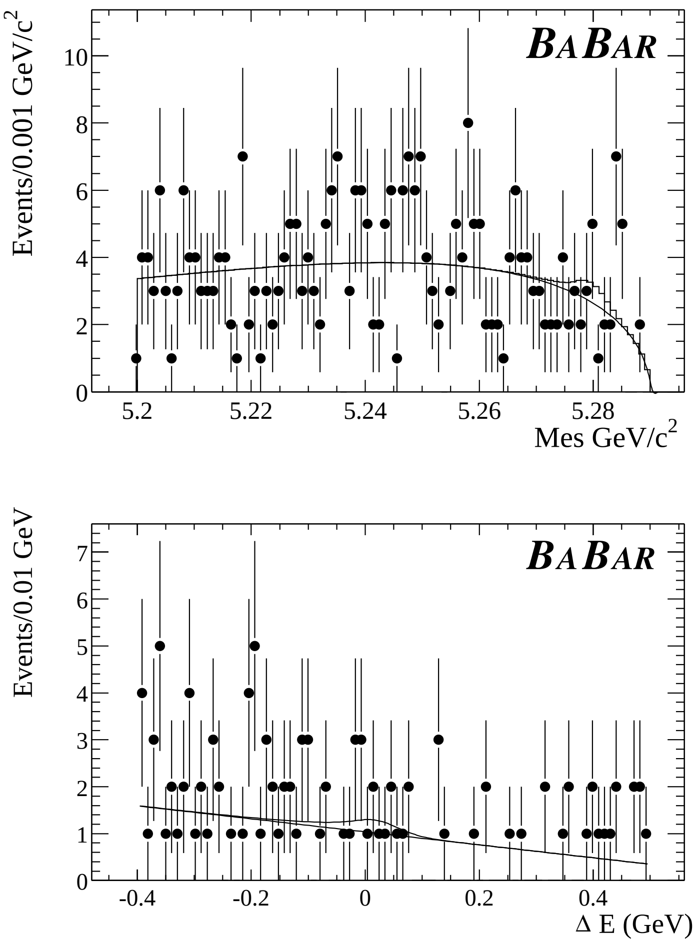

Figure 4.12: *Distributions of $m_{\rm ES}$ (top) and ΔE (bottom) for events enhanced in signal $B^0 \to \pi^0 K_s^0$ decays. The solid curve shows the shape of the background and signal.*

4.4 Determination of Branching Fractions

The branching fractions for $B^0 \to \pi^{\pm}K^{\mp}$, $B^{\pm} \to \pi^{\pm}K^0_S$, $B^{\pm} \to \pi^0 K^{\pm}$ and $B^0 \to \pi^0 K^0_S$ have been calculated. The efficiency of the cuts applied to the on-resonance data sample for each individual channel have been documented in Chapter 3. The branching fractions are calculated as,

$$\mathcal{B} = \frac{N_S}{\epsilon \cdot N_{B\overline{B}}}, \tag{4.11}$$

where N_S is the central value from the fit of the signal yield, ϵ is the total efficiency and $N_{B\overline{B}} = (22.57 \pm 0.36) \times 10^6$, is the total number of $B\overline{B}$ pairs in the Run 1 data set. Equal branching fractions for $\Upsilon(4S) \to B^0\overline{B}^0$ and $\Upsilon(4S) \to B^+B^-$ are assumed in the calculation of $\mathcal{B}$. The branching fractions for each mode, together with statistical errors, are summarised in table 4.14. The branching fractions calculated by the 'cut-and-count' analysis method, using Monte Carlo and off-resonance data) are also included in table 4.14 for ease of comparison. Using off-resonance data to

Channel	$\mathcal{B}(10^{-6})$ (Data)	$\mathcal{B} \times (10^{-6})$ (MC)	$\mathcal{B}_{off} \times (10^{-6})$
$B^0 \to \pi^{\pm}K^{\mp}$	26.6 ± 3.4	8.0 ± 1.9	14.1 ± 1.9
$B^{\pm} \to \pi^{\pm}K^0_S$	17.8 ± 4.0	15.0 ± 4.2	16.6 ± 4.2
$B^{\pm} \to \pi^0 K^{\pm}$	18.9 ± 4.0	1.6 ± 2.4	10.7 ± 2.4
$B^0 \to \pi^0 K^0_S$	4.1 ± 4.2	5.8 ± 4.5	8.5 ± 4.5

Table 4.14: Measured $B \to \pi K$ branching fractions and statistical errors.

estimate the number of background events, N_{off}, in the signal regions to calculate the branching fractions, appears to predict the branching fractions derived from data reasonably accurately in the cases of $B^0 \to \pi^{\pm}K^{\mp}$ and $B^{\pm} \to \pi^{\pm}K^0_S$. The K^0 results are consistent between the methods used. However, the MC background overestimate, noted in Chapter 3, for the results for the charged K channels is confirmed. It should be noted that the maximum likelihood method is intrinsically superior or more likely to give a more accurate result as it is internally consistent, whereas the cut-and-count method is subject to normalisation between the MC and the data.

4.5 Systematic Uncertainties

The systematic uncertainties in the extended maximum likelihood analysis come from an imperfect knowledge of the correct parameterisations of the PDF's and uncertainties in the sample selection cut values.

4.5.1 Variation of PDF's

For each mode, the widths of the PDF's describing m_{ES} were increased and decreased by 8% and the fits repeated. In the case of $B^0 \rightarrow \pi^{\pm}K^{\mp}$, only the widths of the 'main' Gaussian were varied. The widths and the parameter n were increased by 20% and decreased by 10% for ΔE distributions described by the Crystal ball function [58]. The widths of the 'main' Gaussian in the $B^0 \rightarrow \pi^{\pm}K^{\mp}$ ΔE distribution were also increased by 20% and decreased by 10%. The results of the variation of the PDF's study are quoted in terms of number of events in table 4.15. The fourth column contains the average value of the systematics on ΔE for each channel.

4.5.2 Variation of Cuts

The systematic uncertainties due to the values of the cut selection criteria were calculated by first varying the values of the $\cos\theta_K$ for each mode and then varying the value of the K^0_S decay length significance cut, where applicable. Using the plots of Q against $\cos\theta_K$ in figure 3.13, the maximum value of Q was reduced by 20% and the corresponding value of $\cos\theta_K$ was used. The extended maximum likelihood fit was carried out to determine the yield of signal events resulting from the modified cut. The same procedure was carried out with no cut applied to the $\cos\theta_K$ variable and again the signal yield was determined from the fit. For modes containing a K^0_S, cuts on the K^0_S decay length significance of $l_{K^0_S}/\sigma_l > 1.5$ and $l_{K^0_S}/\sigma_l > 30$ were applied.

The optimal cuts were compared with the modified cuts in terms of the branching fractions calculated from the signal yields. The results for the $\cos\theta_K$ are outlined in table 4.16 and for the K^0_S decay length significance cut in table 4.17 .

Channel	Variation	Systematic (# Events)	Ave. ΔE (# Events)
$B^0 \to \pi^\pm K^\mp$	change $m_{\rm ES}$ $\sigma \pm 8\%$	± 3.0	
	increase ΔE σ 20 %	$+12.0$	± 9.5
	decrease ΔE σ 10 %	-7.0	
$B^\pm \to \pi^\pm K^0_S$	change $m_{\rm ES}$ $\sigma \pm 8\%$	± 0.6	
	increase ΔE σ 20 %	$+3.1$	± 2.2
	decrease ΔE σ 10 %	-1.3	
	change $m_{\rm ES}$ $n \pm 8\%$	± 0.3	
	increase ΔE n 20 %	$+0.7$	± 0.5
	decrease ΔE n 10 %	-0.3	
$B^\pm \to \pi^0 K^\pm$	change $m_{\rm ES}$ $\sigma \pm 8\%$	± 2.1	
	increase ΔE σ 20 %	$+7.0$	± 5.5
	decrease ΔE σ 10 %	-4.0	
	change $m_{\rm ES}$ $n \pm 8\%$	± 3.5	
	increase ΔE n 20 %	$+0.8$	± 0.8
	decrease ΔE n 10 %	-0.9	
$B^0 \to \pi^0 K^0_S$	change $m_{\rm ES}$ $\sigma \pm 8\%$	± 0.2	
	increase ΔE σ 20 %	$+0.02$	± 0.03
	decrease ΔE σ 10 %	-0.04	
	change $m_{\rm ES}$ $n \pm 8\%$	± 0.04	
	increase ΔE n 20 %	$+0.1$	± 0.07
	decrease ΔE n 10 %	-0.05	

Table 4.15: Systematic uncertainties in the signal yield due to PDF parameters.

4.5.3 Likelihood Tests with Toy Monte Carlo

The correctness of the fitting procedure and potential correlations between fit components can be examined with "toy" Monte Carlo simulation. A toy Monte Carlo study involves the generation of thousands of toy experiments with statistics similar to those observed in the fit to the Run 1 data. In each toy experiment, the fit variables ($m_{\rm ES}$, ΔE) are generated according to the probability distributions actually used in the maximum likelihood fit. The numbers of signal and background events are given by Poisson distributions with means given by the nominal Run 1 fit results. There is a complication in the channels containing information from the DIRC. The DIRC angle, θ_c, depends on the momentum of the charged track passing through the DIRC. The toy Monte Carlo simulation requires accurate modelling of this momentum spectrum, including the relevant analysis cuts. Therefore, only the

Channel	$\cos\theta_K$	$\mathcal{B}(10^{-6})$	$\cos\theta_K$	$\mathcal{B}(10^{-6})$
$B^0 \to \pi^\pm K^\mp$	0.46	+1.4	1.0	-3.0
$B^\pm \to \pi^\pm K^0_S$	0.28	+0.5	1.0	-2.9
$B^\pm \to \pi^0 K^\pm$	0.32	+1.7	1.0	-3.8
$B^0 \to \pi^0 K^0_S$	0.28	+1.0	1.0	-1.9

Table 4.16: Systematic errors due to variation of $\cos\theta_K$ cut values.

Channel	$l_{K^0_S}/\sigma_l$	$\mathcal{B}(10^{-6})$	$l_{K^0_S}/\sigma_l$	$\mathcal{B}(10^{-6})$
$B^\pm \to \pi^\pm K^0_S$	1.5	+6.2	30	-1.0
$B^0 \to \pi^0 K^0_S$	1.5	+0.9	30	-3.2

Table 4.17: Systematic errors due to variation of $l_{K^0_S}/\sigma_l$ cut values.

neutral channel, $B^0 \to \pi^0 K^0_S$, was checked with the assumption that if this channel was unbiased, then the other channels would also be. A total of 1000 such toy experiments were generated and fitted for the $B^0 \to \pi^0 K^0_S$ channel. The distributions of parameter pulls are defined as,

$$Pull = \frac{N_j^{fit} - N_j^{generated}}{\sigma_j}, \tag{4.12}$$

where, N_j^{fit} and $N_j^{generated}$ are the fitted and generated values for fit parameter, j, and σ_j is the error on N_j returned by the fit. The pull distributions for signal and background $B^0 \to \pi^0 K^0_S$ are shown in figure 4.13. To a good approximation, the signal pull distributions are centered on zero and have unit width.

4.6 Systematics on Conversion to Branching Fractions

There are two main sources of systematic errors on the calculation of the branching fractions. These are an uncertainty in the efficiency (σ_ϵ) and an uncertainty in the total number of $B\overline{B}$ pairs ($\sigma_{N_{B\overline{B}}}$) in the Run 1 data sample. The uncertainty in the efficiency has two components; the uncertainty in the tracking efficiency, which is 2.5% [61] (per track), and the uncertainty in the photon reconstruction efficiency

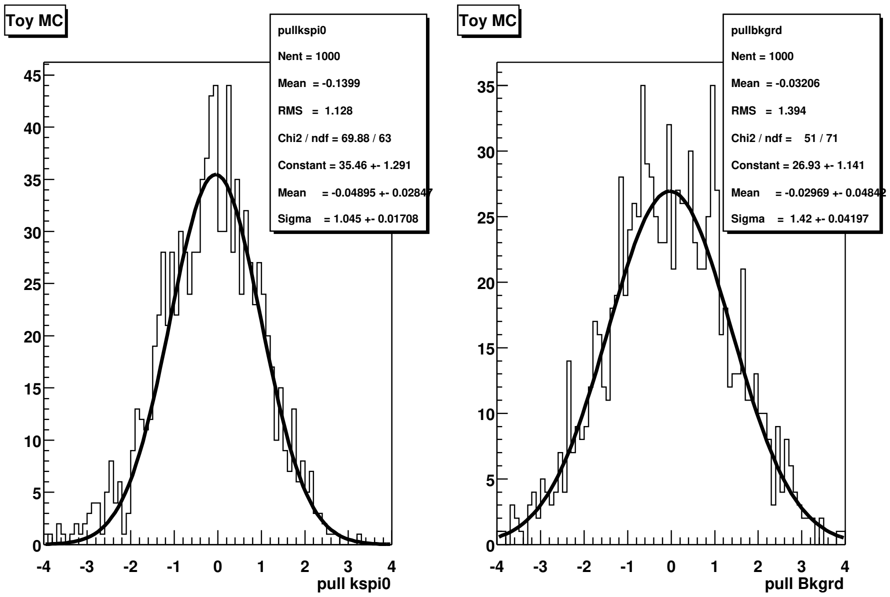

Figure 4.13: *Toy MC study pulls for $K_S^0\ \pi^0$.*

and is also 2.5%. The error on the number of $B\overline{B}$ pairs, which is 1.6%. Table 4.18 summarises the error on the efficiency, (σ_ϵ), the error on the branching fraction due to the efficiency $(\mathcal{B}(\sigma_\epsilon))$ and the error on the branching fraction due to the uncertainty in the number number of $B\overline{B}$ pairs $(\mathcal{B}(\sigma_{N_{B\overline{B}}}))$ for each $B \to \pi K$ channel.

Channel	$\sigma_\epsilon(\%)$	$\mathcal{B}(\sigma_\epsilon)(10^{-6})$	$\mathcal{B}(\sigma_{N_{B\overline{B}}})(10^{-6})$
$B^0 \to \pi^\pm K^\mp$	± 5	± 1.3	± 0.4
$B^\pm \to \pi^\pm K_S^0$	± 7.5	± 1.3	± 0.3
$B^\pm \to \pi^0 K^\pm$	± 7.5	± 1.4	± 0.3
$B^0 \to \pi^0 K_S^0$	± 10	± 0.4	± 0.1

Table 4.18: Systematic errors in the branching fraction calculation due to the uncertainty in efficiency and the number of $B\overline{B}$ pairs.

4.7 Summary of Systematics

The systematic errors in terms of the branching fraction, for each mode, were added in quadrature and the total values of the systematics are summarised in table 4.19

Channel	$\mathcal{B}(10^{-6})$ (syst)
$B^0 \to \pi^\pm K^\mp$	± 3.3
$B^\pm \to \pi^\pm K_S^0$	± 5.3
$B^\pm \to \pi^0 K^\pm$	± 3.6
$B^0 \to \pi^0 K_S^0$	± 2.5

Table 4.19: Total systematic error on measured $B \to \pi K$ branching fractions.

4.8 Charge Asymmetries

The charge asymmetries are calculated for the modes $B^0 \to \pi^\pm K^\mp$, $B^\pm \to \pi^\pm K_S^0$ and $B^\pm \to \pi^0 K^\pm$. The partial rate asymmetry can be written as,

$$\mathcal{A}_{CP} = \frac{N(\overline{B} \to \bar{f}) - N(B \to f)}{N(\overline{B} \to \bar{f}) + N(B \to f)}, \tag{4.13}$$

where B represents either a B^0 or a B^+ meson. In this case, f, represents a self-tagging $B \to \pi K$ mode. $\overline{B}$ and $\bar{f}$ are the conjugate states.

4.8.1 Results

The charge asymmetry, $\mathcal{A}_{CP}$, for $B^0 \to \pi^\pm K^\mp$ was determined from the maximum likelihood fit. It can be shown that $\mathcal{A}_{CP}$ is given by:

$$\mathcal{A}_{CP} = 1 - 2f_{\pi K} \tag{4.14}$$

$f = 0.53 \pm\ 0.06(\mathrm{stat})$, therefore, $\mathcal{A}_{CP} = -0.06 \pm\ 0.12$.

To make a measurement of any charge asymmetry in the $B^\pm \to \pi^\pm K_S^0$ decay channel, a simultaneous maximum likelihood fit of $B^+ \to \pi^+ K_S^0$ and $B^- \to \pi^- K_S^0$ is carried out. The charge of the pion is used to differentiate between the two channels. The fit gives the number of signal and background $B^+ \to \pi^+ K_S^0$ and $B^- \to \pi^- K_S^0$ events. The background shapes are the same for both $B^+ \to \pi^+ K_S^0$ and $B^- \to \pi^- K_S^0$. These numbers are recorded in table 4.20. The errors are statistical. $\mathcal{A}_{\pi^\mp K_S^0}$ is given by,

$$\mathcal{A}_{\pi^\mp K_S^0} = \frac{N(B^- \to \pi^- K_S^0) - N(B^+ \to \pi^+ K_S^0)}{N(B^+ \to \pi^+ K_S^0) + N(B^- \to \pi^- K_S^0)}, \tag{4.15}$$

channel	# Events
$N_{\pi^+ K^0_S}$	21.0 ± 6.0
$N_{\pi^- K^0_S}$	10.0 ± 4.0
$N_{b\pi^+ K^0_S}$	1534.0 ± 43.0
$N_{b\pi^- K^0_S}$	1529.0 ± 44.0

Table 4.20: Signal and background yields of $B^+ \to \pi^+ K^0_S$ and $B^- \to \pi^- K^0_S$. Errors are statistical.

and has a value of $-0.35 \pm 0.23(\text{stat})$. The measurement of any charge asymmetry in $B^\pm \to \pi^0 K^\pm$ was treated in a similar fashion, with a simultaneous maximum likelihood fit being carried out on $B^+ \to \pi^0 K^+$ and $B^- \to \pi^0 K^-$. The results are given in table 4.21.

$\mathcal{A}_{\pi^0 K^\mp}$ is given by,

channel	# Events
$N_{\pi^0 K^+}$	32.0 ± 9.0
$N_{\pi^0 K^-}$	37.0 ± 9.0
$N_{b\pi^0 K^+}$	1893.0 ± 47.0
$N_{b\pi^0 K^-}$	1936.0 ± 46.0

Table 4.21: Signal and background yields of $B^+ \to \pi^0 K^+$ and $B^- \to \pi^0 K^-$. Errors are statistical.

$$\mathcal{A}_{\pi^0 K^\mp} = \frac{N(B^- \to \pi^0 K^-) - N(B^+ \to \pi^0 K^+)}{N(B^- \to \pi^0 K^-) + N(B^+ \to \pi^0 K^+)}, \tag{4.16}$$

and was found to be $+0.07 \pm 0.18(\text{stat})$.

4.8.2 Systematics

To establish the systematic uncertainties present in the evaluation of the asymmetries, the variation of the PDF's and the variation of the selection cuts were again considered.

4.8.3 Systematic Uncertainty in Asymmetry due to the Variation of PDF's

For each mode, the widths of the PDF's describing m_{ES} were increased and decreased as before. The asymmetry value was recorded for each time the fit was varied and the difference between the original asymmetry and the new one was considered to be the systematic error. The results of the variation of the PDF's study are quoted in terms of the difference in the asymmetry value $\mathcal{A}$ for each mode studied, in table 4.22

Channel	Variation	Systematic ($\mathcal{A}$)	Ave. ΔE Systematic ($\mathcal{A}$)
$B^0 \to \pi^\pm K^\mp$	change m_{ES} $\sigma \pm 8\%$	± 0.02	
	increase ΔE σ 20 %	$+0.016$	± 0.014
	decrease ΔE σ 10 %	-0.012	
$B^\pm \to \pi^\pm K^0_S$	change m_{ES} $\sigma \pm 8\%$	± 0.0075	
	increase ΔE σ 20 %	$+0.017$	± 0.002
	decrease ΔE σ 10 %	-0.03	
	change m_{ES} $n \pm 8\%$	± 0.006	
	increase ΔE n 20 %	$+0.008$	± 0.005
	decrease ΔE n 10 %	-0.002	
$B^\pm \to \pi^0 K^\pm$	change m_{ES} $\sigma \pm 8\%$	± 0.02	
	increase ΔE σ 20 %	$+0.01$	± 0.02
	decrease ΔE σ 10 %	-0.02	
	change m_{ES} $n \pm 8\%$	± 0.01	
	increase ΔE n 20 %	$+0.01$	± 0.01
	decrease ΔE n 10 %	-0.01	

Table 4.22: Systematic uncertainties in asymmetry values due to PDF parameters.

4.8.4 Systematic Uncertainty in Asymmetry due to the Variation of the Selection Cuts

The same method as outlined in section 4.6.2 was used to determine the systematic uncertainties in the asymmetries due to the selection criteria. In this case, the asymmetry was calculated and the difference between this and the original value of the asymmetry was recorded. The change in the value of $\mathcal{A}$ due to a change in the value of the $\cos\theta_K$ cut is shown in table 4.23. The change in the value of $\mathcal{A}$ due to

Channel	$\cos\theta_K$	Systematic ($\mathcal{A}$)	$\cos\theta_K$	Systematic ($\mathcal{A}$)
$B^0 \to \pi^\pm K^\mp$	0.46	-0.08	1.0	+0.04
$B^\pm \to \pi^\pm K^0_S$	0.28	-0.03	1.0	+0.06
$B^\pm \to \pi^0 K^\pm$	0.32	-0.07	1.0	+0.05

Table 4.23: Systematic errors due to variation of $\cos\theta_K$ cut values.

a change in the value of the $l_{K^0_S}/\sigma_l$ cut is shown in table 4.24 for the $B^\pm \to \pi^\pm K^0_S$ mode.

Channel	$l_{K^0_S}/\sigma_l$	Systematic ($\mathcal{A}$)	$l_{K^0_S}/\sigma_l$	Systematic ($\mathcal{A}$)
$B^\pm \to \pi^\pm K^0_S$	1.5	-0.02	30	+0.03

Table 4.24: Systematic errors due to variation of $l_{K^0_S}/\sigma_l$ cut values.

4.9 Summary of Systematics on Charge Asymmetries

The systematic errors on the charge asymmetries, for each mode, were added in quadrature and the total values of the systematics are summarised in table 4.25.

Channel	$\mathcal{A}$ (syst)
$B^0 \to \pi^\pm K^\mp$	± 0.07
$B^\pm \to \pi^\pm K^0_S$	± 0.08
$B^\pm \to \pi^0 K^\pm$	± 0.06

Table 4.25: Total systematic error on $B \to \pi K$ asymmetries.

4.10 Summary of Results

A summary of the results of the $B \to \pi K$ branching fraction measurements and charge asymmetries are tabulated below:

Channel	$\mathcal{B}(10^{-6})$
$B^0 \to \pi^\pm K^\mp$	$26.6 \pm 3.4(\text{stat}) \pm 3.3(\text{syst})$
$B^\pm \to \pi^\pm K_S^0$	$17.8 \pm 4.0(\text{stat}) \pm 5.3(\text{syst})$
$B^\pm \to \pi^0 K^\pm$	$18.9 \pm 4.0(\text{stat}) \pm 3.6(\text{syst})$
$B^0 \to \pi^0 K_S^0$	$4.1 \pm 4.2(\text{stat}) \pm 2.5(\text{syst})$

Table 4.26: Measured $B \to \pi K$ branching fractions with statistical and systematic errors.

Channel	$\mathcal{A}$
$B^0 \to \pi^\pm K^\mp$	$-0.06 \pm 0.12(\text{stat}) \pm 0.07(\text{syst})$
$B^\pm \to \pi^\pm K_S^0$	$-0.35 \pm 0.23(\text{stat}) \pm 0.08(\text{syst})$
$B^\pm \to \pi^0 K^\pm$	$+0.07 \pm 0.18(\text{stat}) \pm 0.06(\text{syst})$

Table 4.27: $B \to \pi K$ asymmetries with statistical and systematic errors.

Chapter 5

Conclusions

5.1 The Branching Fractions

The branching fractions for all charged and neutral $B \to \pi K$ modes have been measured using the BaBar Run 1 data set. Table 5.1 summarises these results and compares them with $B \to \pi K$ branching fractions measured by the Belle experiment [26] in Japan. The Belle results are based on 10.4 fb^{-1} of data collected at the KEKB e^+e^- storage ring. The values measured are consistent with those obtained

Channel	$\mathcal{B}(10^{-6})$	$\mathcal{B}(10^{-6})$ Belle
$B^0 \to \pi^\pm K^\mp$	$26.6 \pm 3.4(\text{stat}) \pm 3.3(\text{syst})$	$19.3^{+3.4+1.5}_{-3.2-0.6}$
$B^\pm \to \pi^\pm K^0_S$	$17.8 \pm 4.0(\text{stat}) \pm 5.3(\text{syst})$	$13.7^{+5.7+1.9}_{-4.8-1.8}$
$B^\pm \to \pi^0 K^\pm$	$18.9 \pm 4.0(\text{stat}) \pm 3.6(\text{syst})$	$16.3^{+3.5+1.6}_{-3.3-1.8}$
$B^0 \to \pi^0 K^0_S$	$4.1 \pm 4.2(\text{stat}) \pm 2.5(\text{syst})$	$16.0^{+7.2+2.5}_{-5.9-2.7}$

Table 5.1: $B \to \pi K$ branching fractions measured for this dissertation and the $B \to \pi K$ branching fractions measured by Belle (with statistical and systematic errors).

by the Belle experiment. The statistical errors in each mode are similar to those of Belle. Significant signals have been measured for $B^0 \to \pi^\pm K^\mp$, $B^\pm \to \pi^\pm K^0_S$ and $B^\pm \to \pi^0 K^\pm$.

The systematic errors quoted are of the same order as the statistical errors, this implies that further statistics would not improve the total errors. However, this is unlikely to be the case. The systematic errors are based on fits to the same data

sample as the signal yield results, they are therefore prone to the same statistical errors as the data sample. The systematic errors had to be calculated using the main data sample because the Monte Carlo sample was only half the size of the data sample. The above systematic errors could be dominated by purely statistical effects and would then effectively represent upper limits.
$B^0 \rightarrow \pi^{\pm}K^{\mp}$ yielded the greatest number of events (126.0 ± 16.0, see section 4.3.6). The maximum likelihood fit of this channel also revealed the presence of approximately 23.0 ± 11.0 $B^0 \rightarrow \pi^{\mp}\pi^{\pm}$ events in the sample. A very speculative conclusion could be drawn from the large difference in the numbers of $B^0 \rightarrow \pi^{\pm}K^{\mp}$ and $B^0 \rightarrow \pi^{\mp}\pi^{\pm}$ events observed; the Penguin diagram would dominate the rare charmless two-body Feynmann diagrams. This domination of the Penguin over the Tree diagram would lead to significant difficulties in extracting the value of sin2α.

5.2 The Asymmetries

Channel	$\mathcal{A}$
$B^0 \rightarrow \pi^{\pm}K^{\mp}$	$-0.06 \pm 0.12(\text{stat}) \pm 0.07(\text{syst})$
$B^{\pm} \rightarrow \pi^{\pm}K^0_S$	$-0.35 \pm 0.23(\text{stat}) \pm 0.08(\text{syst})$
$B^{\pm} \rightarrow \pi^0K^{\pm}$	$+0.07 \pm 0.18(\text{stat}) \pm 0.06(\text{syst})$

Table 5.2: $B \rightarrow \pi K$ asymmetries with statistical and systematic errors.

All the asymmetry measurements are consistent with zero. No observation of Direct CP Violation can be claimed. The asymmetry measurements are dominated by statistical errors, which have a long way to go before they reach the level of the systematic errors. A considerably larger data set must be accumulated before a meaningful measurement of the expected charge asymmetries can be made. BaBar is well on the way to achieving unprecedented amounts of data, and I look forward to reading about their results in the future.

References

[1] E. Noether, Nachr. Ges. Wiss. Göttingen (1918), 171.

[2] G.D. Rochester and C.C. Butler *Nature* **160** (1947) 855.

[3] T.D. Lee and C.N. Yang, Phys. Rev. **104** (1956) 251.

[4] M. Gell-Mann and A. Pais, Phys. Rev. **97** (1955) 1387.

[5] K. Lande *et al.*, Phys. Rev. **103** (1956) 1901.

[6] J.H. Christenson, J.W. Cronin, V.L. Fitch and R. Turlay, Phys. Rev. Lett. **13** (1964) 138.

[7] A.D. Sakharov, 5 (1967) 32; JETP Lett. **5** (1967) 24.

[8] S.W. Herb *et al.*, Phys. Rev. Lett. **59** (1977) 252.

[9] BaBar Collaboration, B. Aubert *et al.*, Phys. Rev. Lett. **87** (2001) 091801.

[10] Belle Collaboration, K. Abe *et al.*, Phys. Rev. Lett. **87** (2001) 091802.

[11] E. Leader and E. Predazzi, *"An Introduction to Gauge Theories and Modern Particle Physics"*, Vol 2 (Cambridge University Press) (1996) p.12.

[12] R. E. Marshak and C.P. Ryan, *"The Theory of Weak Interactions in Particle Physics"*, (Wiley, New York) (1969).

[13] BaBar Collaboration, B. Aubert *et al.*, *"Measurement of the time dependence of $B^0\overline{B}^0$ oscillations using inclusive dilepton events"*, paper submitted to the 30^{th} International Conference on High Energy Physics, Osaka Japan (2000).

[14] M. Gronau, J.L. Rosner and D. London, Phys. Rev. Lett. **73** (1994) 21.

[15] O.F. Hernández, D. London, M. Gronau and J.L. Rosner, Phys. Lett. **B333** (1994) 500; M. Gronau, O. F. Hernández, D. London and J.L. Rosner, Phys. Rev. **D50** (1994) 4529.

[16] N. Cabibbo, Phys. Rev. Lett. **10**, (1963) 531.

[17] M. Kobayashi and T. Maskawa, Prog. Th. Phys. **49** (1973) 652.

[18] Particle Data Group, D.E. Groom *et al.*, Eur. Phys. Jour. C **15** (2000) 1.

[19] L.L. Chau and W.Y. Keung, Phys. Rev. Lett. **53** (1984) 1802.

[20] L. Wolfenstein, Phys. Rev. Lett. **51** (1983) 1945.

[21] A.J. Buras and R. Fleischer, hep-ph9704376, in *"Heavy Flavours II"*, World Scientific (1998), eds. A.J. Buras and M. Linder, p. 65-238.

[22] Y. Nir, *"CP Violation in and Beyond the Standard Model"*, SLAC Summer Institute (1999).

[23] R. Fleischer and T. Mannel, Phys. Rev. D **57** (1998) 2752.

[24] CLEO Collaboration, R. Godang *et al.*, Phys. Rev. Lett. **80** (1998) 3456.

[25] M. Gronau and J.L. Rosner, Phys. Rev. **D57** (1998) 6843.

[26] Belle Collaboration, K. Abe *et al.*, Phys. Rev. Lett. **87** (2001) 101801.

[27] CLEO Collaboration, D. Cronin-Hennessy *et al.*, Phys. Rev. Lett. **85** (2000) 525.

[28] M. Neubert and J.L. Rosner, Phys. Rev. Lett. **81** (1998) 23.

[29] M. Neubert and J.L. Rosner, Phys. Lett. B **441** (1998) 403.

[30] A.J. Buras and R. Fleischer, Eur. Phys. Jour. C **11** (1999) 93.

[31] R. Fleischer, Int. Jour. Mod. Phys. **A12** (1997) 2459.

[32] L. Wolfenstein, Phys. Rev. **D52** (1995) 537; J.F. Donoghue, E. Golowich, A.A. Petrov and J.M. Soares, Phys. Rev. Lett. **77** (1996) 2178; B. Blok and I. Halperin, Phys. Lett. **B385** (1996) 324; B. Blok, M. Gronau and J.L. Rosner, Phys. Rev. Lett. **78** (1997) 3999.

[33] R. Fleischer, Eur. Phys. Jour. C **6** (1998) 451.

[34] M. Gronau and J.L. Rosner, Phys. Rev. D **57** (1998) 6843.

[35] A.J. Buras, R. Fleischer and T. Mannel, Nucl. Phys. B **533** (1998) 3.

[36] M. Gronau, O.F. Hernández, D. London and J. L. Rosner, Phys. Rev. **D52** (1995) 6356.

[37] A.J. Buras and R. Fleischer, Phys. Lett. **B341** (1995) 379; R. Fleischer, Phys. Lett. **B341** (1994) 205.

[38] N.G. Deshpande and X.-G. He, Phys. Rev. Lett. **74** (1995) 26 [E: *ibid.,* p. 4099].

[39] M. Gronau, O.F. Hernández, D. London and J.L. Rosner, Phys. Rev. **D52** (1995) 6374.

[40] M. Gronau and J.L. Rosner, Phys. Rev. Lett. **76** (1996) 1200; A.S. Dighe, M. Gronau and J.L. Rosner, Phys. Rev. **D54** (1996) 3309; A.S. Dighe and J.L. Rosner, Phys. Rev. **D54** (1996) 4677.

[41] The PEP-II Conceptual Design Report, SLAC-PUB-418 (1993).

[42] The BaBar Technical Design Report, SLAC-R-95-457 (1995).

[43] The BaBar Collaboration, B. Aubert *et al.*, *"The BaBar Detector"* hep-ex/105044, to appear in Nucl. Instr. and Methods **.**

[44] P.F. Harrison and H.R. Quinn (eds.) *The BaBar Physics Book: Physics at an Asymmetric B Factory"*, SLAC-R-0504 (1998).

[45] P. Billoir, Nucl. Instr. and Methods A **225** (1984) 225.

[46] C. Touramanis *et al.*, *"Reconstruction of π^0 in BaBar"*, BaBar Analysis Document # 20 (2000).

[47] U. Berzano *et al.*, *"Measurement of Branching Fractions for Charmless Two-Body B Decays"*, BaBar Analysis Document # 38 (2000).

[48] A. Drescher *et al.*, Nucl. Instr. and Methods A **237** (1985) 464.

[49] C. Hearty *et al.*, *"Measurement of the Number of $\Upsilon(4S)$ Mesons Produced in Run 1 (B Counting)"*, BaBar Analysis Document # 134 (2001).

[50] C. Hearty *et al.*, *"Hadronic Event Selection and B Counting For Inclusive Charmonium Measurements"*, BaBar Analysis Document # 30 (2000).

[51] Belle Collaboration, K. Abe *et al.*, Phys. Rev. Lett. **87** (2001) 101801.

[52] G.C. Fox and S. Wolfram, Phys. Rev. Lett. **41** (1978) 1581.

[53] J.D. Bjorken and S.D. Brodsky, Phys. Rev. D **1** (1970) 1416.

[54] K. Flood *et al.*, *"Thrust Calculation at BaBar"*, BaBar Analysis Document # 305 (2001).

[55] U. Egede *et al.*, *"A User's Guide to the RooFitTools Package for Unbinned Maximum Likelihood Fitting"*, BaBar Analysis Document # 18 (2001).

[56] D. Antreasyan, Crystal Ball Note 321 (1983).

[57] H. Albrecht *et al.*, ARGUS Collaboration, Phys. Lett. **B185** (1987) 218.

[58] U. Berzano *et al.*, *"Analysis of Neutral B Decays to $\pi^+\pi^-$, $K^+\pi^-$ and K^+K^-"*, BaBar Analysis Document # 160 (2001).

[59] U. Berzano *et al.*, *"Measurement of Branching Fractions for Charmless $B \rightarrow h'h^0$"*, BaBar Analysis Document # 98 (2001).

[60] A. Bevan *et al.*, *"Measurement of Branching Fractions for Charmless $B \rightarrow h^0h^0$"*, BaBar Analysis Document # 148 (2001).

[61] BaBar Collaboration, B. Aubert *et al.*, "The first year of the BaBar experiment at PEP-II", paper submitted to the 30^{th} International Conference on High Energy Physics, Osaka, Japan (2000).

[62] Belle Collaboration, K. Abe *et al.*, Phys. Rev. D **64** (2001) 071101.